

NASA TECHNICAL NOTE



NASA TN D-2854

NASA TN D-2854

**A PARAMETRIC STUDY OF THE
AERODYNAMIC CHARACTERISTICS
OF NOSE-CYLINDER-FLARE BODIES
AT A MACH NUMBER OF 6.0**

by George C. Ashby, Jr., and Aubrey M. Cary, Jr.

Langley Research Center

Langley Station, Hampton, Va.

A PARAMETRIC STUDY OF THE AERODYNAMIC CHARACTERISTICS OF
NOSE-CYLINDER-FLARE BODIES AT A MACH NUMBER OF 6.0

By George C. Ashby, Jr., and Aubrey M. Cary, Jr.

Langley Research Center
Langley Station, Hampton, Va.

NATIONAL AERONAUTICS AND SPACE ADMINISTRATION

For sale by the Clearinghouse for Federal Scientific and Technical Information
Springfield, Virginia 22151 - Price \$3.00

A PARAMETRIC STUDY OF THE AERODYNAMIC CHARACTERISTICS OF
NOSE-CYLINDER-FLARE BODIES AT A MACH NUMBER OF 6.0

By George C. Ashby, Jr., and Aubrey M. Cary, Jr.
Langley Research Center

SUMMARY

Force tests were conducted at a Mach number of 6.0 on nose-cylinder-flare bodies to determine the effect of nose shape, cylinder length, flare angle, and flare length on the longitudinal aerodynamic characteristics. A particular investigation was conducted to determine the effect of flare angle for constant flare length, surface area, and diameter. Results indicated that at a Reynolds number of approximately 0.92×10^6 (based on body diameter), the boundary-layer separation effects were significant only with respect to the slope of the normal-force and pitching-moment curve at low angles of attack. The variations of the aerodynamic characteristics with the various parameters were, in general, similar to those predicted by Newtonian theory below a flare angle of 30° and a ratio of flare base diameter to cylinder diameter of less than approximately 2.2. The limiting diameter ratio is consistent with the extent of the low-constant dynamic-pressure region near the body caused by the bow-shock influences as predicted by axisymmetric characteristic theory.

The effects of the various parameters for the flares that exceeded the limiting diameter ratio follow the trends predicted by the computed flow-field properties. The axial force for these flare configurations at zero angle of attack was, in general, computed within 10 percent by using these properties. For a constant flare length and surface area the flare effectiveness increased with increasing flare angle; however, for constant flare diameter only the axial-force coefficient was affected by flare angle.

INTRODUCTION

The cone-cylinder-flare configuration has many advantages as a reentry body: The nose shape can be adjusted to facilitate present ablative techniques and to produce required drag for a given trajectory; the centerbody length can be adjusted for payload size; and the flare angle and length can be varied to produce a stable configuration.

Numerous investigations for the subsonic, transonic, and supersonic speed range have determined the aerodynamic characteristics of cone-cylinder-flare bodies of various geometrical ratios. (For example, see refs. 1 to 6.) In addition, the aerodynamic characteristics of cone-cylinder-flare configurations

have been investigated at hypersonic speeds (for example, refs. 7 to 10); however, most of the investigations were generally unsystematic and somewhat limited in scope.

The purpose of the present program is to provide a systematic study to aid in the aerodynamic design of cone-cylinder-flare reentry bodies at hypersonic speeds. The overall objective of this study was to show the effect of nose bluntness, midbody length, flare angle, and flare length on the longitudinal aerodynamic characteristics of the cone-cylinder-flare type bodies, while an attempt was made to provide a theoretical basis for prediction of the experimental data. Because this type of body may be mated to another vehicle at its flare end, a particular objective was to show the effect of flare angle on the aerodynamic characteristics when flare length, flare diameter, and flare surface area were fixed.

SYMBOLS

A	cross-sectional area of the cylinder midbody section
C_A	axial-force coefficient, $\frac{\text{Axial force}}{q_\infty A}$
$C_{A,b}$	base axial-force coefficient, $\frac{\text{Base axial force}}{q_\infty A}$
C_m	pitching-moment coefficient, $\frac{\text{Pitching moment}}{q_\infty A D_c}$
C_{m_α}	slope of pitching-moment curve, $\frac{\partial C_m}{\partial \alpha}$ per degree
C_N	normal-force coefficient, $\frac{\text{Normal force}}{q_\infty A}$
C_{N_α}	slope of normal-force curve, $\frac{\partial C_N}{\partial \alpha}$ per degree
C_p	pressure coefficient
D_c	diameter of the cylinder midbody section
D_f	diameter of the flare base
K	proportionality constant for Newtonian theory
l	distance downstream from nose-cylinder junction

l_c	length of cylinder midbody section
l_f	length of flare section
M	Mach number
q	dynamic pressure
q_∞	free-stream dynamic pressure
r	radial distance measured perpendicular to the body center line
S_f	surface area
$x_{c.p.}$	center of pressure referenced to cylinder-flare junction; positive when toward rear
α	angle of attack
δ	flow deflection angle
θ_c	nose-cone half-angle
θ_f	angle of the flare with respect to the body center line

APPARATUS AND METHODS

Models

The dimensions of the models and the location of the moment reference center are shown in figure 1. The models consisted of three basic sections: nose section, cylinder midbody section, and cone frustum flare section. The two nose sections used were conical and hemispherical; the two cylinders used measured 4 diameters and 1 diameter in length; and the flares utilized varied in angle from 0° to 30° and in length from 0.61 to 3 cylinder diameters long, the length depending on the flare angle. Figure 1 shows the lengths for each flare selected to show the effect of flare angle when flare length, flare surface area, and flare diameter were held constant. The moment reference center was located at the cylinder-flare junction for all configurations tested.

Wind Tunnel

The tests were conducted in the Langley 20-inch Mach 6 tunnel. The tunnel is of the intermittent type exhausting to the atmosphere and is operated from a stored air supply at stagnation pressures from approximately 7 to 38 atmospheres and a maximum stagnation temperature of 600° F. A fixed two-dimensional nozzle block is employed; the test section is rectangular, 20 by 20.5 inches. A more

detailed description of the tunnel is given in reference 11. The tests were run at a stagnation temperature of approximately 450° F for all cases; the corresponding Reynolds number per foot was 0.554×10^6 .

Methods

The aerodynamic forces were measured by use of a six-component electrical strain-gage balance housed inside the model; the balance was rigidly connected to a sting support system. A motor rotated the support system to change the angle of attack in the vertical plane. An optical system described in reference 12 was used to set the angle of attack. For the majority of the tests two base pressure tubes were located behind the model in the plane of the model base; however, because many of the measured base pressures were not valid, no base pressure corrections were made on the axial-force coefficient. The correction to the axial-force coefficient for the base pressure is presented in figure 2 for the configurations for which there are valid data. Sufficient data are shown to be representative of all the models; in most instances, the effect of base pressure on the data is relatively small and invariant with angle of attack. Because the Mach number of the test section can vary as much as 0.1, the variation depending on the operating schedule explained in reference 13, the Mach number was measured for each test point with a total-head probe. The probe was located off the center line of the tunnel to avoid interference from the model bow shock.

Accuracy

On the basis of the balance calibration readout accuracy, and dynamic-pressure accuracy, it is estimated by the method of least squares, that the measured quantities are accurate within the following maximum average limits:

	$\theta_f < 30^{\circ}$	$\theta_f = 30^{\circ}$
C_N	± 0.125	± 0.145
C_A	± 0.030	± 0.155
C_m	± 0.120	± 0.200

The angle of attack is believed to be correct within $\pm 1/2^{\circ}$. It is noted that the combination of measuring errors of the coefficients and of the angles of attack caused the curves to pass through 0 at angles of attack up to 4° in some cases; however, the values of the coefficients near zero angle of attack are, in general, consistent with the estimated errors.

RESULTS AND DISCUSSION

Analysis of Flow About Bodies

In general, the forces and moments of flare stabilized bodies are affected by boundary-layer separation (see, for example, refs. 14 and 15), bow-shock influence on the dynamic pressures near the flares (ref. 16), and bow-shock--flare-shock intersection effects (ref. 17). The occurrence and effect of these phenomena on the aerodynamic characteristics of the configurations of the present investigation are discussed in the following sections.

Boundary-layer separation.-- References 14 and 15 show that boundary-layer separation effects on flare stabilized bodies are usually manifested by a reduction in axial force at $\alpha = 0^\circ$ and by an increase in the slopes of the normal-force and negative pitching-moment curves near zero angle of attack. An explanation of these results is contained in reference 15. The effect of boundary-layer separation on the windward meridian usually disappears as angle of attack increases, and the coefficient curves become coincident or at least parallel with those curves occurring for configurations free of separation over the whole angle-of-attack range.

A feel for the magnitude of the effect of separation on the longitudinal aerodynamic data (at least for the long-cylinder configuration, $l_c/D_c = 4.0$) can be obtained from references 18, 19, and 20. References 18 and 19 present the pressure distribution on ogive cylinders with a 30° flare and reference 20, the pressure distribution on a flat plate with a 30° wedge. The local Reynolds number at the flare or wedge is approximately the same in these references as that of the present tests. These references indicate that boundary-layer separation would not strongly affect the pressure distribution, and, therefore, the flare forces are not strongly affected when the Reynolds number is large enough for a turbulent or near turbulent boundary layer. However, reference 21, which presents pressure data for a cone-cylinder-flare body with laminar flow, indicates that the pressure distribution can be strongly affected when the flow separates. A comparison of the transitional Reynolds numbers in references 18, 22, and 23 with those of the present investigation indicates that, at zero angle of attack, the boundary layer at the cylinder-flare junction for the conical-nose long-cylinder body ($l_c/D_c = 4.0$) would be transitional or turbulent whereas the blunt nose configurations would tend towards laminar conditions at the flare. For the short-cylinder configurations ($l_c/D_c = 1.0$) for both noses, the boundary layer at the flare location would probably be laminar at zero angle of attack. It should be remembered that the different shape of the nose-cylinder junction also has some effect on boundary-layer conditions downstream.

The schlieren photographs, figures 3 and 4, show typical examples of the variation of flow separation as flare angle, nose shape, cylinder length, and angle of attack are varied. Probably the most important observation to be made from figure 3 is that the extent of the separation on the flare is not large on any of these models except for the hemispherical-nose $l_c/D_c = 4.0$ 20° and 30° flare models.

Figure 4 shows that flow separation on the flare along the windward meridian has been greatly reduced at $\alpha = 6^\circ$ compared with that at $\alpha = 0^\circ$ for all configurations. There are several additional observations that can be made from figures 3 and 4 with respect to boundary-layer separation: First, the conical-nose long-cylinder configuration has a smaller extent of separation on the flare than the conical-nose short-cylinder configuration; second, blunting the configurations has opposite effects, flow separation is increased on the flare for the long-cylinder configurations and decreased for the short-cylinder configurations. Reference 21 shows a similar effect of cylinder length for a conical-nose body. From this discussion, flow-separation effects are not expected to be significant on any configurations except possibly the hemispherical-nose $l_c/D_c = 4.0$ 20° and 30° flare models.

Flow field.- To aid in the evaluation of the effect of the body geometry on the aerodynamic characteristics, the properties of the flow field between the body and bow shock were computed for both the cone-cylinder and hemisphere-cylinder bodies without flares by an automatic computer program utilizing the method of characteristics. The normalized dynamic-pressure distributions at four cylindrical stations are presented in figure 5. For both noses a region of low and nearly constant dynamic pressure exists near the surface of the cylinder along the whole cylinder length. As cylinder length increases the radial extent of this low-dynamic-pressure region increases until the length exceeds $l_c/D_c = 3$; beyond this point the region remains nearly constant. Between the region of nearly constant dynamic pressure and the bow shock, the dynamic pressure increases at a rapid rate. Blunting the nose lowers the dynamic-pressure level and increases the radial extent of the low-constant dynamic-pressure region but does not alter the level or gradient very much between this region and the bow shock. The effect of blunting is more easily seen in figure 5(c) where the two fields were superimposed with the bow shocks coincident. The two flow-field plots show that a conical flare which extends beyond the low-constant energy region near the body would be markedly more effective because the energy level of the flow increases very rapidly and the flare area upon which the flow acts increases. For body stations of 1 diameter or more, conical flares must have angles greater than about 20° and base diameters larger than approximately 2.2 cylinder diameters to extend into the high energy portion of the flow field. These limits apply approximately for both noses and indicate that the nose cone angle selected for the present investigation was too large to show fully the effect of nose blunting.

This observation indicates that at zero angle of attack all the flares of the present investigation, except for the longest 30° flare, are embedded in the low energy region near the cylindrical body even for the conical-nose configurations. An increase in flare size beyond the limit stated would be required to reap any benefit of the large energy gradient outside the low energy region for both nose configurations.

Bow-shock—flare-shock intersection effects.- As shown in figure 4, the intersection of the bow shock and flare shock moves closer to the flare as angle of attack increases, and at some angle of attack the point of intersection moves into the flow region immediately ahead of the flare. For a given Mach number the angle of attack at which this happens is dependent upon nose

bluntness, cylinder length, flare angle, and flare length. The effect of the proximity of the shock intersection to the flare is shown in reference 17 to be a reduction in the surface pressures on the outboard portion of the flare and to be due to expansion waves emanating from the shock intersection. The pressure reduction on the rearward portion of the flare surface reduced the normal and axial forces and the negative pitching moment. An indication of the magnitude of the effect can be gaged from the results of reference 17 for a 10° flare which show that the pressure on the affected portion of the flare surface is reduced by approximately one-third. For the present investigation the schlieren photographs of figure 4 for the body at angle of attack indicate that the shock intersection is in the proximity of the higher angle flares at low angles of attack when the cylinder length is 1 diameter.

Experimental Results and General Comments

The measured longitudinal aerodynamic data along with Newtonian estimates for each flare angle and $x_{c.p.}$ are presented in figures 6 to 9. At all angles of attack except zero, $x_{c.p.}$ was determined by dividing C_m by C_N . Because both C_m and C_N approach zero as angle of attack does, the value of C_m/C_N becomes indeterminate. To avoid this result, the slope (dC_m/dC_N) at zero angle of attack was found by taking the values over the angle-of-attack range from -2° to 2° . The angle of attack at which the bow-shock-flare-shock intersection is in proximity to the flare (obtained from schlieren photographs) is shown on the figures by a vertical line at the appropriate angle of attack. Figure 10 presents the variation of the slopes of the normal-force and pitching-moment coefficients with flare length at zero angle of attack. In addition, a plot of the typical variation of C_N and C_m with flare angle and flare length at a constant α are shown in figure 11.

It is widely known that Newtonian theory ($C_p = K \sin^2\delta$) is not accurate when the body shock does not closely envelop the body as would be the case for the flares. However, because the concept of the theory is free of the effects of the boundary-layer separation, of flow-field variations, and of bow-shock-flare-shock interaction, the theory was used to provide a basis for the trends of the aerodynamic characteristics in relation to various parametric changes. For the present calculations the conventional proportionality constant of 2.0 was used for the conical-nose configurations. Allowance for the effect of the nose bluntness was made by using the modified value of K (1.818) for the hemispherical-nose configurations. The predicted values for each nose-cylinder-flare configuration are the sum of the values attributed to the lateral surface of each individual component, no allowance being made for the shielding of the flare surface by the forebody as angle of attack is increased.

By using the schlieren photographs and the Newtonian estimates as a guide, a general analysis of the results in figures 6 to 10 indicates that boundary-layer separation effects are small for all flares less than 30° . The slopes of the C_N and C_m curves near zero angle of attack for this group are only slightly affected, whereas for the 30° flares, the slopes are affected considerably. The effects of separation on the slopes disappear, however, beyond an

angle of attack of about 5° . For the 30° flares at zero angle of attack the decrease of C_A below the Newtonian value when the nose is blunted is attributed primarily to flow-field effects (rather than to increased separation) because of the size of the decrease of C_A relative to the increase of flow separation and because of the increasing difference between the measured and Newtonian values with increasing flare length. The differences in $x_{c.p.}$ for positive and negative angles of attack and the noted scatter near zero angle of attack reflect the effect of measuring error with respect to the low values of C_m and C_N . Further examination of these figures shows that there are no significantly unusual effects of bluntness, cylinder length, or flare length on the variation of the aerodynamic characteristics with angle of attack except for the longer 30° flares. (Compare figs. 8 and 9.) This result is compatible with the flow-field analysis of the previous section which showed that the longest 30° flare would be the only one to extend beyond the low-constant energy region near the body. Since the effects of the geometric parameters on the longitudinal aerodynamic characteristics for flares which are embedded in the low-constant energy region near the body are different from the effects for those flares that extend beyond the region, the data for the longest 20° and 30° flares are used to evaluate such effects for the two categories.

Evaluation of Parameters

Effect of nose bluntness.— The effect of blunting the nose manifests itself in three ways: First, through the direct contribution on the nose; second, through the effect on the flow field in the region of the flare; and third, through its effect on the position of the bow-shock—flare-shock intersection relative to the flare. The first effect is the opposite of the other two; blunting the nose increases the axial-force contribution of the nose but its effect on the flow field and of the shock intersection tends to decrease the axial-force contribution of the flare. The direct effect of blunting the nose can be determined from figures 6(a) and 6(b) for the 0° flare. From the figures the value of C_A is seen to double approximately and the increase is, as expected, predictable by Newtonian theory. To determine the effect of blunting on the effectiveness of the flare, the longitudinal aerodynamic characteristics for the two noses are plotted in figure 12 for the longest cylinder ($l_c/D_c = 4.0$) and both the longest 20° and 30° flares ($l_f/D_c = 1.645$). Examination of figures 12(a) and 12(b) shows that for the 20° flare configuration the axial force is higher with the blunt nose but the difference between the two noses has been reduced with the addition of the flare (see fig. 6); however, for the 30° flare the axial force is higher near zero angle of attack for the conical nose configuration. The comparison of the effect of bluntness for the two flares has shown that the results are compatible with the flow-field analysis, that is, the contribution to the axial force of the 30° flare, which extends beyond the low-constant energy region near the body, would be markedly greater and would be more strongly affected by nose bluntness than the contribution of 20° flare, which is within the low energy region near the body. Although it is not shown, the effect of bluntness is more pronounced for the short cylinder and would be expected to be from the flow-field analysis. The aerodynamic coefficients, especially the axial force of the longest 30° flares

are also observed to increase considerably with angle of attack and to deviate considerably from the Newtonian prediction. For the 20° flare, however, the variation of the coefficients from the Newtonian prediction is not as great. A possible explanation for this result can be obtained from an examination of the computed flow-field characteristics in figure 5. The figure shows that as the distance between the body and shock decreases (moving forward on the cylinder) the dynamic pressure distribution remains similar. Analogously, as the shock approaches the lower surface of the body as angle of attack increases, the dynamic-pressure distribution between the body and shock should remain similar and the lower surface of a flare of sufficient radial extent would move into a region of higher energy and stronger energy gradient and thereby would increase the contribution of the surface to the forces. Since the energy of the region near the body remains relatively constant as the distance between the shock and body increases (analogous to moving rearward on the cylinder), the upper portion of the flare would be affected less by angle of attack. The longest 30° flare, which already extends into the higher energy region at zero angle of attack, should be, as it is more strongly affected than the others. Bluntness is seen in figures 13 and 14 to have some influence on the variation of the aerodynamic coefficients with angle of attack; this influence, again, is especially noticeable in the variation of the axial-force coefficient. The explanation for this larger variation is found from the previous analysis of the variation of the dynamic-pressure distribution between the body and shock with angle of attack; it is noted that the energy level near the body is lower for the hemispherical nose than for the conical nose, but near the shock the energy level is nearly equal to that of the conical nose. Therefore, as the flare moves closer to the shock with angle of attack, the increase in the forces should be larger for the hemispherical-nose configuration.

For the long cylinder blunting the nose does not increase the angle of attack at which the bow-shock—flare-shock intersection moves inboard of the flare; but for the short cylinder the angle of attack is increased (figs. 8 and 9).

In summarizing the effects of nose bluntness, it can be said that the longitudinal aerodynamic characteristics of flare stabilized bodies are strongly dependent upon the size of the flare relative to the size of the low energy region near the body caused by the bow shock. The effectiveness of flares which extend beyond this region is more strongly affected by bluntness.

Effect of cylinder length.— Shortening the cylinder affects the aerodynamic characteristics in a number of ways: (1) By changing the moment arm and removing some of the force- and moment-producing cylinder section; (2) by placing the flare in a region of the flow field that has a higher energy level and gradient; (3) by placing the flare closer to the bow shock so that the bow-shock—flare-shock intersection effects occur at a lower angle of attack; and (4) by positioning the flare so that its upper surface is exposed to the flow over a larger angle-of-attack range. Except for the axial-force coefficient at zero angle of attack, two or more of the four effects are influencing the aerodynamic characteristics at all times. At zero angle of attack only the position of the flare in the flow field has an effect on the axial-force coefficient; the flow-field analysis shows that shortening the cylinder from $l_c/D_c = 4.0$ to 1.0

would not be expected to strongly affect the axial force on the longest 20° flare ($l_f/D_c = 1.645$) for either nose but should increase the axial force on the 30° flare of the same length for both noses. Figures 13 and 14 show this effect to be true and to be stronger for the conical-nose configuration.

The influence of the various combinations of effects due to shortening the cylinder on the variation of the coefficients with angle of attack can also be determined from figures 13 and 14. In figure 13 it can be seen that the extended exposure of the upper surface of the 20° flare from $\alpha = 5^\circ$ to $\alpha = 11^\circ$ combined with the change of the flow field between the body and shock does not increase the axial-force coefficient very much; the Newtonian estimates indicate that the effects on normal force and pitching moment beyond those expected from the first effect are not significant. In figure 14, however, the bow-shock—flare-shock intersection effects are seen to override the strong flow-field effect and the extended upper-surface exposure effect. (Note C_A in fig. 14(a).) The shock intersection effects would not be expected to be felt until the intersection moves sufficiently inboard for the expansion fan emanating from the intersection to contact the flare surface. Figure 14 shows that the effect is noticeable within an angle of attack of 3° from the angle at which the shock intersection initially moves into proximity of the flare. Blunting the nose delays the advent of shock intersection effects for the short cylinder by an angle of attack of about 7° . (Compare figs. 14(a) and 14(b).)

Effect of flare angle.— The effect of flare angle in conjunction with flare length has been discussed with respect to the analysis of the flow field and the other test parameters; however, the effects of flare angle for various geometric flare constants are also available from the investigation. Figures 15, 16, and 17 present the longitudinal aerodynamic characteristics for flare length, flare surface area, or flare diameter held constant. For a constant flare length (fig. 15) the forces and moments increase with flare angle for all configurations tested. It is observed that irrespective of nose shape and cylinder length only the aerodynamic characteristics of the 20° and 30° flares show any variation from predicted trends. The 30° flare extends beyond the low energy region near the body at zero angle of attack and is influenced by the strong energy gradient over the whole angle-of-attack range, whereas the 20° flare evidently exceeds the extent only at the higher angles of attack. The characteristics of these two flares are also affected by the bow-shock—flare-shock intersection effects as the cylinder length is decreased. For the constant flare surface area (fig. 16) flare effectiveness increases with flare angle; however, the increase is not as large as that for the constant length comparison. The aerodynamic characteristics of the 20° and 30° flares are influenced by the energy gradient of the flow field near the shock at angle of attack; otherwise, the data follow the trends predicted by Newtonian theory. The lengths of these flares are less than those of the constant length comparison (fig. 15) and neither extends beyond the low energy region at zero angle of attack; however, at angle of attack where the bow shock approaches more closely the flares do extend beyond the low energy region. The 20° and 30° flares are still of sufficient length to have their aerodynamic characteristics affected by the bow-shock—flare-shock intersection as cylinder length is reduced. For the constant flare diameter comparison (fig. 17) the most striking result is the insignificant influence of flare angle on the normal force and pitching moment.

Evidently the increase in pressure coefficient as flare angle increases is balanced by the accompanying decrease in surface area. Since the frontal area is a constant, the axial-force coefficient shows some increase with flare angle. Further examination of the figure reveals that only the 30° flare has its aerodynamic characteristics affected by the flow-field energy gradient as angle of attack increases. This occurs because the 20° and 30° flares are shorter than those of the comparisons of figures 15 and 16. The flares are also short enough not to be influenced by the shock intersection as cylinder length is reduced.

The results of the comparisons of figures 15, 16, and 17 indicate the necessity of knowing the flow-field characteristics and the location of the bow-shock--flare-shock intersection in order to determine the influence of flare parametric changes on the longitudinal aerodynamic characteristics. For those flares which are embedded within the low energy region near the body, the trends of the aerodynamic characteristics are predictable by Newtonian theory; for the larger flares the energy gradients must be accounted for.

The slopes of the normal-force and pitching-moment curves and the axial-force coefficient at zero angle of attack are presented in figure 18 for the various flare geometric constants. Comparison of the measured values and the Newtonian estimates indicates the strong influence of flow separation on $C_{N\alpha}$ and $C_{m\alpha}$ for the 30° flare. The comparison for C_A shows the effect of the flow-field energy gradient and flow separation on that parameter for the same flare.

Estimation of Axial-Force Coefficient at $\alpha = 0^\circ$

The dynamic-pressure distribution between the cylinder and shock are not readily computed or estimated for angles of attack other than 0° ; therefore, only C_A at $\alpha = 0^\circ$ was computed with the effect of the energy level and gradient between the shock and body being accounted for.

For the calculations two flow models were used to compute the contribution of the flare. As was done in reference 24, the flare pressure coefficient was assumed to be the same for the first flow model as it would be on a cone frustum at free-stream Mach number; the bow shock of the nose cylinder only serves to reduce the dynamic pressure but does not alter the pressure distribution. The pressure coefficients of the flares were determined from cone theory at a Mach number of 6.0; the axial-force coefficient was corrected by the ratio of the average dynamic pressure in the flow field immediately ahead of the flare to the free-stream dynamic pressure. The dynamic pressure, averaged with respect to the square of the radius to account for the increase of area with radius for the flares, was obtained from the distribution computed by using axisymmetric characteristics. This method differs from that of reference 24 in which the dynamic pressure was averaged with respect to the radius. In the second flow model the flare surfaces at discrete radii are assumed to act independently and to have a pressure coefficient which is commensurate with the computed Mach number and pressure at that radius in the flow field immediately ahead of the shock at the cylinder-flare junction. Since the flare is known to act as a wedge near

its junction with the cylinder and to change to conical flow along its length, the computation of the pressure distribution along the flare was both two and three dimensional.

Figure 19 presents the computed C_A for all the flares and both noses plotted against the cylinder length. The measured values for the two cylinder lengths of the present investigation are also presented for comparison. As can be seen from the figure, the values of C_A computed at discrete radii by using the values of Mach number and pressure immediately ahead of the shock at the cylinder-flare junction, in general, follow expected trends; that is, for the flares which do not extend very far above the cylinder surface (low angle or short flares) the axial-force coefficient is better predicted by the two-dimensional flow estimates since the flow over the flare near the cylinder-flare junction is two dimensional. This result is true for the 10° and some 20° flares. As the flare angles or lengths are increased the effect of three-dimensional flow becomes more extensive. This effect is shown by the overprediction of C_A for the longer high-angle flares by the two-dimensional calculation and by the close agreement with the conical values. The calculations of C_A made with \bar{q} are, in general, consistent with the discrete-radii conical-flow calculation. From the agreement between the end points it can be seen that the method using the average \bar{q} appears to give a good prediction of the trends of C_A with cylinder length and gives estimates of the values within 10 percent for all but one of the 30° flare configurations investigated.

CONCLUDING REMARKS

The forebody geometry utilized in these tests introduced a sizable region of low dynamic pressure about the models. The extent of this low energy region increased as the nose bluntness increased. For flares small enough to be embedded in this low energy region the trends of the effects of nose bluntness, cylinder length, and flare angle are predictable by Newtonian theory. In general, however, the values of the force and moment coefficients are overpredicted. For flares large enough to extend beyond this low energy region, the aerodynamic characteristics are significantly affected by the strong dynamic pressure gradient between the low energy region and the bow shock (which increases flare effectiveness) and under certain conditions bow-shock--flare-shock intersection effects (which decrease flare effectiveness). The effects of these phenomena are, of course, not predicted by Newtonian theory. The onset of these bow-shock--flare-shock intersection effects is delayed by an angle of attack of about 7° by increasing the nose bluntness and cylinder length. Boundary-layer separation occurred on the larger flare angles at low angles of attack; however, the significant effects due to separation are confined to the normal-force and pitching-moment curves below an angle of attack of about 5° .

Because of the large variation of the local dynamic pressure between the body and the shock, comparison of flare effectiveness on the basis of constant length, surface area, or diameter depends on the size of the flares. With the flare sizes used in this investigation, flare effectiveness increased with flare angle when the flare length was held constant, and also to a lesser extent with

constant flare surface area. Although some of this increase is to be expected from purely geometric consideration, the effectiveness of the larger flares was also influenced by the strong energy gradient region. For the constant-diameter comparison the flares were all embedded in the low-constant energy region so that only the axial-force coefficient was affected by flare angle. The normal force and pitching moment were not affected because the increase in pressure with flare angle was nearly balanced by the decrease in the surface area. It should be noted that these results may be altered somewhat if different size flares are used.

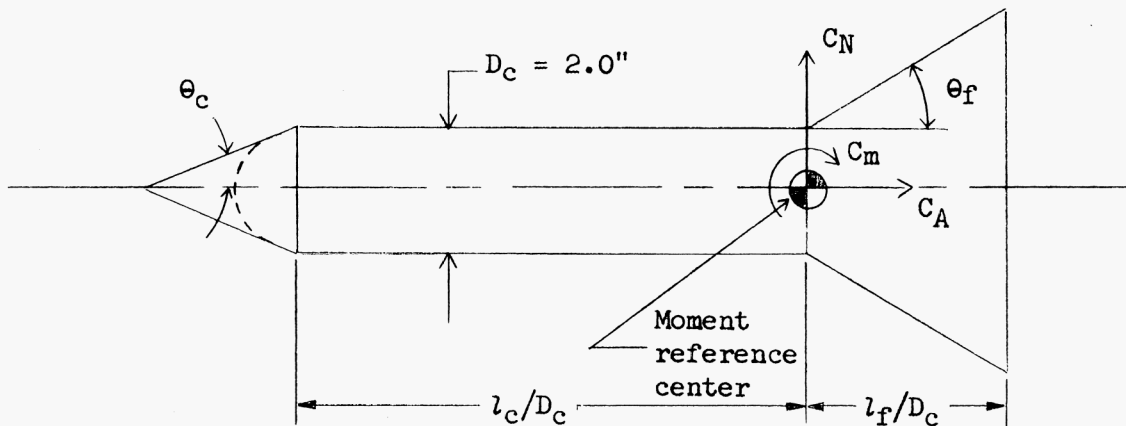
At zero angle of attack the axial-force coefficient for the 30° flares was generally estimated to within 10 percent by using the flow-field properties at the cylinder-flare junction computed by axisymmetric characteristic theory.

Langley Research Center,
National Aeronautics and Space Administration,
Langley Station, Hampton, Va., January 7, 1965.

REFERENCES

1. Mugler, John P., Jr.: Transonic Wind-Tunnel Investigation of the Static Longitudinal Aerodynamic Characteristics of Five Nose Cones Designed for Supersonic Impact. NASA TM X-432, 1961.
2. Morris, Odell A.; and Keith, Arvid L., Jr.: Experimental Investigation of Pressure Distribution and Static Aerodynamic Characteristics for Three Supersonic-Impact Ballistic Reentry Shapes at Mach Numbers of 1.93, 2.55, and 3.05. NASA TM X-453, 1961.
3. Shaw, David S.; and Reed, James D.: Wind-Tunnel Investigation at Mach Numbers From 1.47 to 4.62 of Static Aerodynamic Characteristics of Twelve Nose Cones Designed for Supersonic Impact. NASA TM X-545, 1961.
4. Carraway, Ausley B.; Turner, Kenneth L.; and Crowder, Janette M.: Effects of Afterbody Shape on the Aerodynamic Characteristics of a Fineness-Ratio-10 Cone-Cylinder Configuration at Mach Numbers From 1.57 to 4.65 Including Design Parameter Curves for Circular Afterbody Flares. NASA TM X-348, 1960.
5. Kehlet, Alan B.: Some Effects of Reynolds Number on the Stability of a Series of Flared-Body and Blunted-Cone Models at Mach Numbers From 1.62 to 6.86. NACA RM L57J29, 1958.
6. Rittenhouse, L. E.; and Kaupp, H., Jr.: Influence of Several Shape Parameters on the Aerodynamics of Ballistic Re-Entry Configurations. AEDC-TR-60-13, U.S. Air Force, December 1960.
7. Randall, R. E.; and Kayser, L. D.: Pressure and Force Tests of Several AVCO and GE Re-Entry Models at Mach Number 8. AEDC-TN-59-115, U.S. Air Force, October 1959.
8. Morris, Odell A.: Aerodynamic Characteristics in Pitch of Six Ballistic Reentry Models at a Mach Number of 10.03. NASA TM X-750, 1963.
9. Whiting, Ellis E.; and Carros, Robert J.: Free-Flight Investigation of the Static Stability and Aerodynamic Drag of Three Blunt-Nosed Cylinder-Flare Test Bodies at Mach Numbers From 13 to 17. NASA TM X-500, 1961.
10. Short, Barbara J.; Whiting, Ellis E.; Kruse, Robert L.; and Malcolm, Gerald N.: A Comparison of the Hypersonic Static Stability Characteristics of Blunt- and Pointed-Nosed Slender Entry Vehicles. NASA TM X-850, 1963.
11. Sterrett, James R.; and Emery, James C.: Extension of Boundary-Layer-Separation Criteria to a Mach Number of 6.5 by Utilizing Flat Plates With Forward-Facing Steps. NASA TN D-618, 1960.

12. Ashby, George C., Jr.; and Fitzgerald, Paul E., Jr.: Longitudinal Stability and Control Characteristics of Missile Configurations Having Several Highly Swept Cruciform Fins and a Number of Trailing-Edge and Fin-Tip Controls at Mach Numbers From 2.21 to 6.01. NASA TM X-335, 1961.
13. Goldberg, Theodore J.; Ashby, George C., Jr.; and Hondros, James G.: Center-Line Pressure Distributions on Two-Dimensional Bodies With Leading-Edge Angles Greater Than That for Shock Detachment at Mach Number 6 and Angles of Attack up to 25° . NASA TN D-1793, 1963.
14. Dennis, David H.: The Effects of Boundary-Layer Separation Over Bodies of Revolution With Conical Tail Flares. NACA RM A57I30, 1957.
15. Gray, J. Don: Boundary Layer Separation Effects on the Static Stability of a Flared-Tail Missile Configuration at $M = 2$ to 5. AEDC-TN-60-103, U.S. Air Force, June 1960.
16. Seiff, Alvin; and Whiting, Ellis: The Effect of the Bow Shock Wave on the Stability of Blunt-Nosed Slender Bodies. NASA TM X-377, 1960.
17. Fitzgerald, Paul E., Jr.: The Effect of Bow-Shock—Flare-Shock Interaction on the Static Longitudinal Stability of Flare-Stabilized Bodies at Hypersonic Speeds. NASA TM X-664, 1962.
18. Becker, John V.; and Korycinski, Peter F.: Heat Transfer and Pressure Distribution at a Mach Number of 6.8 on Bodies With Conical Flares and Extensive Flow Separation. NASA TN D-1260, 1962. (Supersedes NACA RM L56F22.)
19. Crawford, Davis H.: The Effect of Air Bleed on the Heat Transfer and Pressure Distribution on 30° Conical Flares at a Mach Number of 6.8. NASA TM X-439, 1961.
20. Sterrett, James R.; and Emery, James C.: Experimental Separation Studies for Two-Dimensional Wedges and Curved Surfaces at Mach Numbers of 4.8 to 6.2. NASA TN D-1014, 1962.
21. Gray, J. Don: A Correlation of Axisymmetric Laminar Flow Separation Characteristics. Paper No. 64-475, Am. Inst. Aeron. Astronaut., July 1964.
22. Bertram, Mitchel H.: Exploratory Investigation of Boundary-Layer Transition on a Hollow Cylinder at a Mach Number of 6.9. NACA Rept. 1313, 1957. (Supersedes NACA TN 3546.)
23. Holloway, Paul F.; and Sterrett, James R.: Effect of Controlled Surface Roughness on Boundary-Layer Transition and Heat Transfer at Mach Numbers of 4.8 and 6.0. NASA TN D-2054, 1964.
24. Laurenson, D. I.: A Semi-Empirical Method for Preliminary Estimation of the Drag of Axisymmetric Ballistic Re-Entry Vehicles. Aerodyn. Data Mem. No. 1:24, Missile and Space Vehicle Dept., Gen. Elec. Co., July 1960.



Noses: Sharp cone ($\theta_c = 22.5^\circ$) and hemispherical

Midbody lengths: $l_c/D_c = 1.0$ and 4.0

Flares $\theta_f = 0^\circ$; $l_f/D_c = 1.0, 2.0,$ and 3.0

$\theta_f = 10^\circ$; $l_f/D_c = 1.0, 1.645, 2.0,$ and 3.0

$\theta_f = 20^\circ$; $l_f/D_c = 0.968, 1.355,$ and 1.645

$\theta_f = 30^\circ$; $l_f/D_c = 0.610, 1.130,$ and 1.645

Flares for constant flare parameters

Constant length, $l_f/D_c = 1.645$		Constant surface area, $S_f/A = 8.62$		Constant diameter, $D_f/D_c = 1.705$	
θ_f	l_f/D_c	θ_f	l_f/D_c	θ_f	l_f/D_c
10°	1.645	10°	1.645	10°	2.000
20°	1.645	20°	1.355	20°	.968
30°	1.645	30°	1.130	30°	.610

Figure 1.- Nominal dimensions of model components and positive directions of forces and moments.

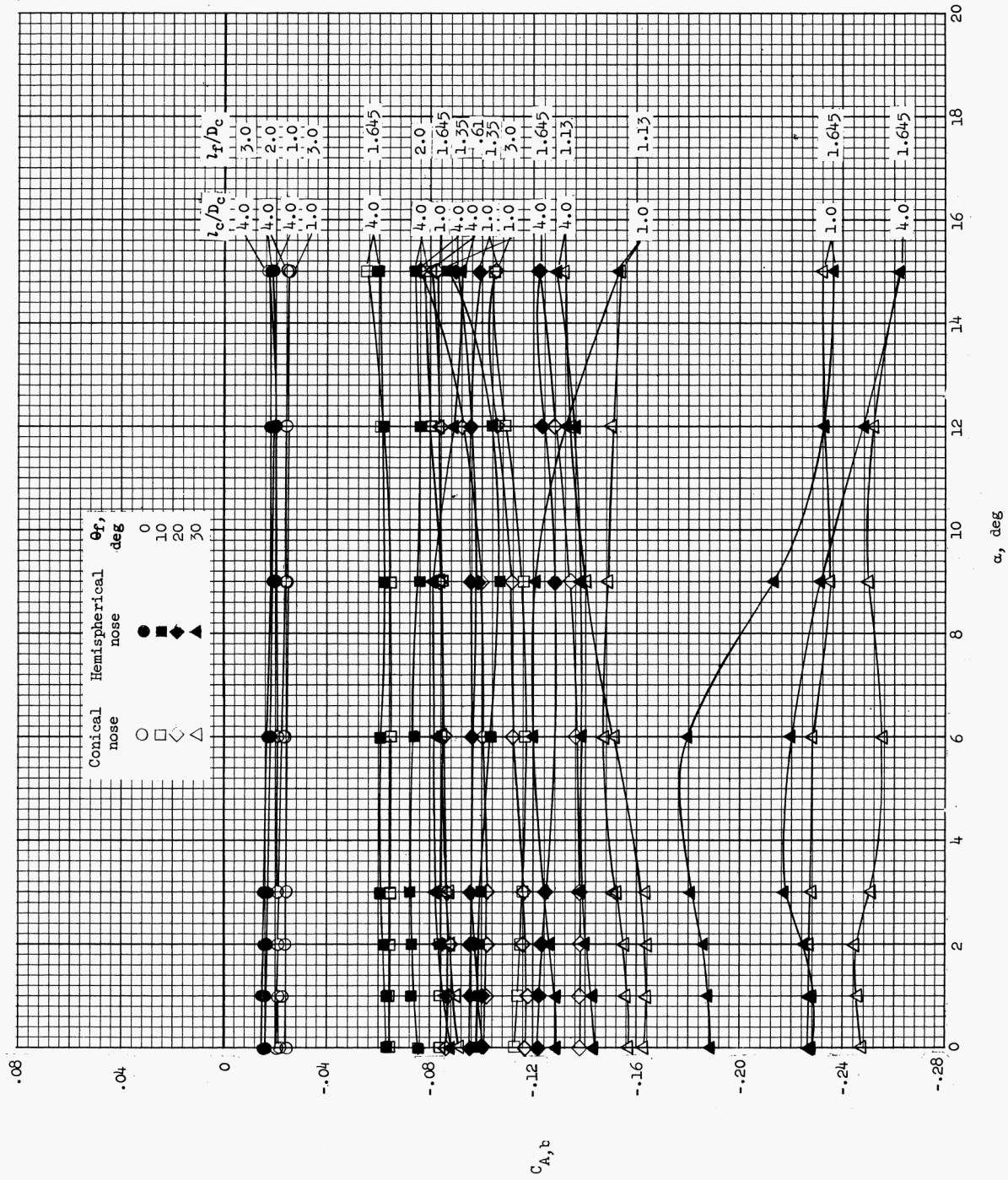
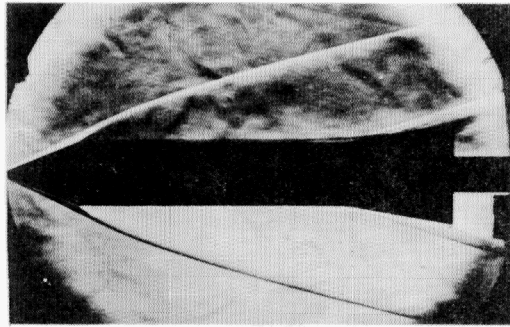
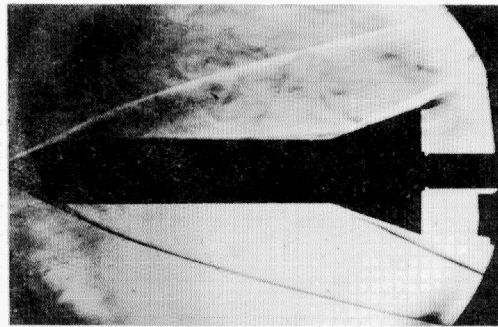


Figure 2.- Variation of axial-force coefficient with angle of attack and cylinder and flare lengths.

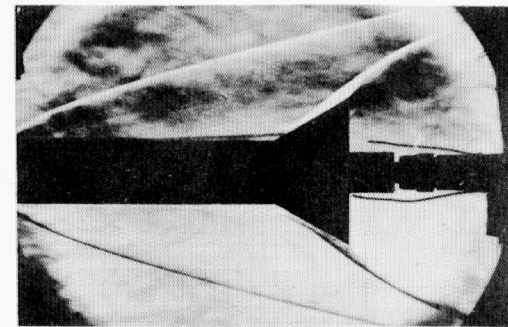


$\theta_f = 10^\circ$

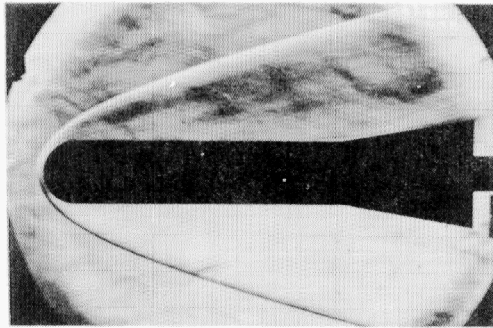


$\theta_f = 20^\circ$

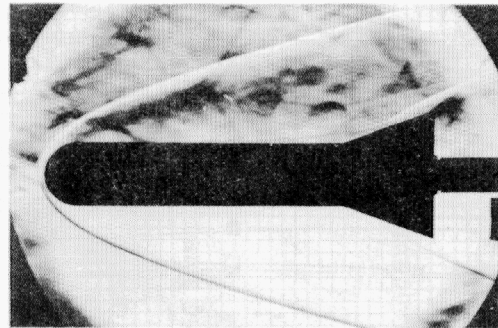
(1) Conical nose.



$\theta_f = 30^\circ$

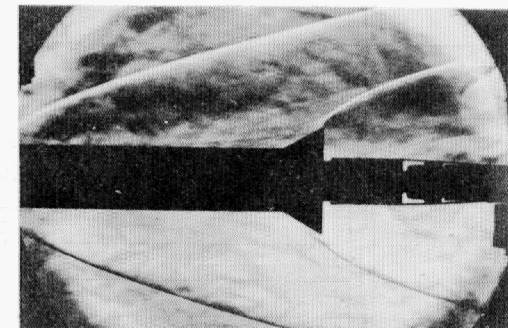


$\theta_f = 10^\circ$



$\theta_f = 20^\circ$

(2) Hemispherical nose.

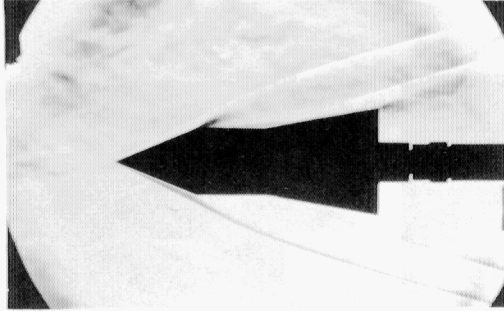


$\theta_f = 30^\circ$

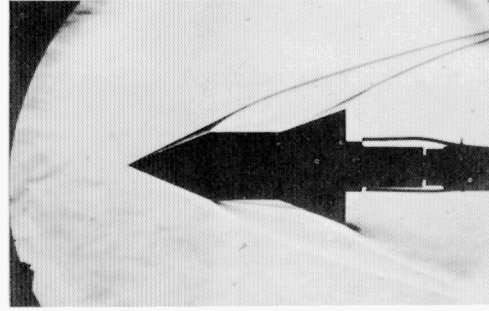
(a) $\lambda_c/D_c = 4.0$.

L-65-27

Figure 3.- Schlieren photographs showing variation of boundary-layer separation with flare angle and nose shape.

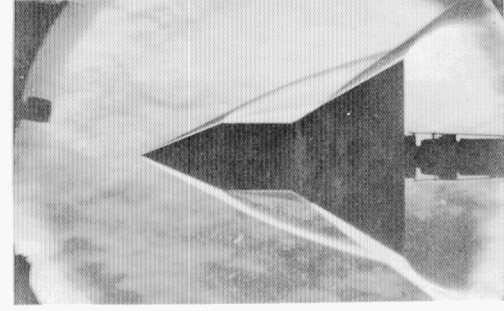


$\theta_f = 10^\circ$

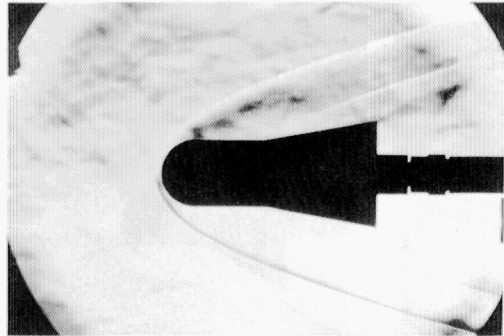


$\theta_f = 20^\circ$

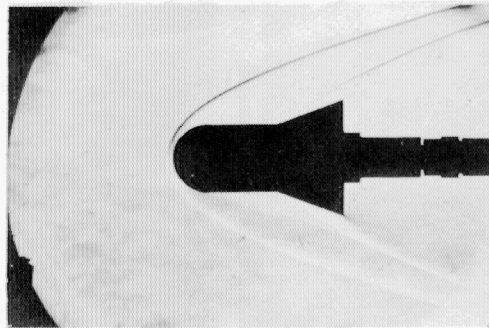
(1) Conical nose.



$\theta_f = 30^\circ$

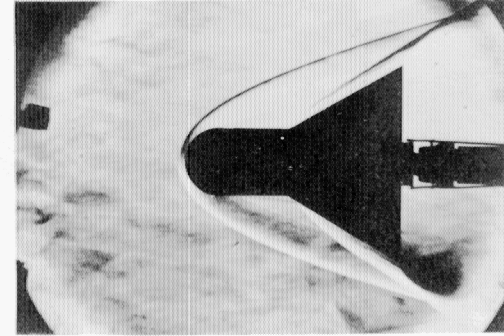


$\theta_f = 10^\circ$



$\theta_f = 20^\circ$

(2) Hemispherical nose.



$\theta_f = 30^\circ$

(b) $l_c/D_c = 1.0$.

Figure 3.- Concluded.

L-65-28

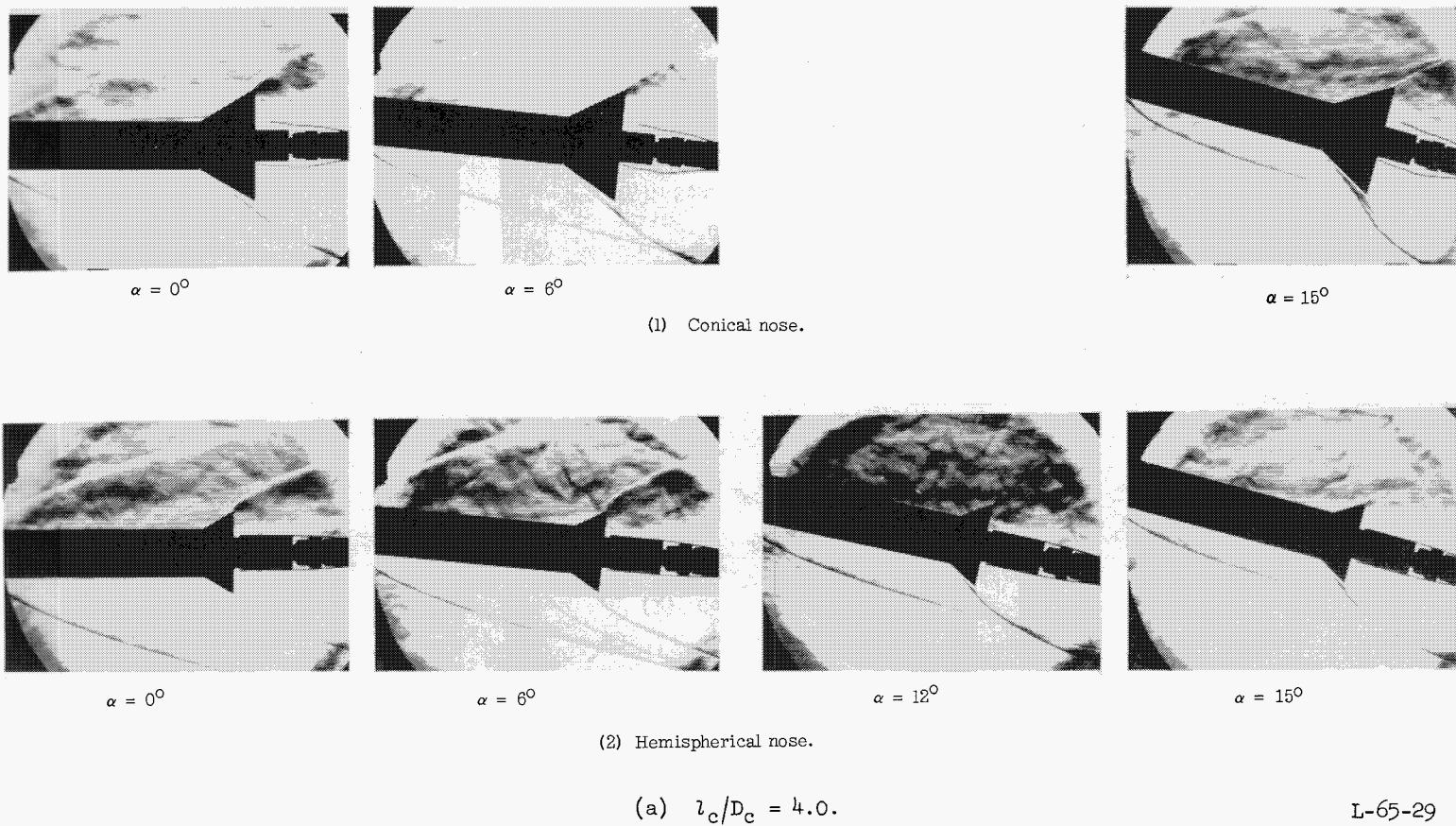


Figure 4.- Schlieren photographs showing variation of boundary-layer separation and the bow-shock-flare-shock intersection position with angle of attack for $\theta_F = 30^\circ$.



$\alpha = 150^\circ$



$\alpha = 120^\circ$



$\alpha = 60^\circ$



$\alpha = 0^\circ$

(1) Conical nose.



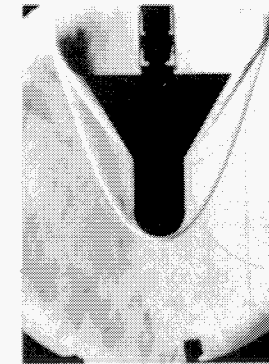
$\alpha = 150^\circ$



$\alpha = 120^\circ$



$\alpha = 60^\circ$



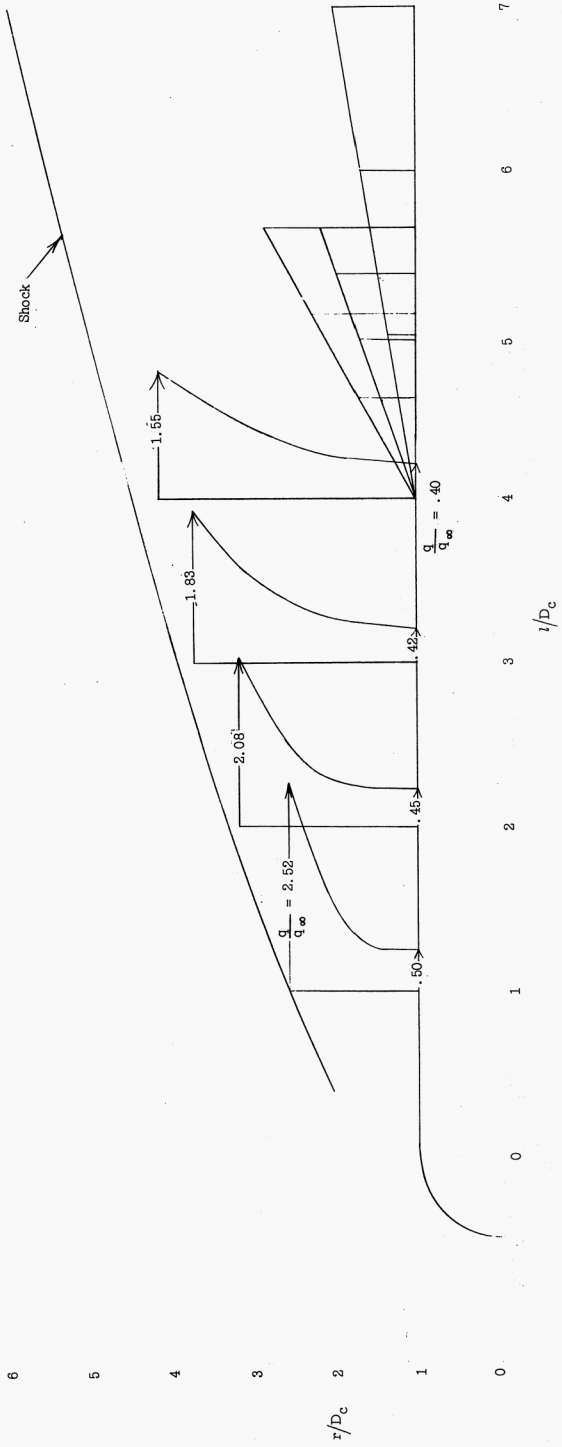
$\alpha = 0^\circ$

(2) Hemispherical nose.

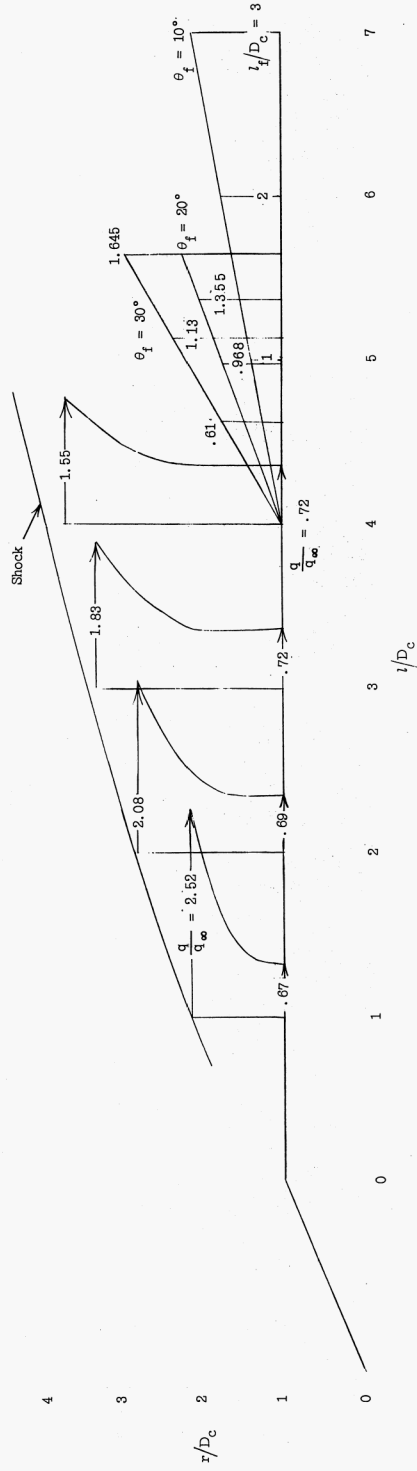
(b) $r_c/D_c = 1.0$.

L-65-30

Figure 4.- Concluded.

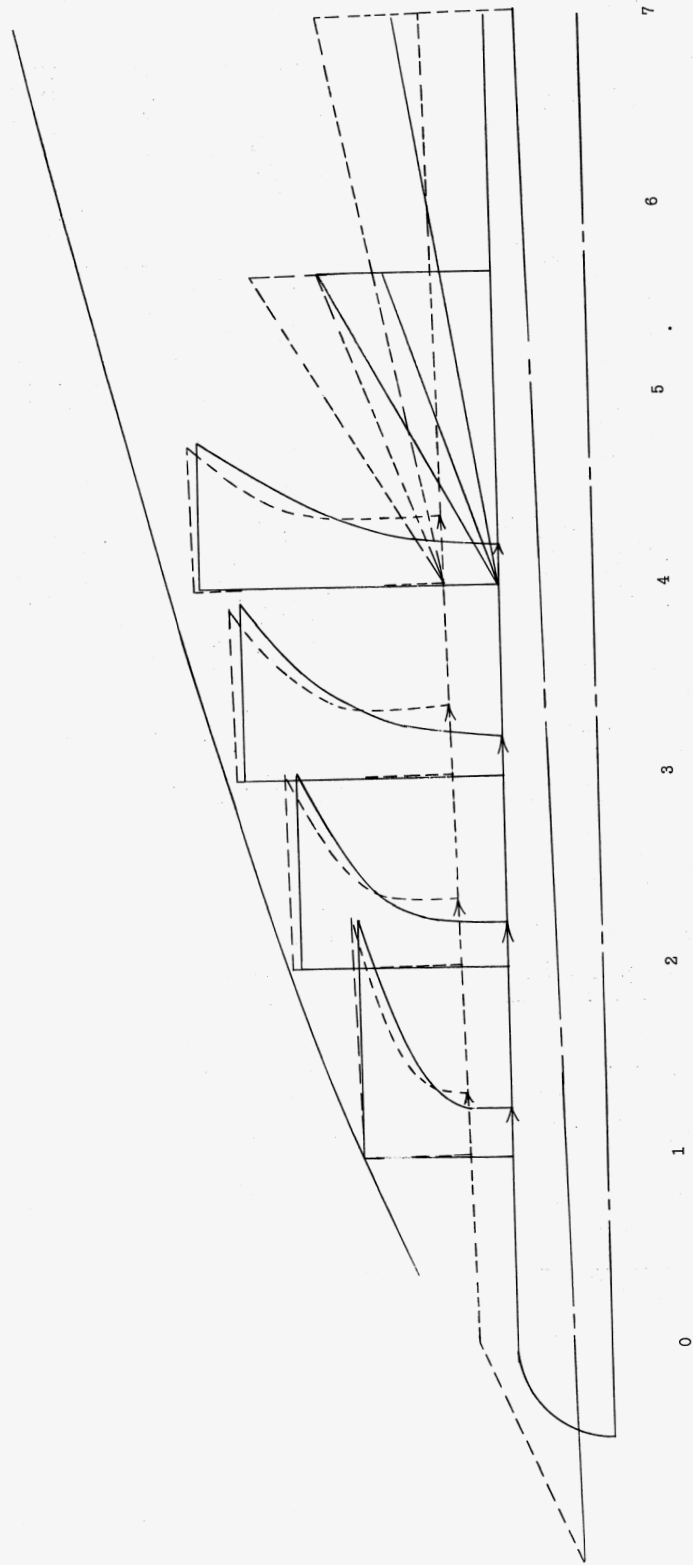


(a) Hemisphere-cylinder-flare configuration.



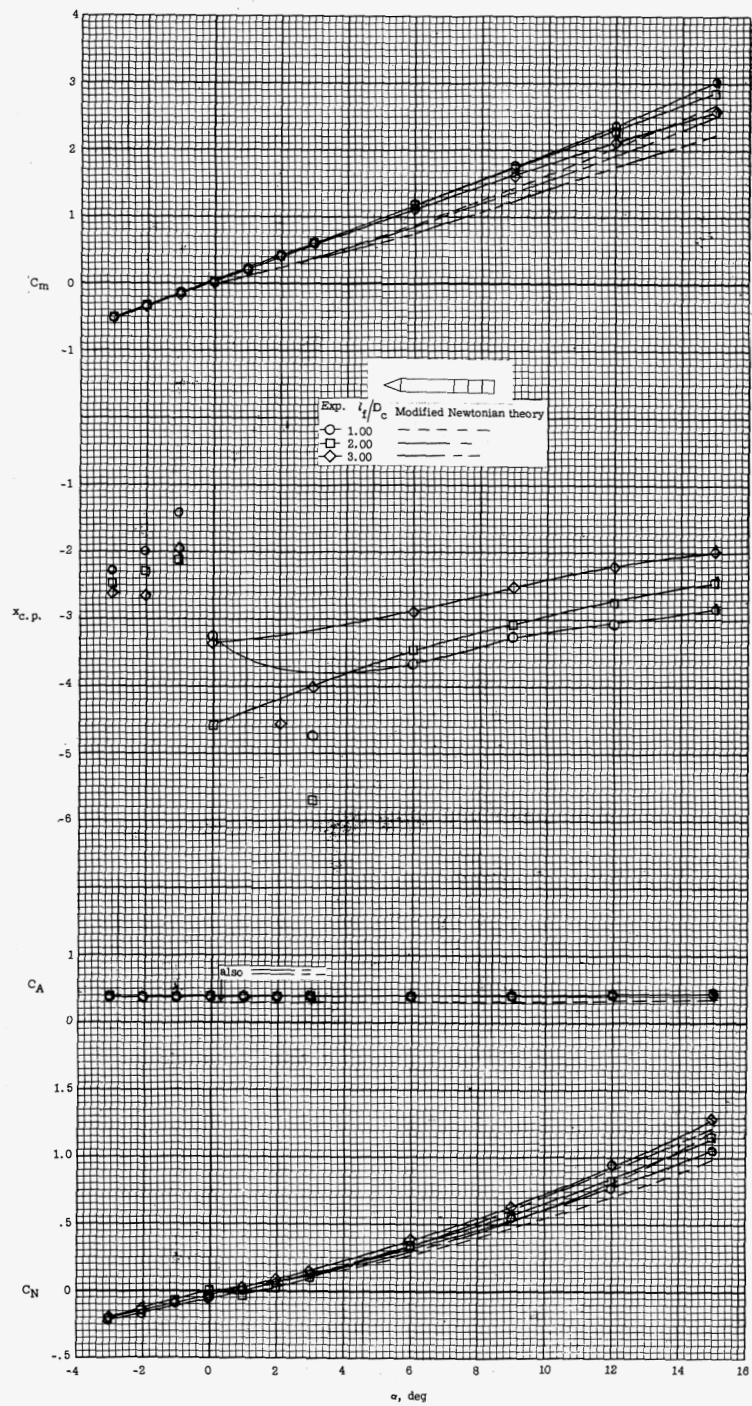
(b) Cone-cylinder-flare configuration.

Figure 5.- Distributions of normalized dynamic pressure in flow field at zero angle of attack computed by method of characteristics.



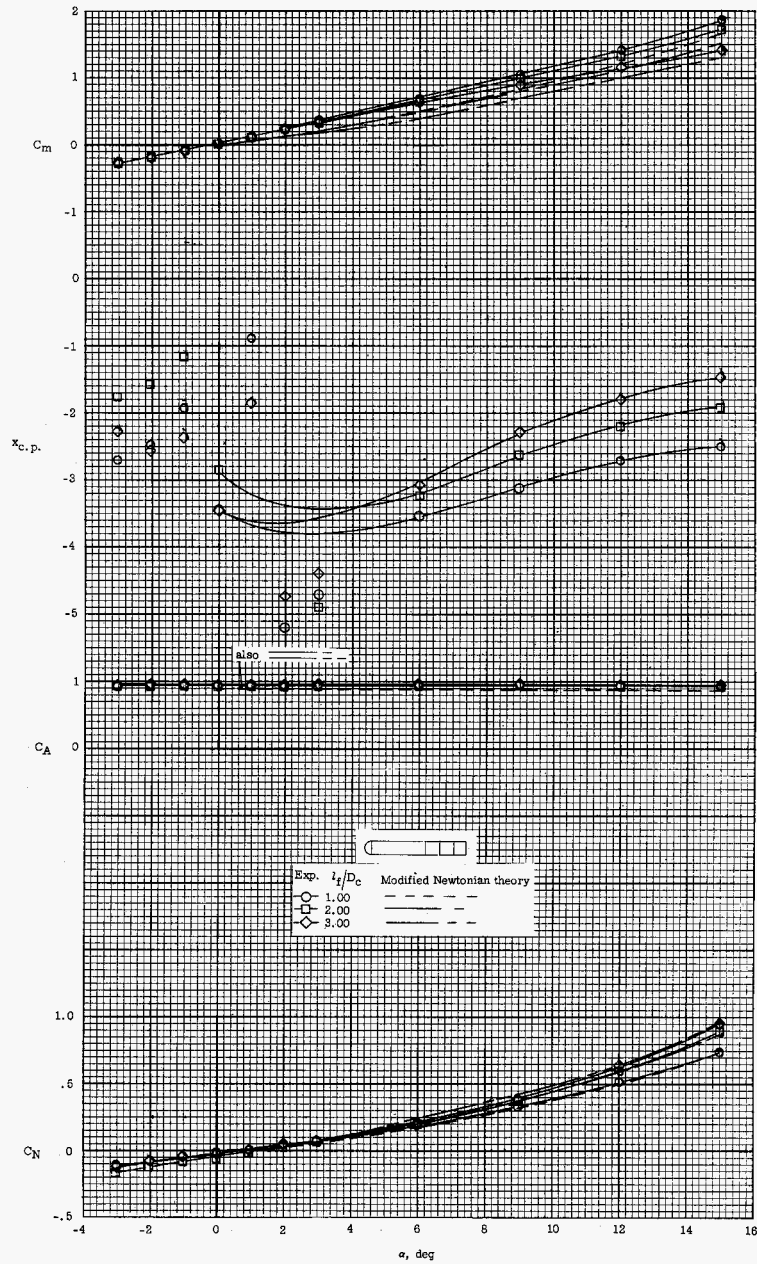
(c) Fields superimposed - shocks coincident.

Figure 5.- Concluded.



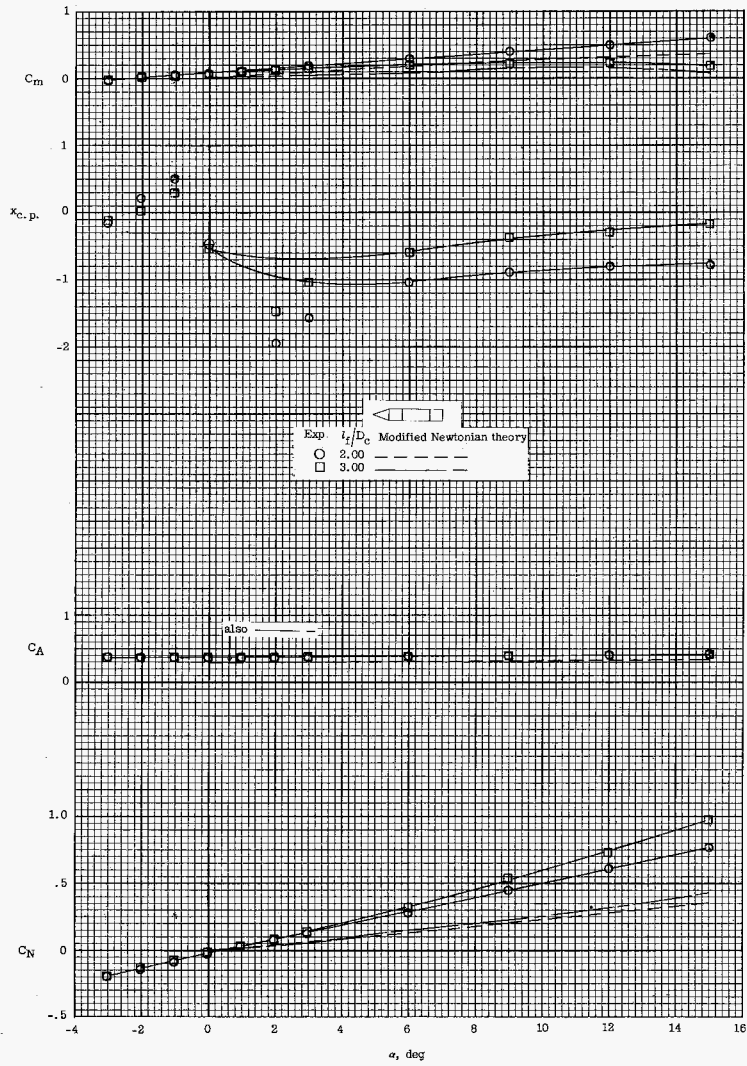
(a) Conical nose, $l_c/D_c = 4.0$.

Figure 6.- Variation of the longitudinal aerodynamic characteristics with angle of attack for 0° flared bodies.



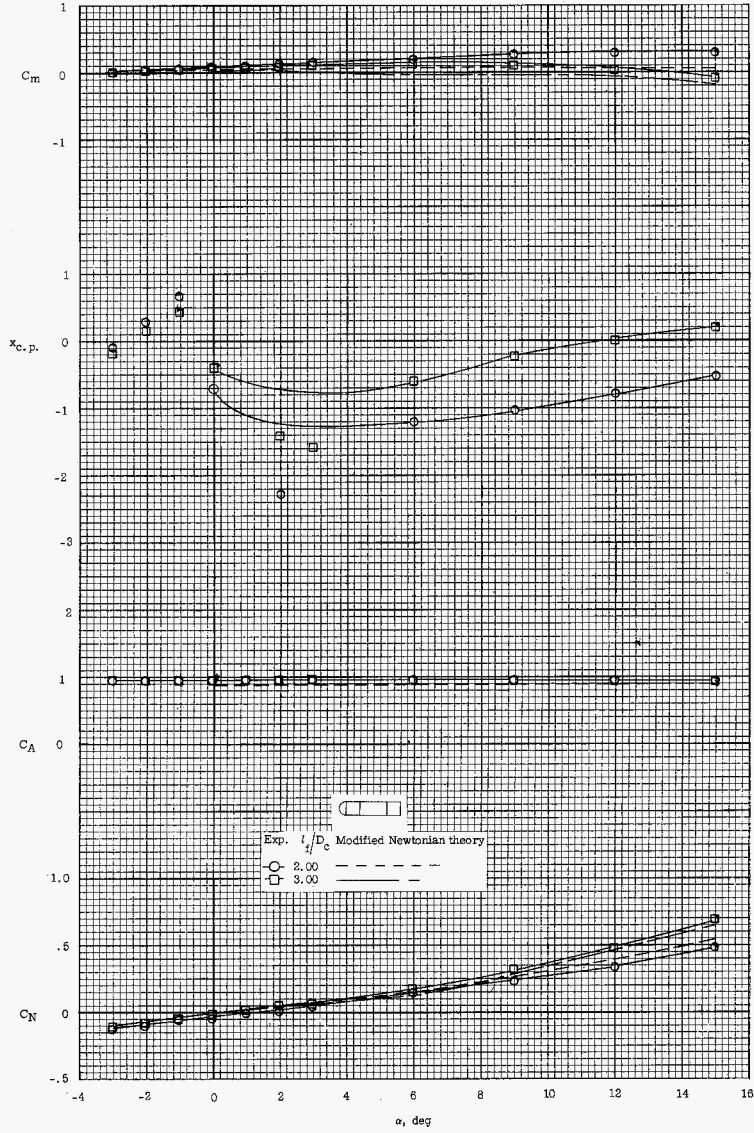
(b) Hemispherical nose, $l_c/D_c = 4.0$.

Figure 6.- Continued.



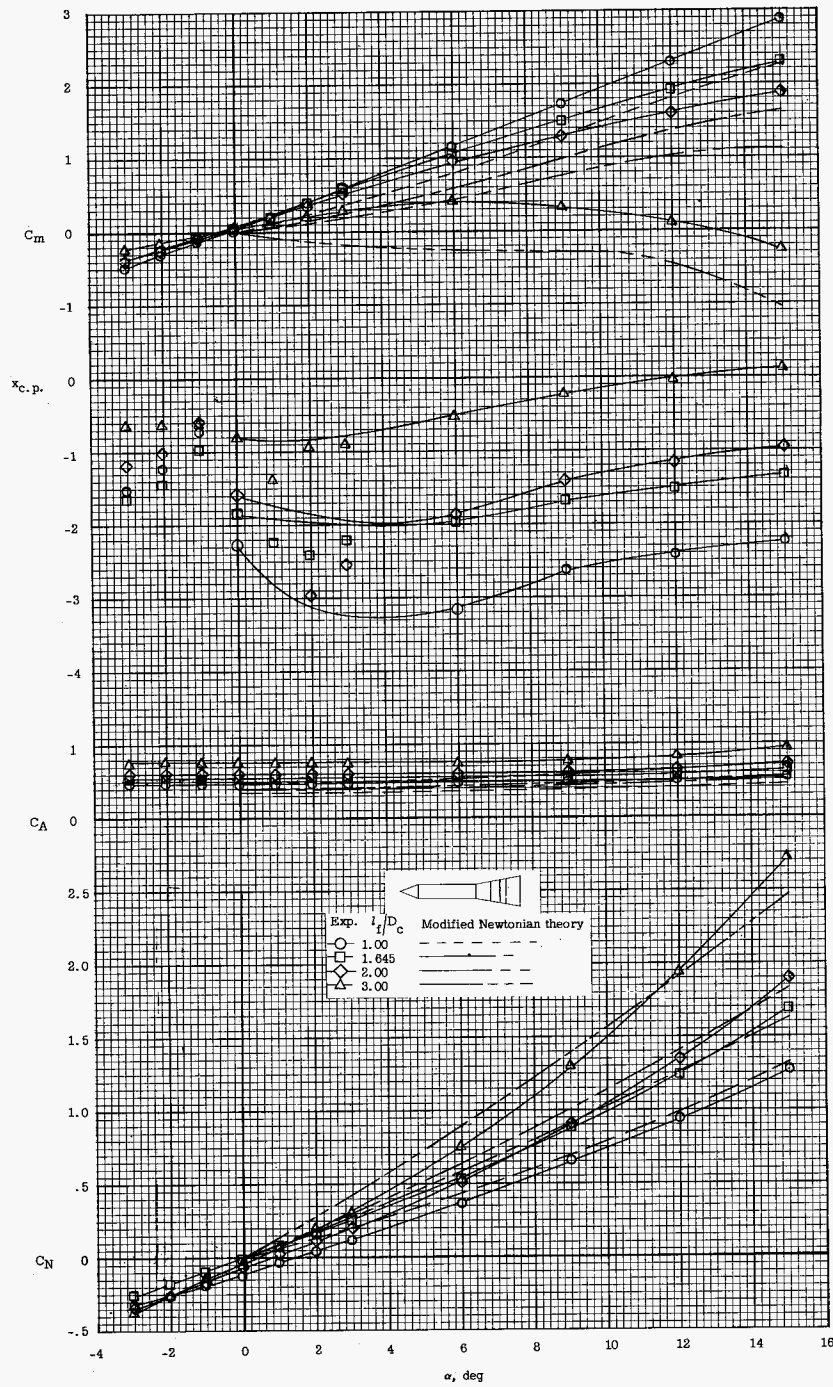
(c) Conical nose, $\lambda_c/D_c = 1.0$.

Figure 6.- Continued.



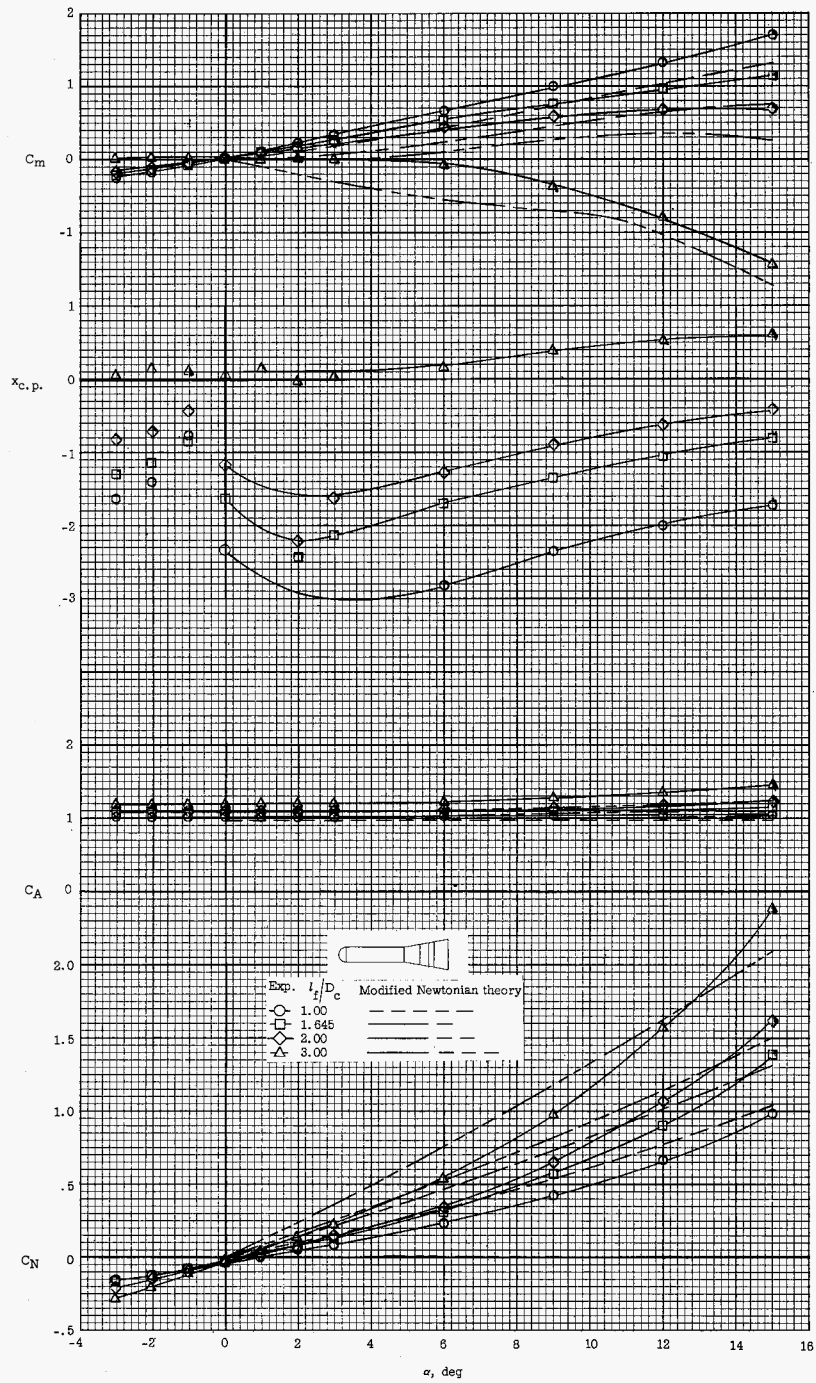
(d) Hemispherical nose, $l_c/D_c = 1.0$.

Figure 6.- Concluded.



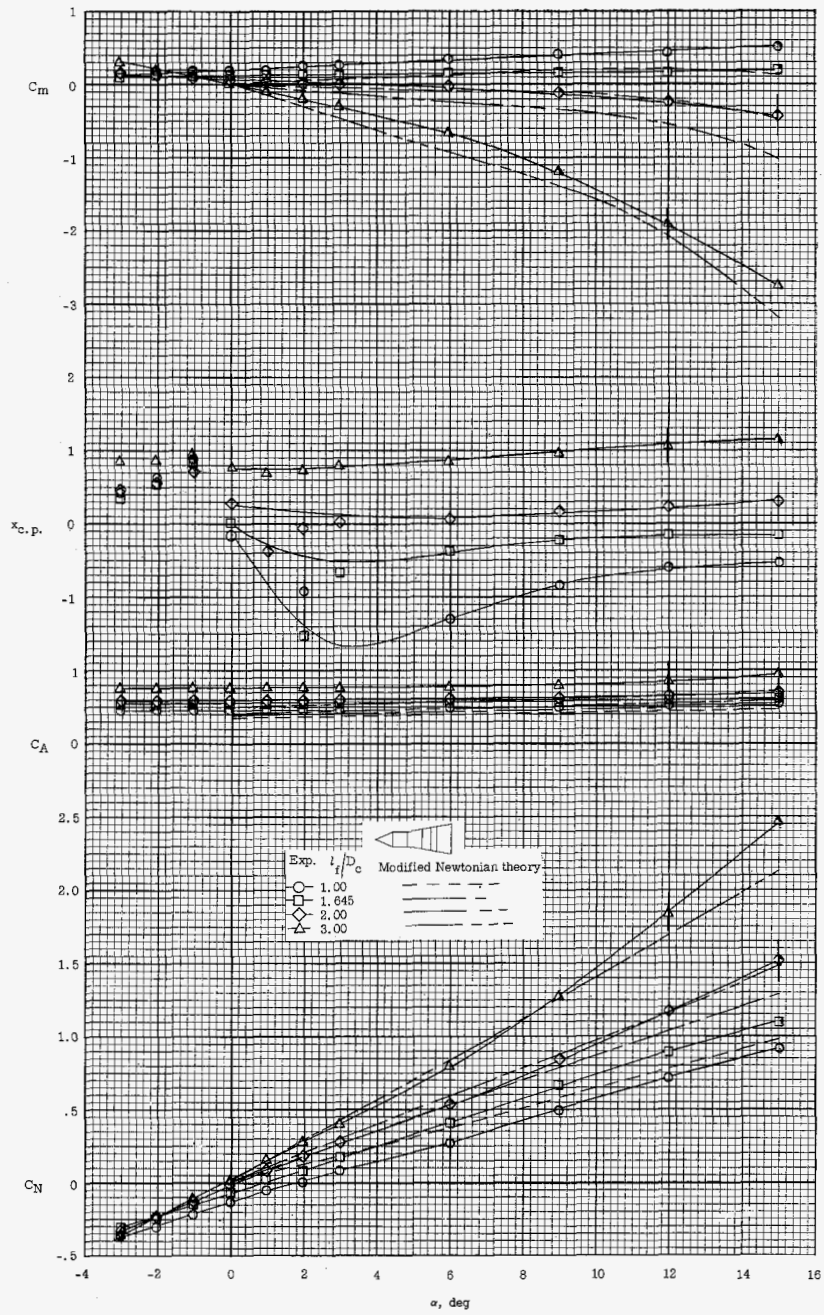
(a) Conical nose, $l_c/D_c = 4.0$.

Figure 7.- Variation of longitudinal aerodynamic characteristics with angle of attack for 10° flared bodies.



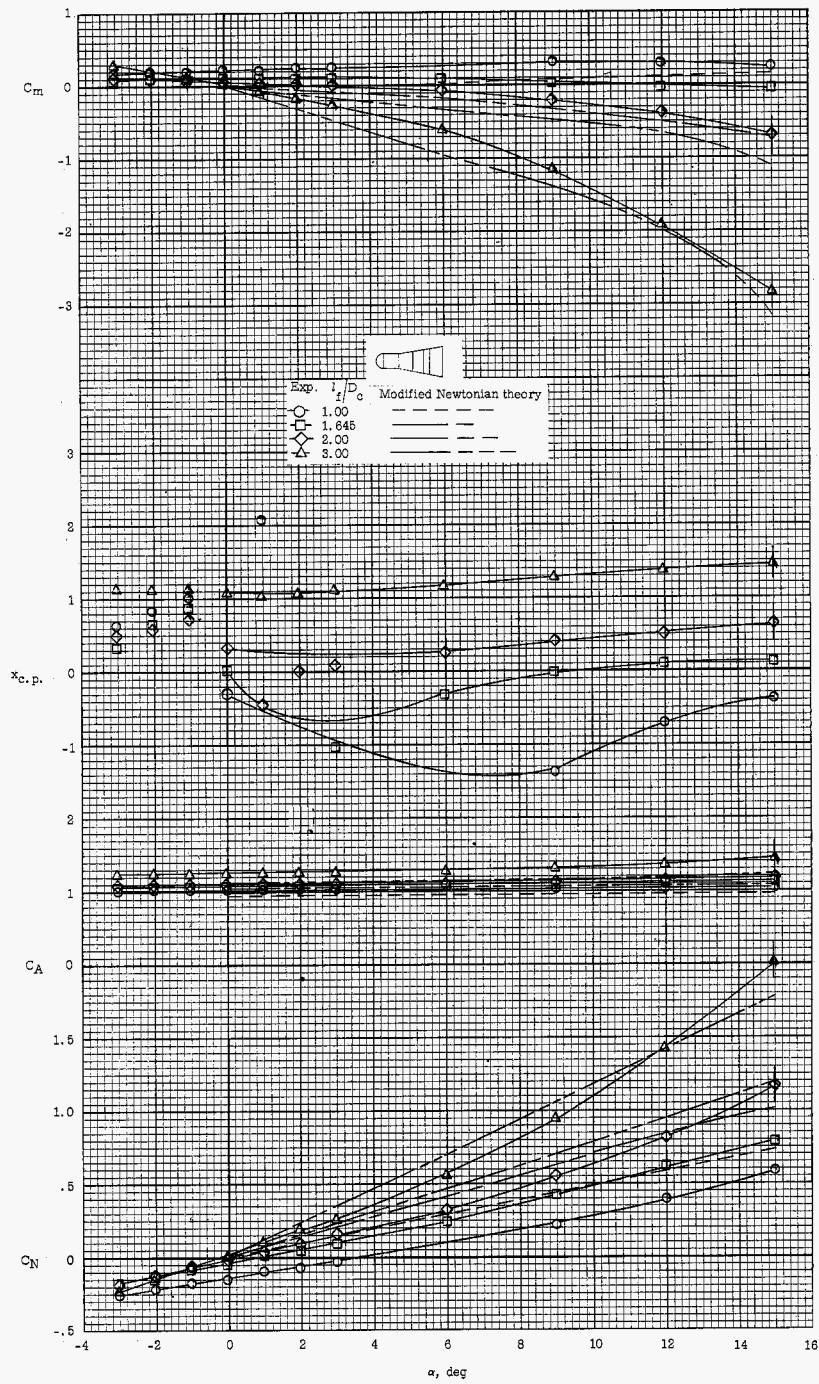
(b) Hemispherical nose, $l_c/D_c = 4.0$.

Figure 7.- Continued.



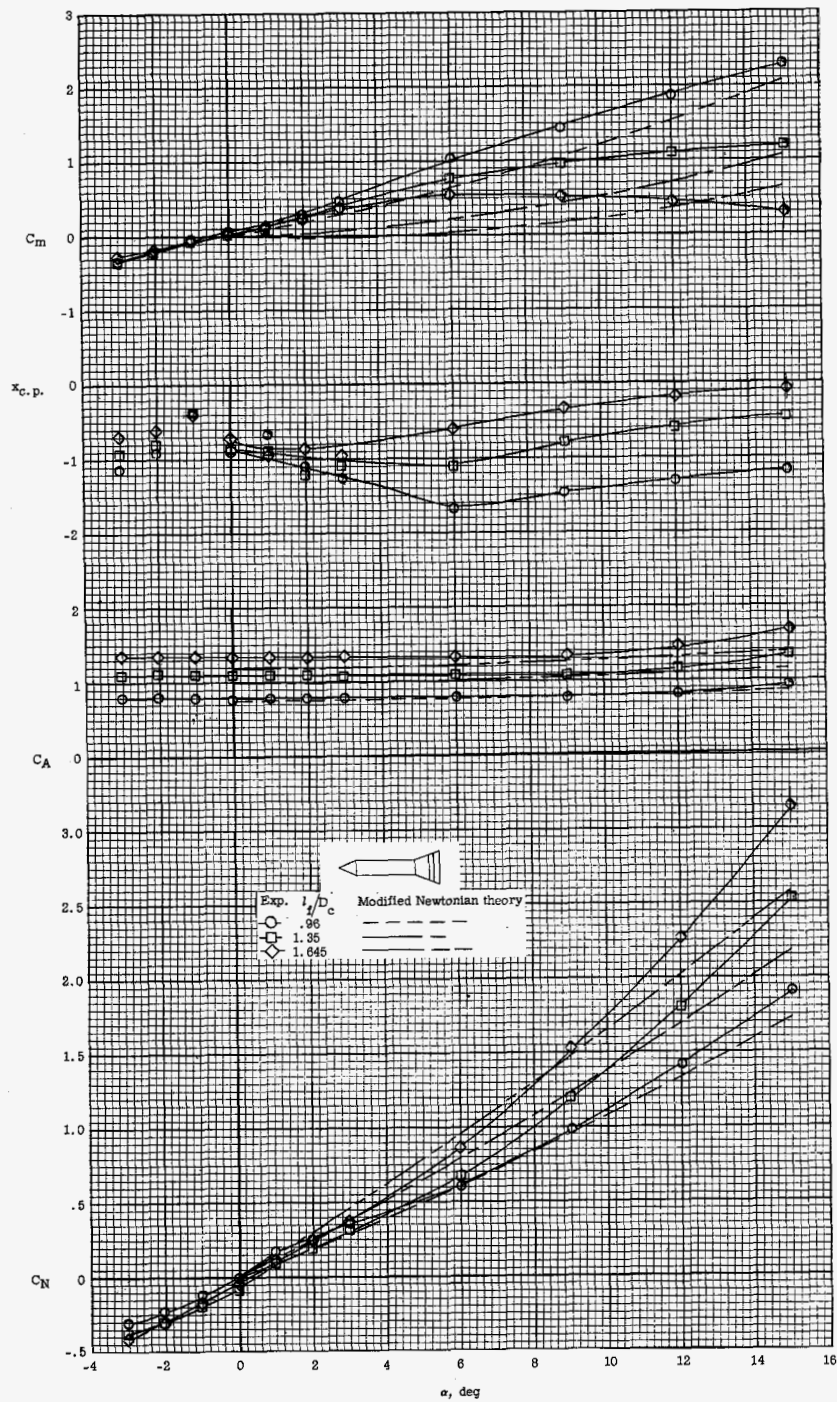
(c) Conical nose, $l_c/D_c = 1.0$.

Figure 7.- Continued.



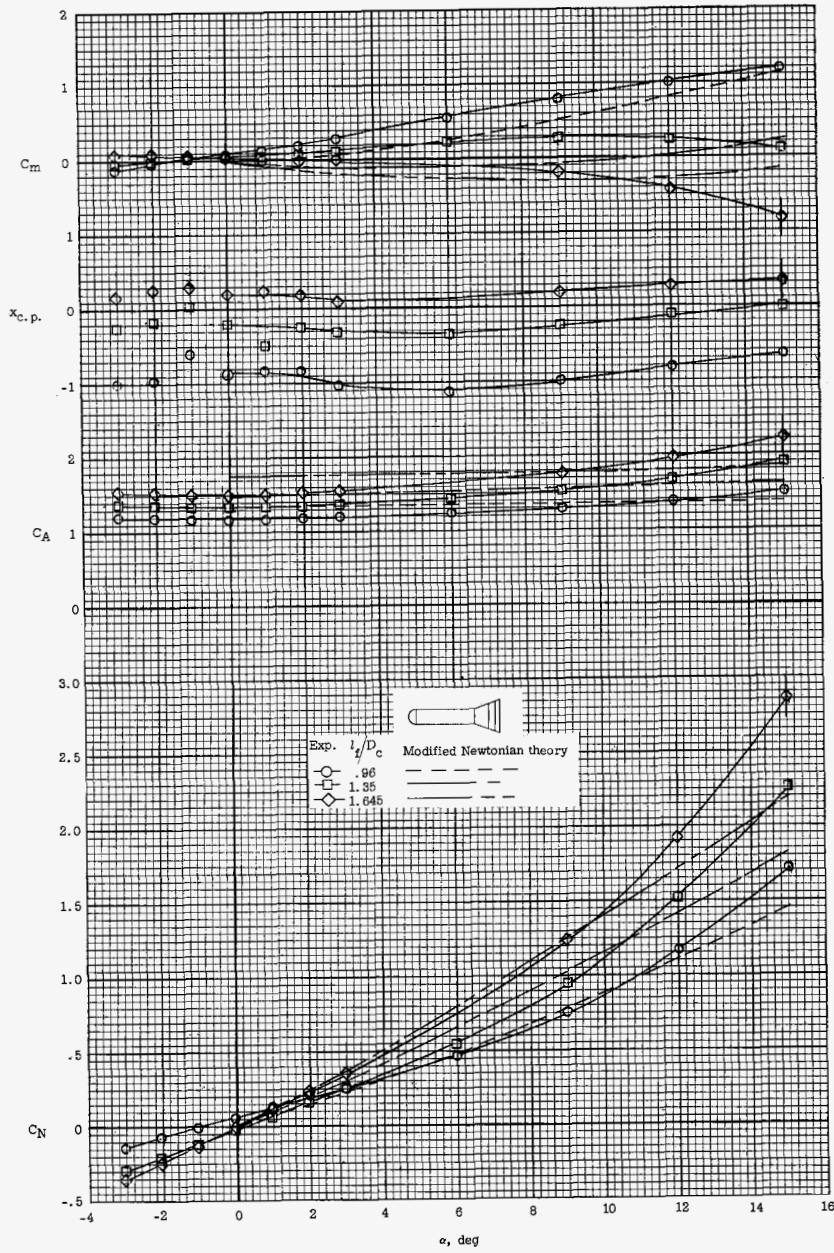
(d) Hemispherical nose, $l_c/D_c = 1.0$.

Figure 7.- Concluded.



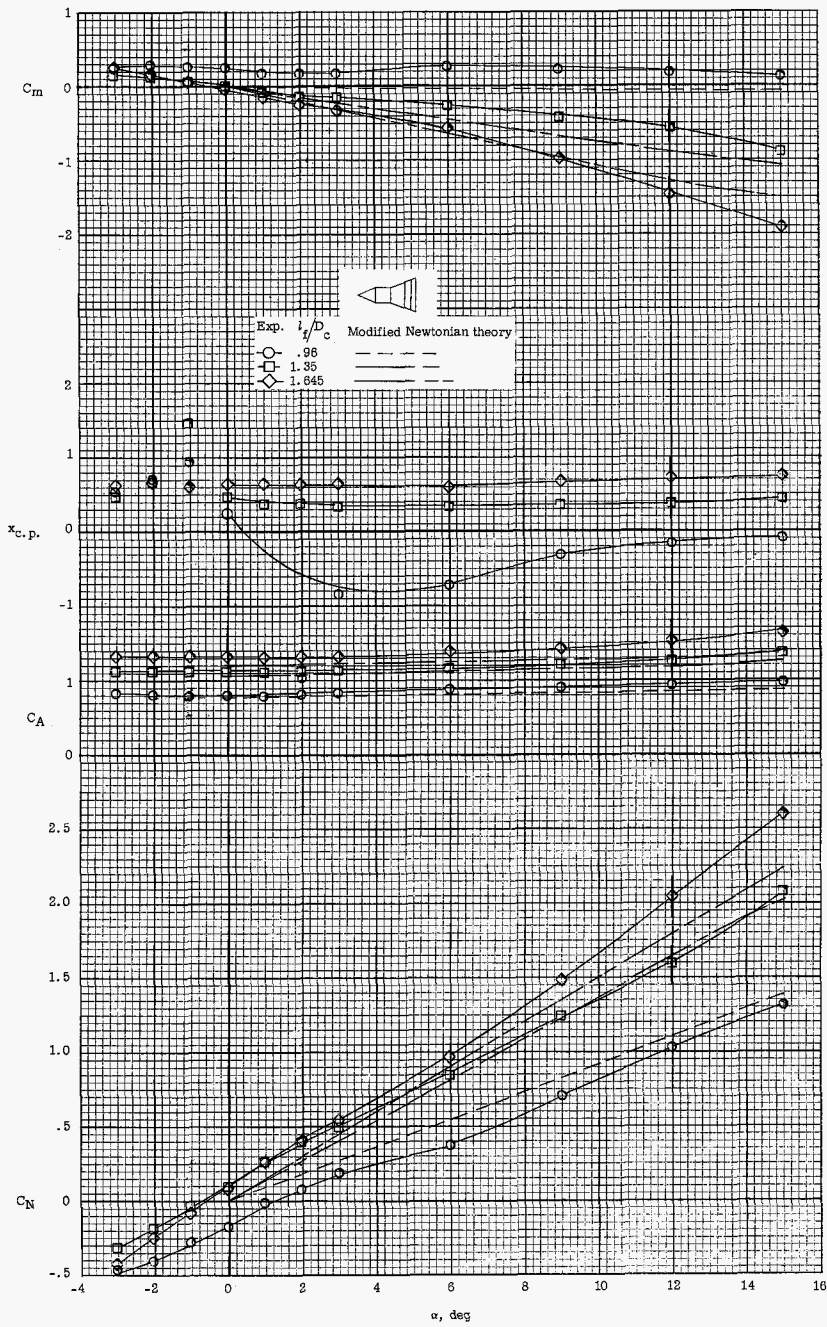
(a) Conical nose, $l_c/D_c = 4.0$.

Figure 8.- Variation of longitudinal aerodynamic characteristics with angle of attack for 20° flared bodies.



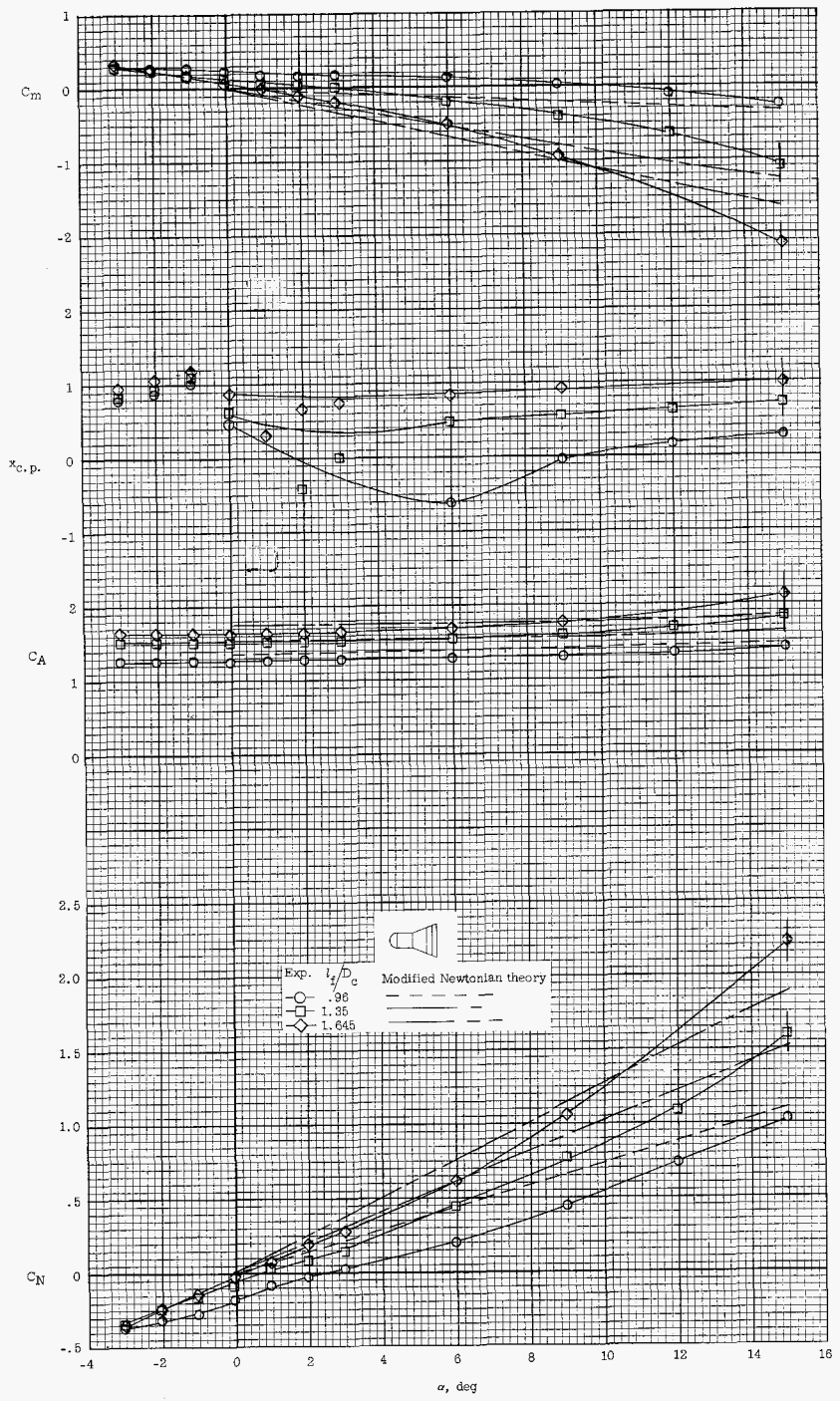
(b) Hemispherical nose, $l_c/D_c = 4.0$.

Figure 8.- Continued.



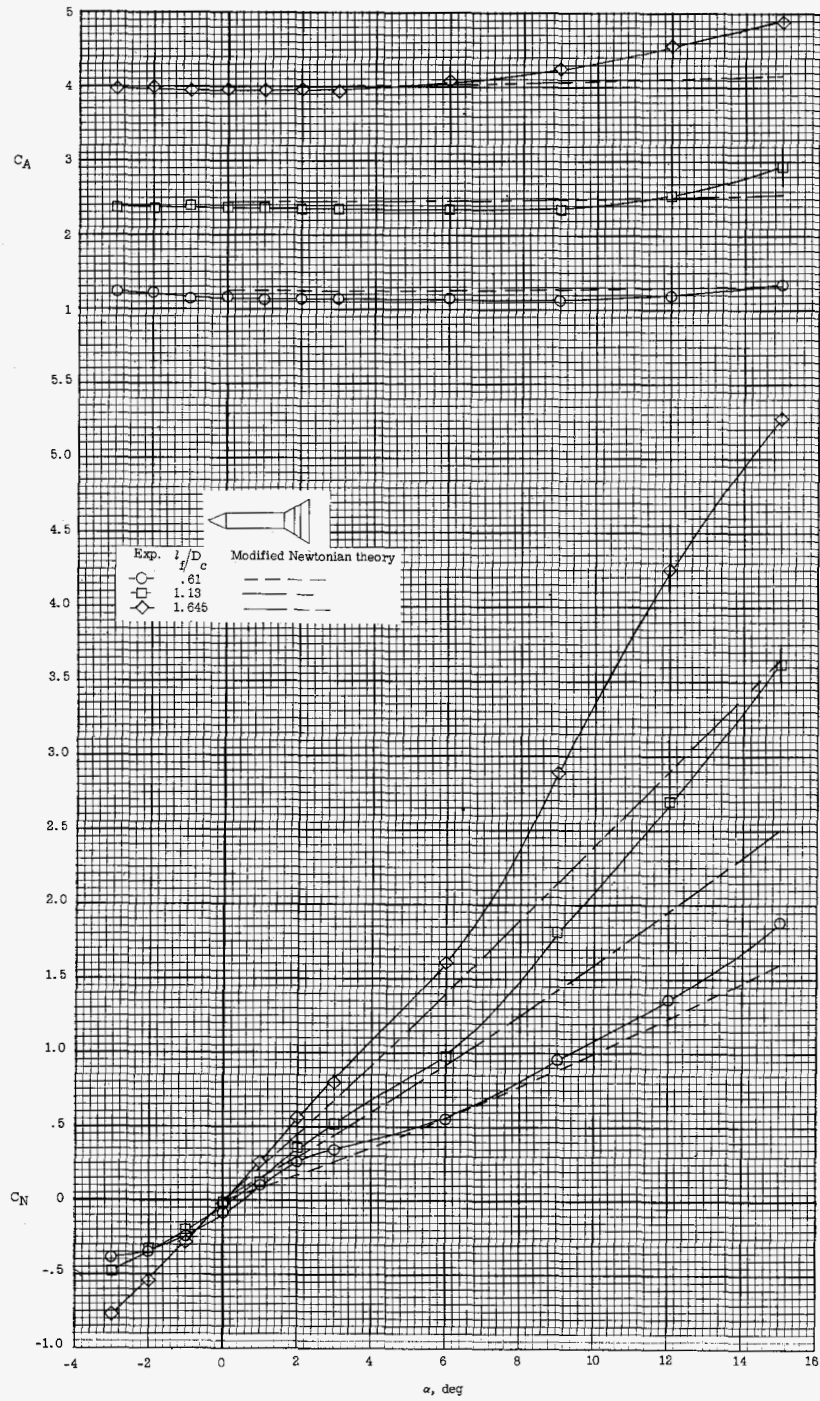
(c) Conical nose, $l_c/D_c = 1.0$.

Figure 8.- Continued.



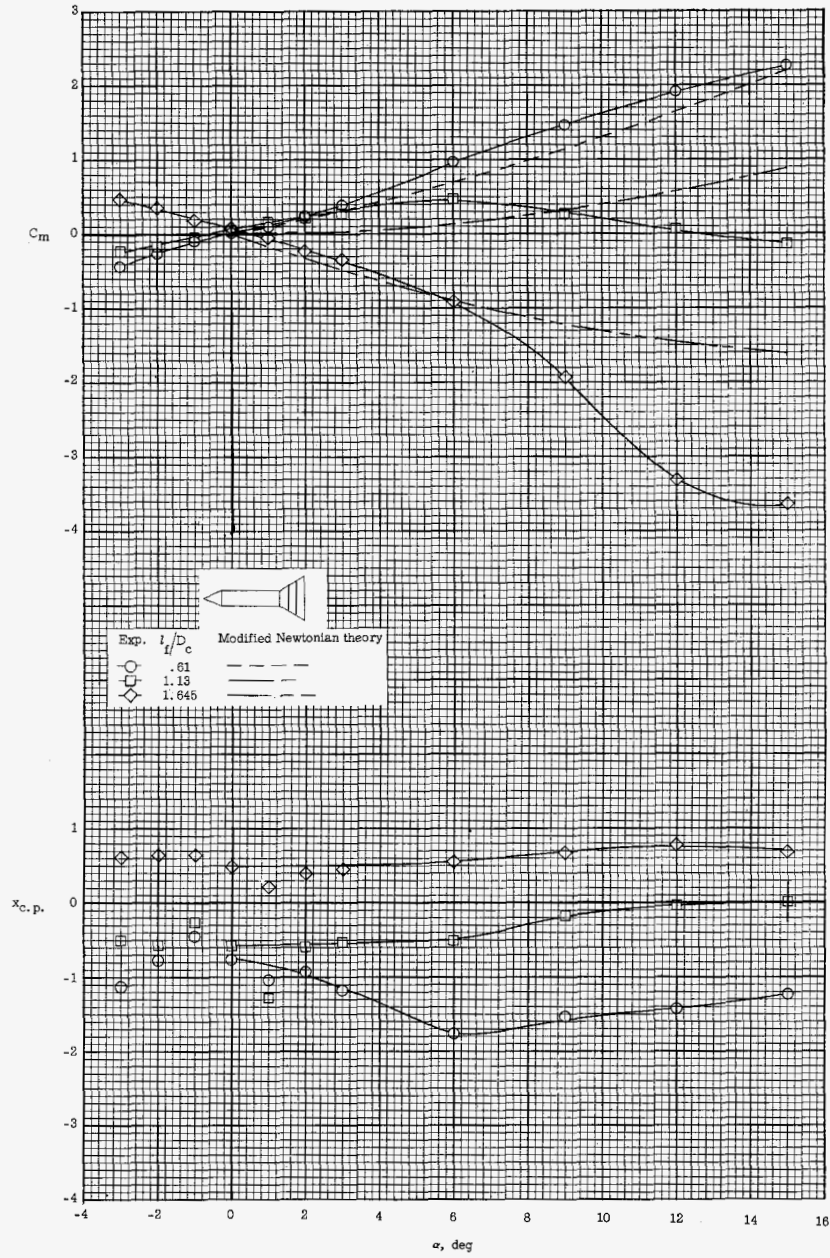
(d) Hemispherical nose, $l_c/D_c = 1.0$.

Figure 8.- Concluded.



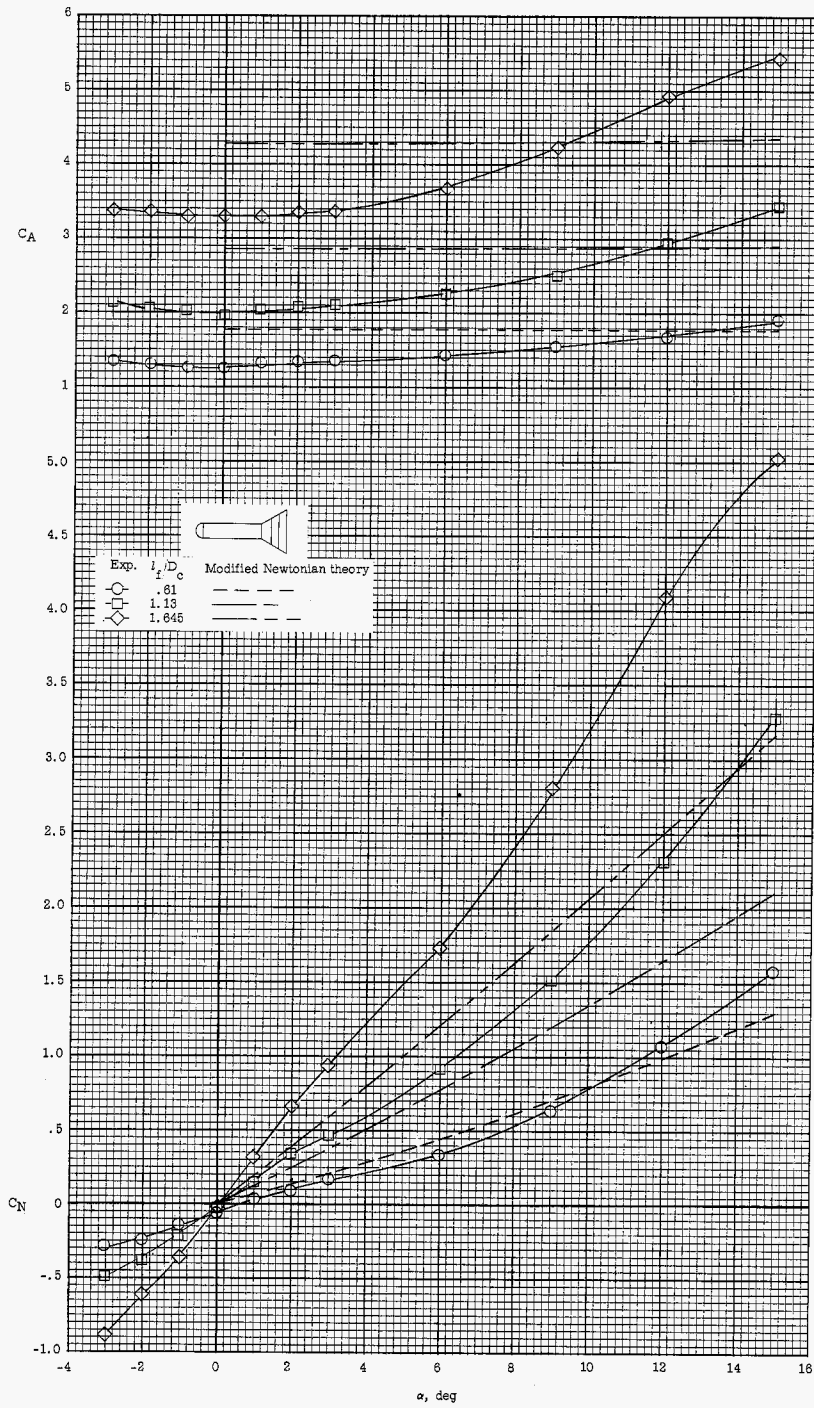
(a) Conical nose, $l_c/D_c = 4.0$.

Figure 9.- Variation of longitudinal aerodynamic characteristics with angle of attack for 30° flared bodies.



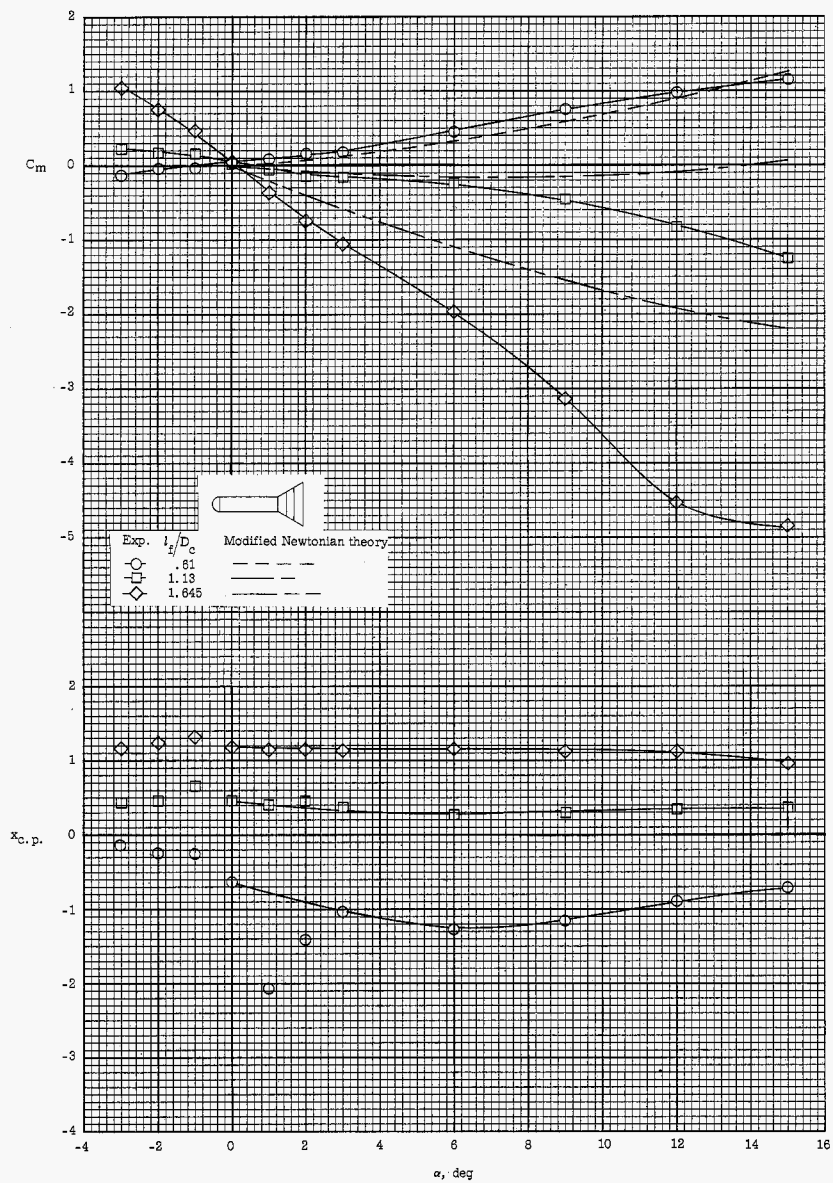
(a) Concluded.

Figure 9.- Continued.



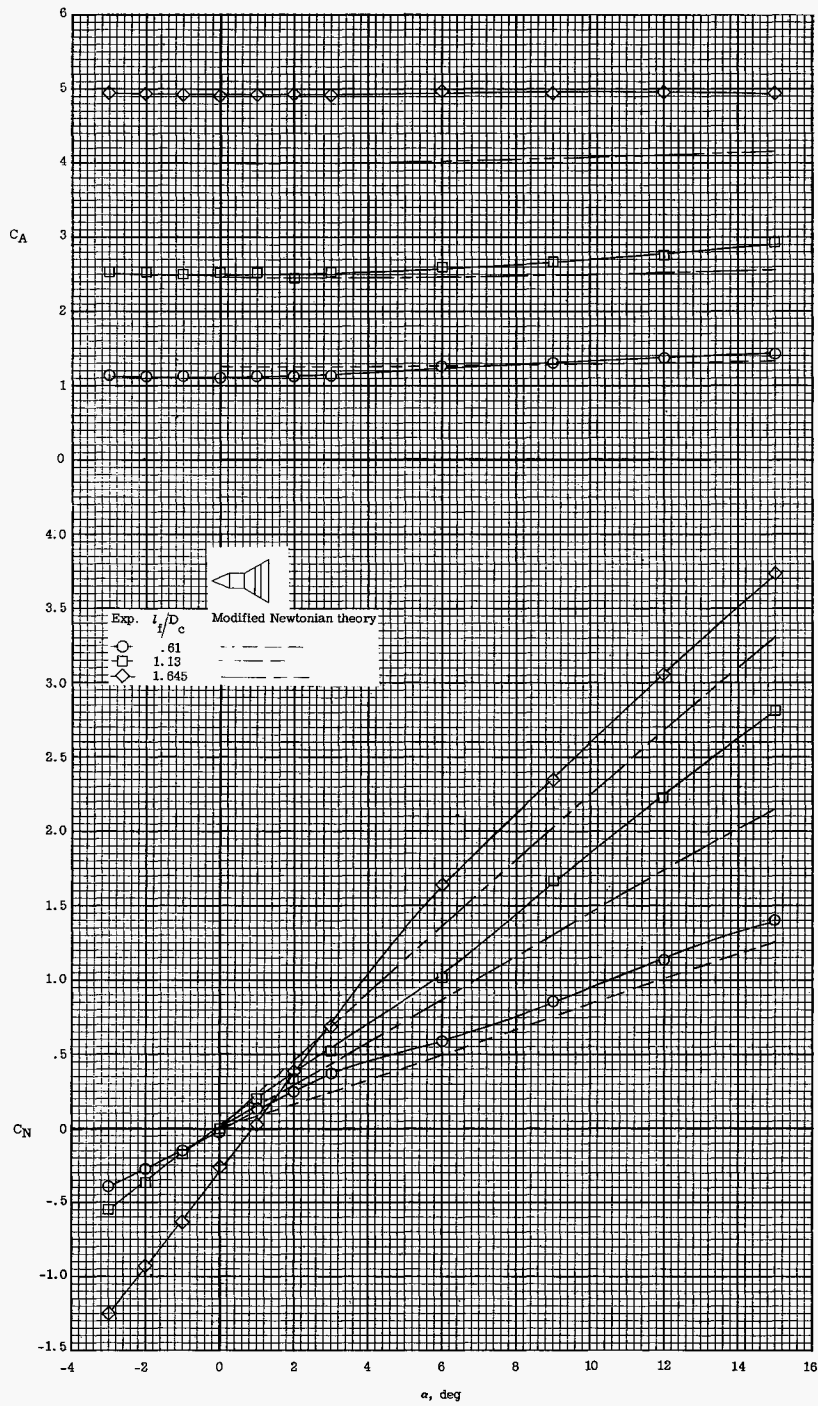
(b) Hemispherical nose, $l_c/D_c = 4.0$.

Figure 9.- Continued.



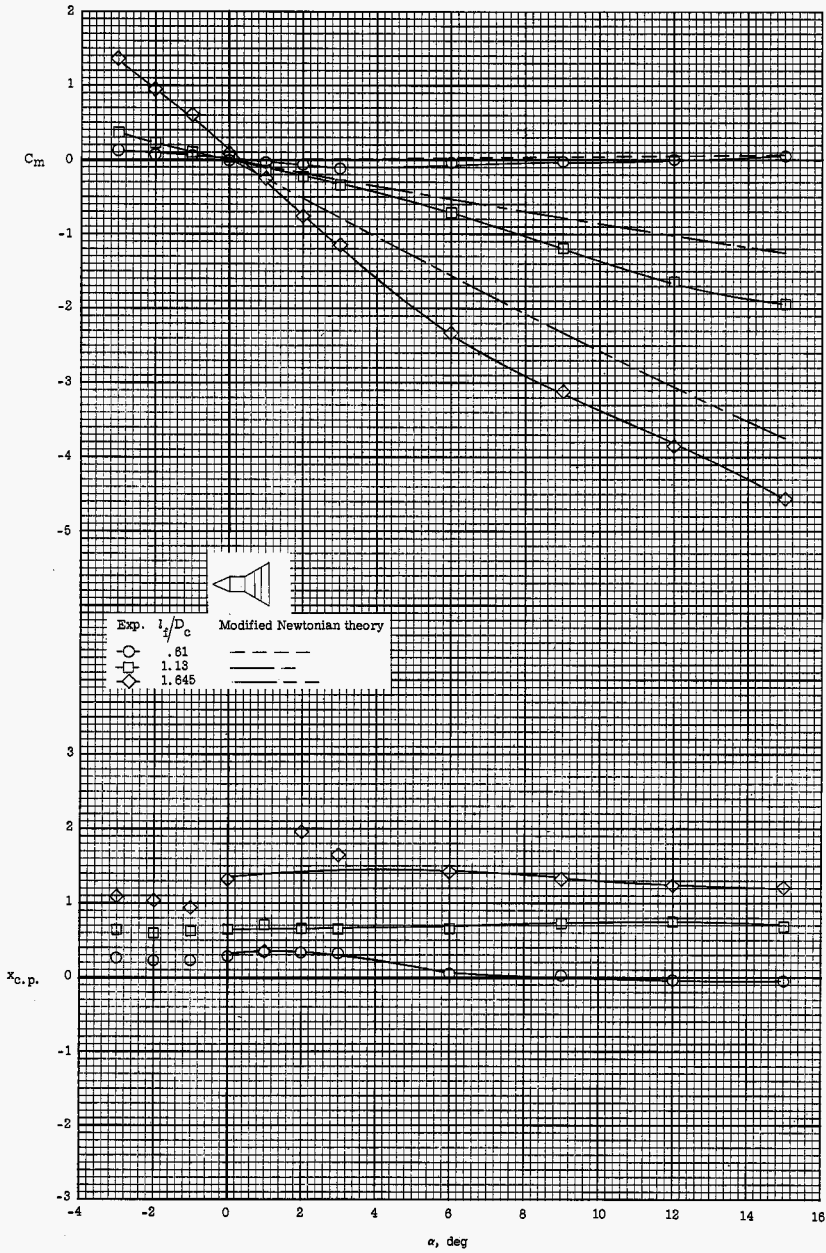
(b) Concluded.

Figure 9.- Continued.



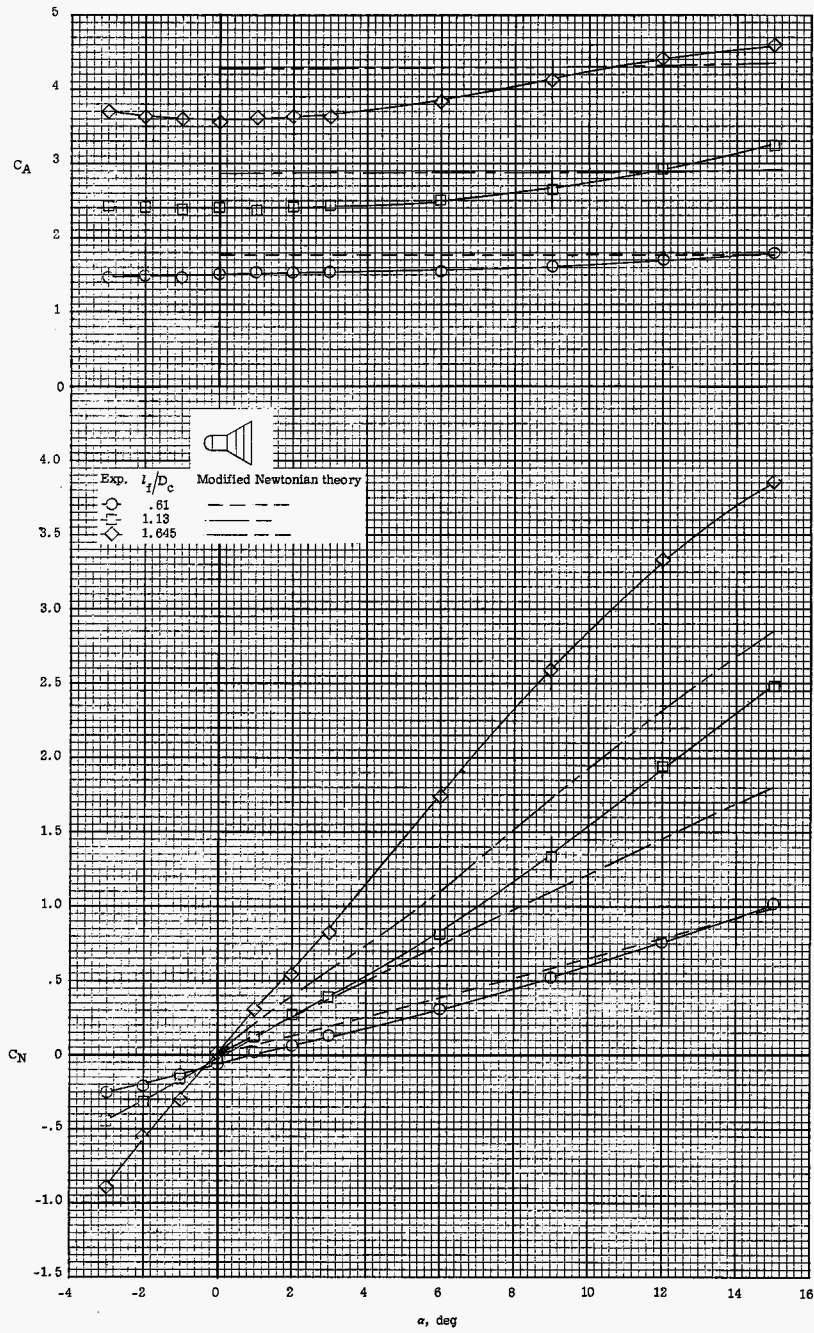
(c) Conical nose, $l_c/D_c = 1.0$.

Figure 9.- Continued.



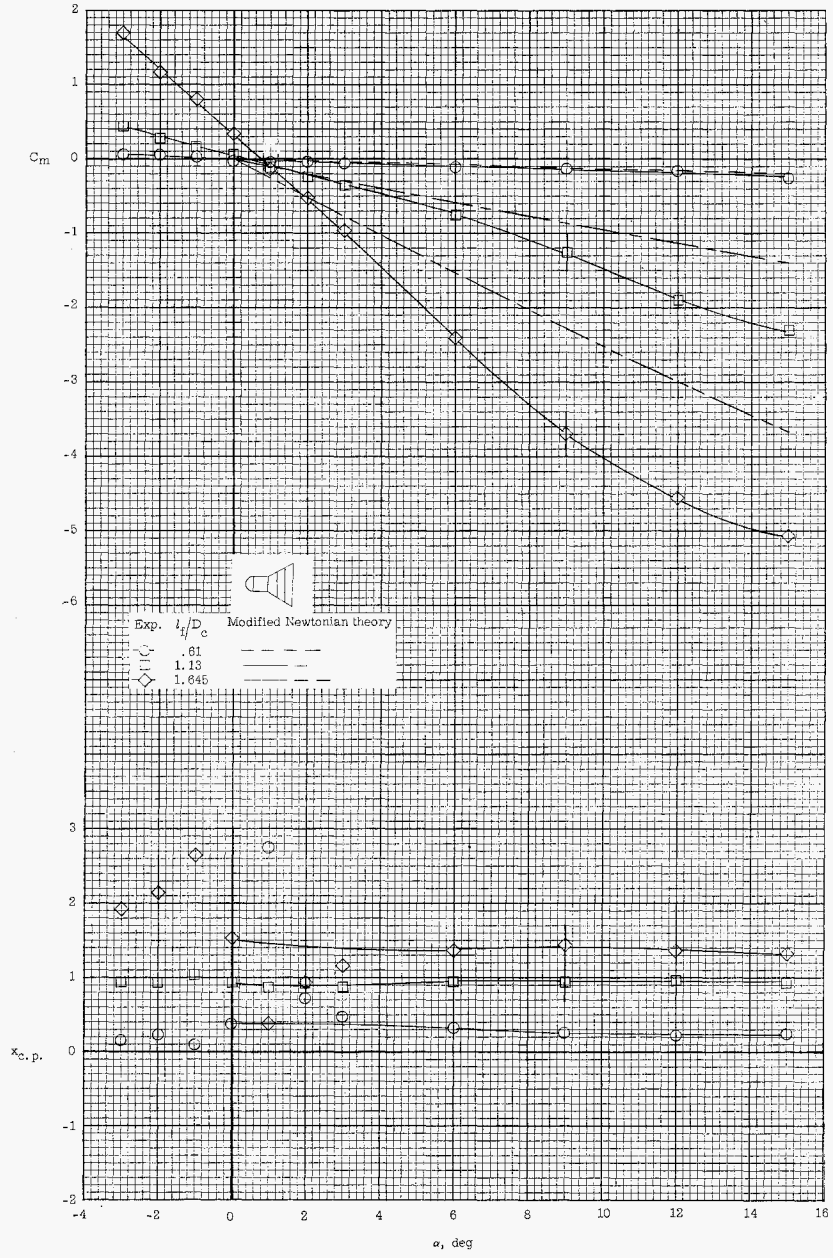
(c) Concluded.

Figure 9.- Continued.



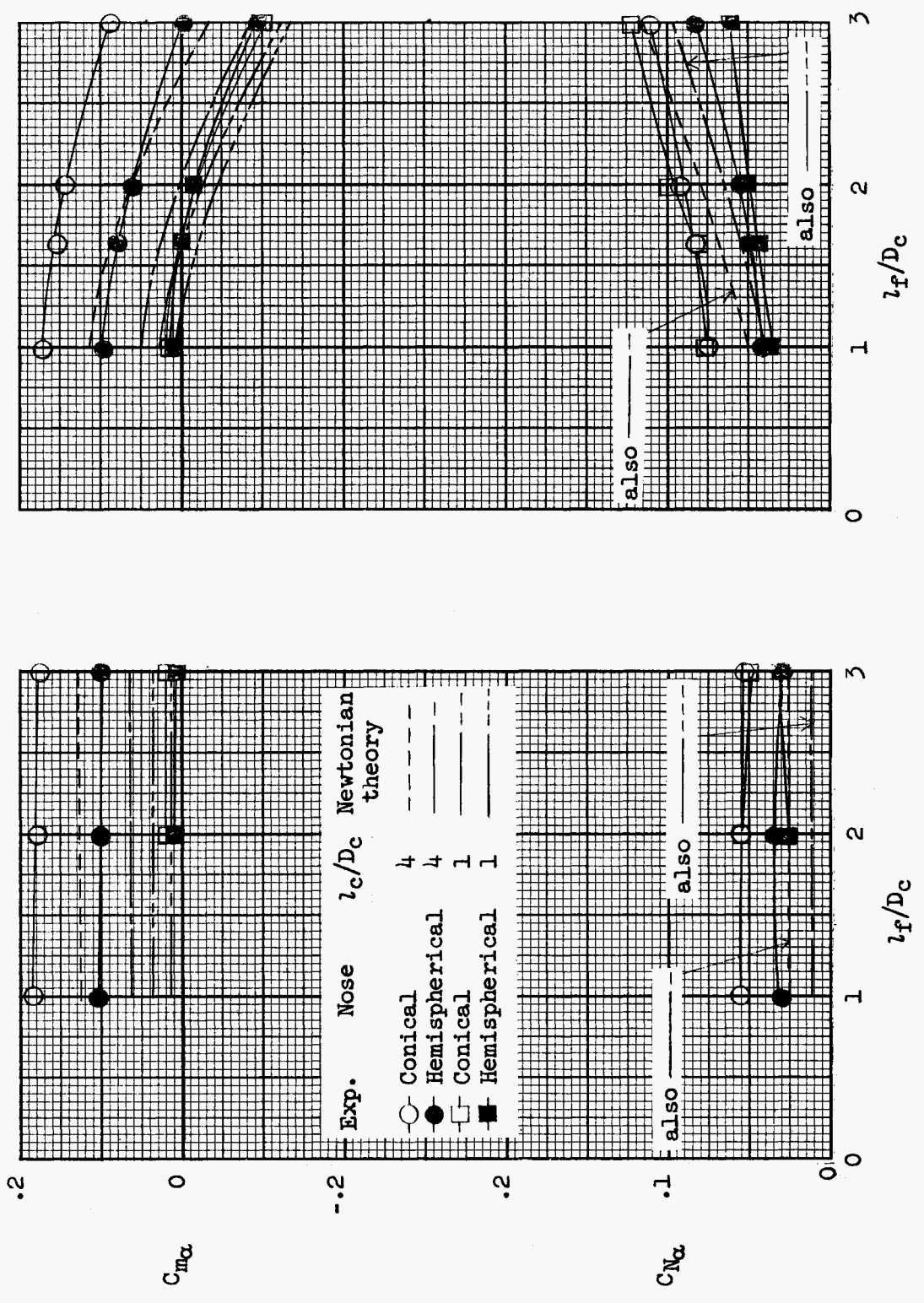
(d) Hemispherical nose, $l_c/D_c = 1.0$.

Figure 9.- Continued.



(d) Concluded.

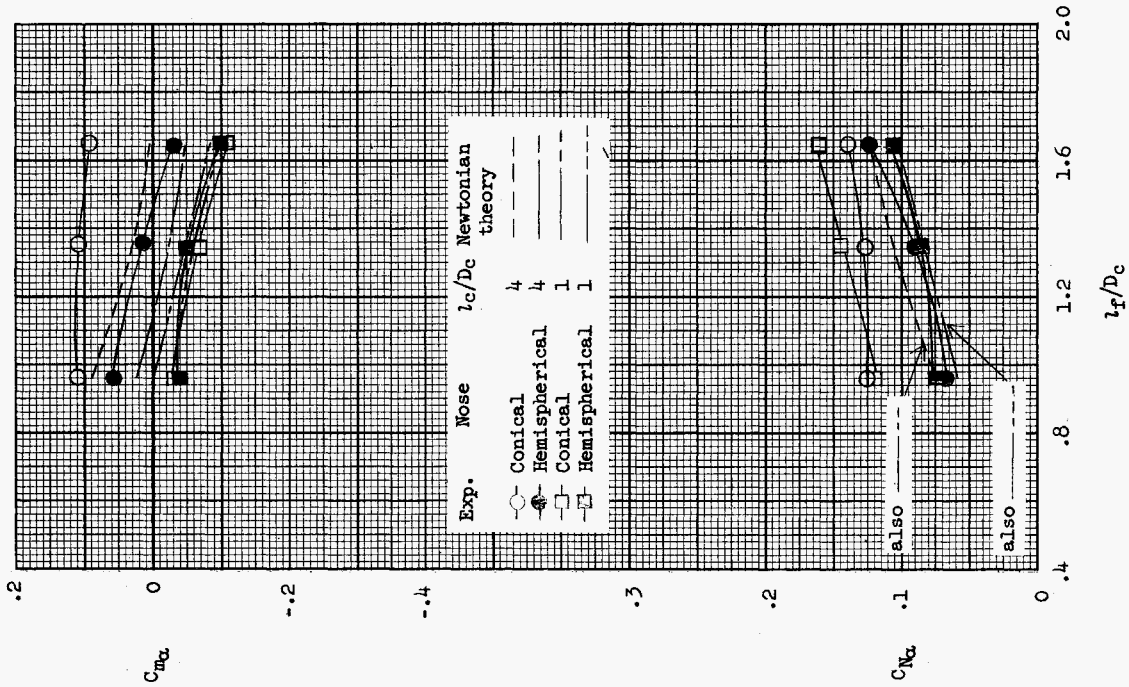
Figure 9.- Concluded.



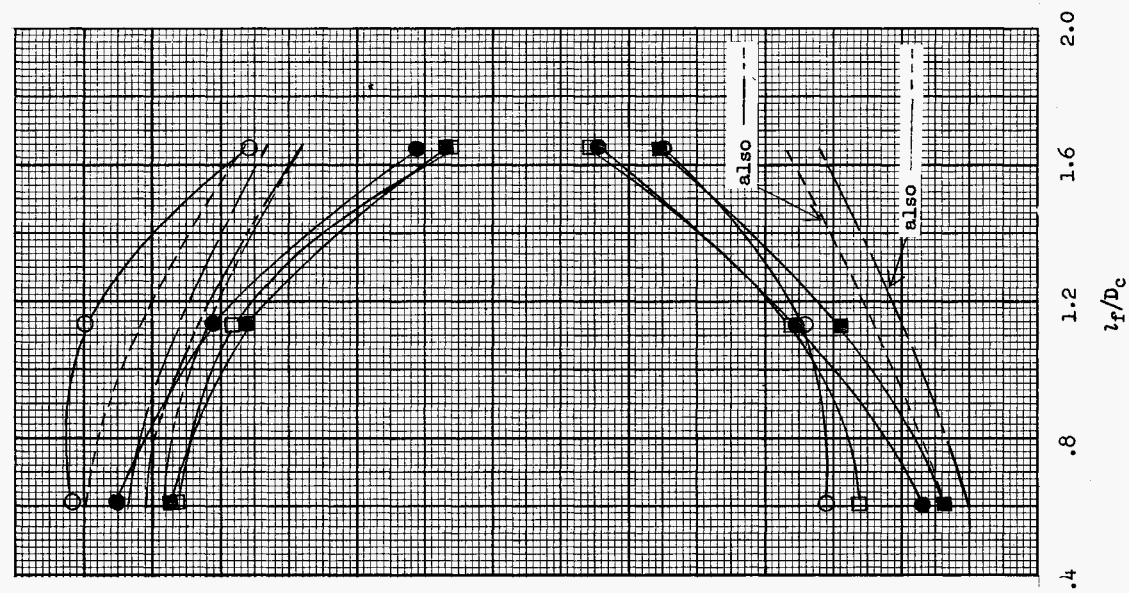
(a) $\theta_f = 0^\circ$.

(b) $\theta_f = 10^\circ$.

Figure 10.- Variation of normal-force-curve and pitching-moment-curve slopes at zero angle of attack with flare length for various flare angles.

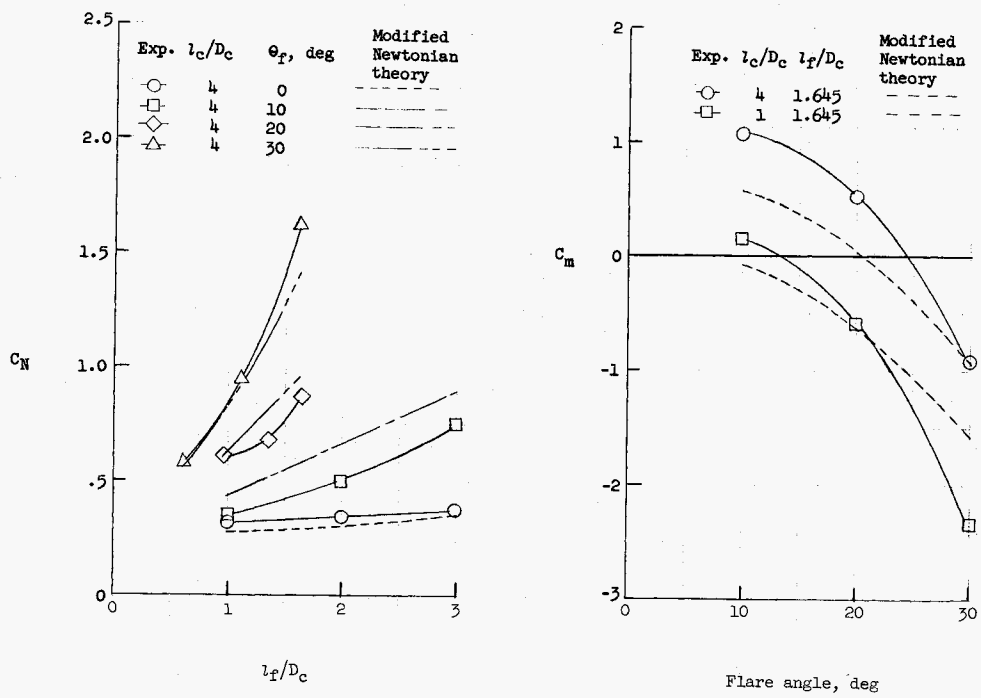


(c) $\theta_F = 20^\circ$.

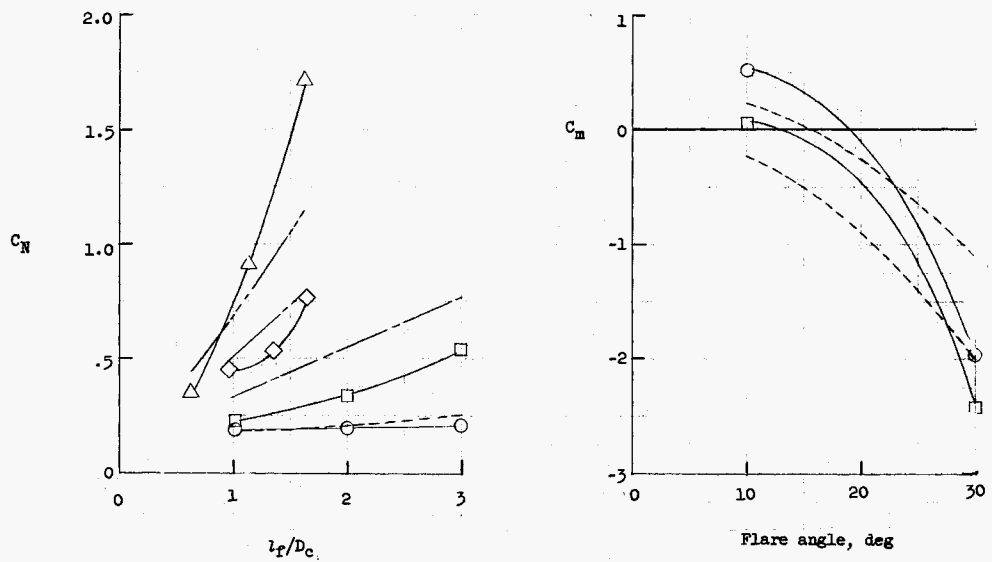


(d) $\theta_F = 30^\circ$.

Figure 10.- Concluded.

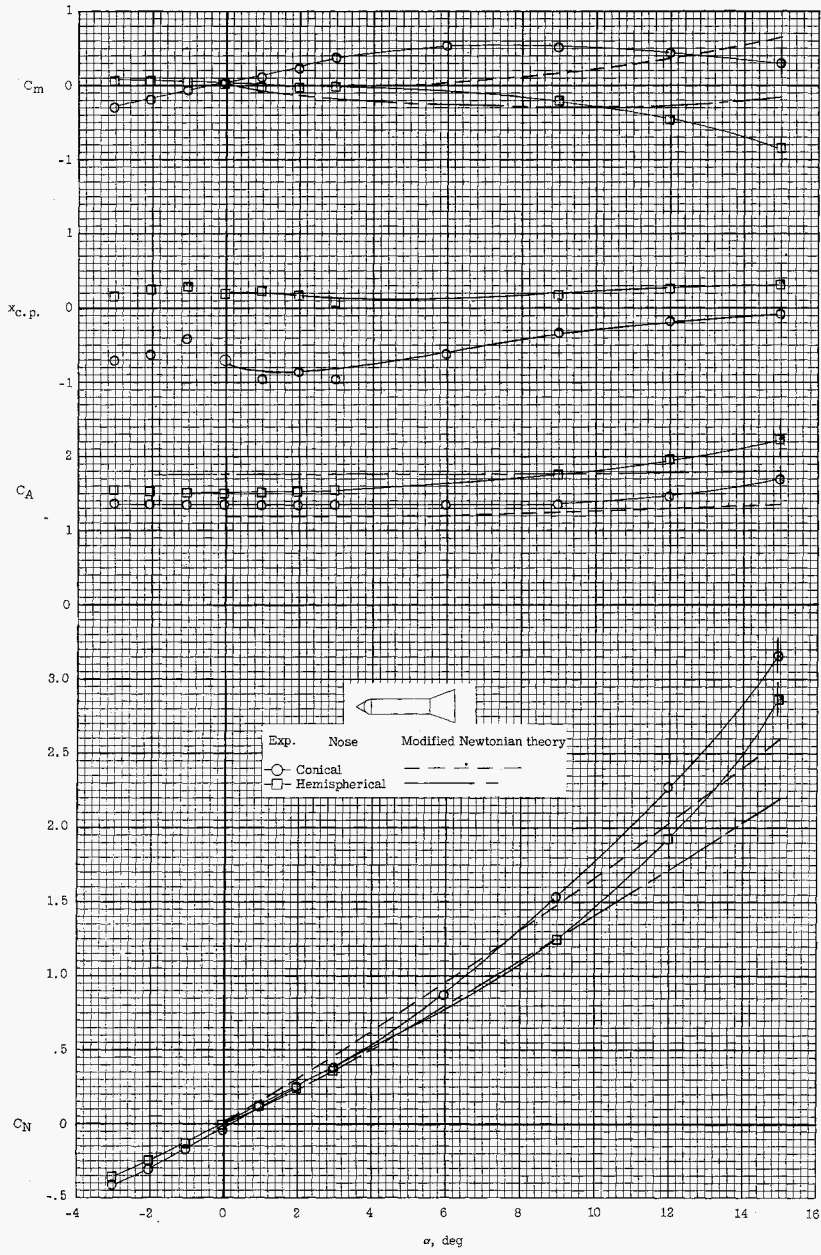


(a) Conical nose.



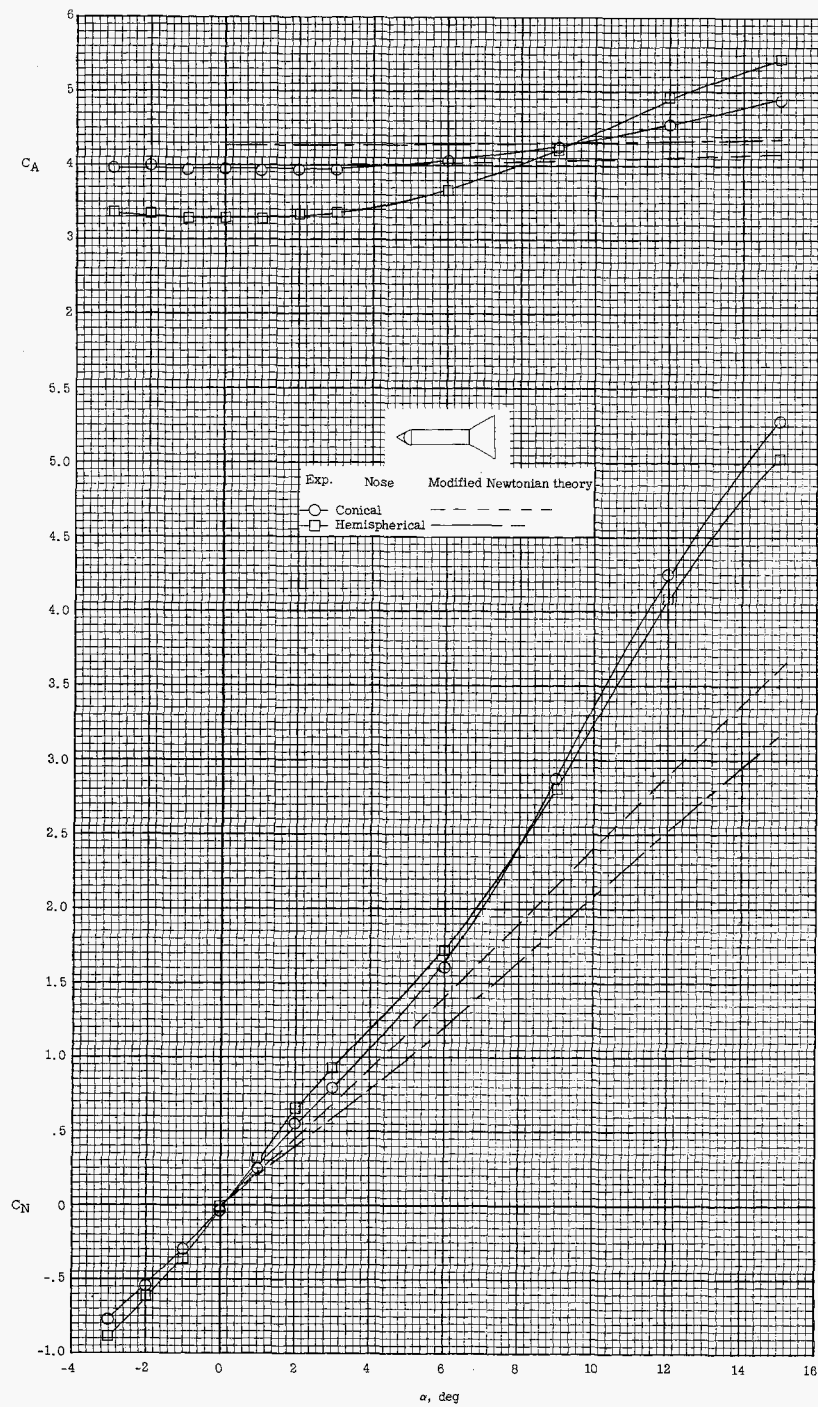
(b) Hemispherical nose.

Figure 11.- Typical measured and predicted results showing effect of flare length, flare angle, cylinder length, and nose bluntness on aerodynamic coefficients. $\alpha = 6.0^\circ$.



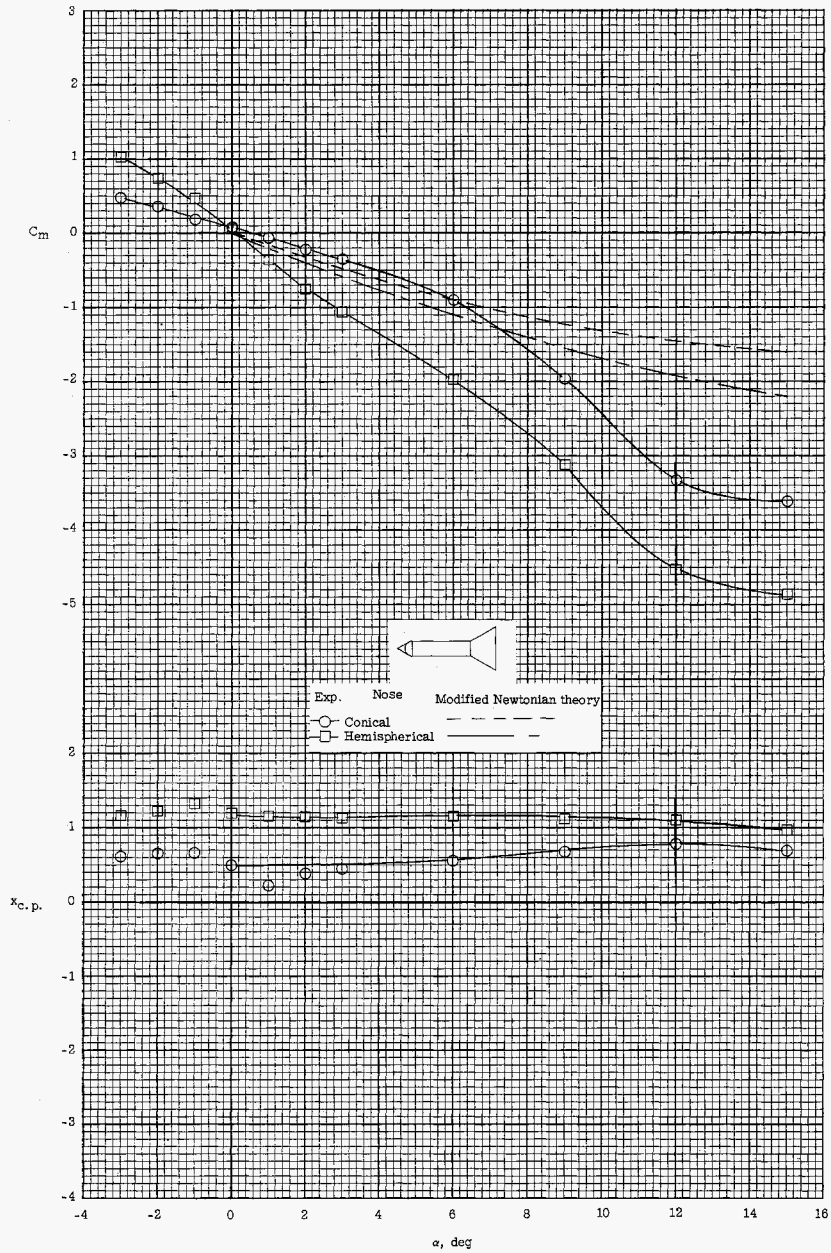
(a) $\theta_f = 20^\circ$.

Figure 12.- Effect of nose bluntness on longitudinal characteristics of $l_c/D_c = 4.0$, $l_f/D_c = 1.645$ configuration.



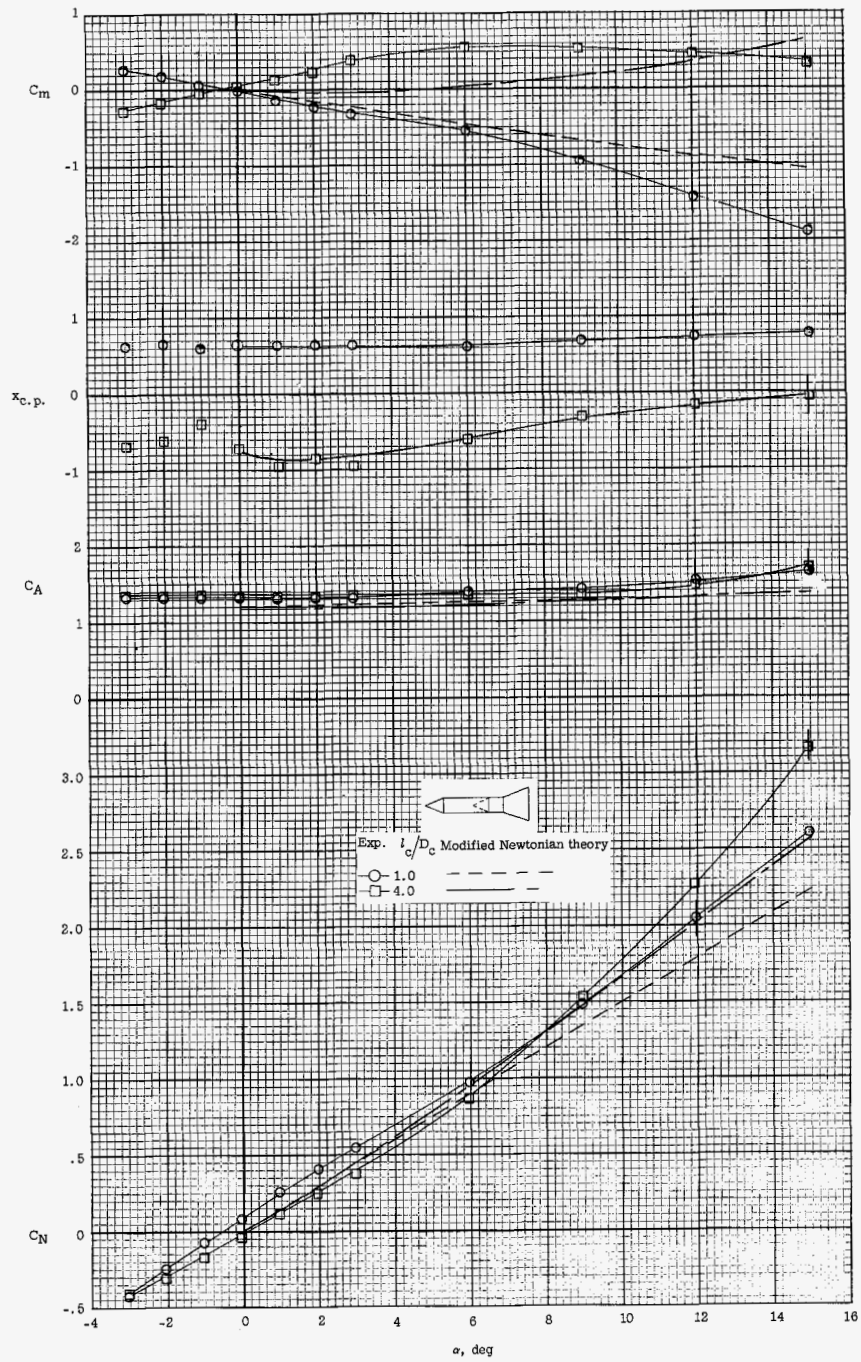
(b) $\theta_f = 30^\circ$.

Figure 12.- Continued.



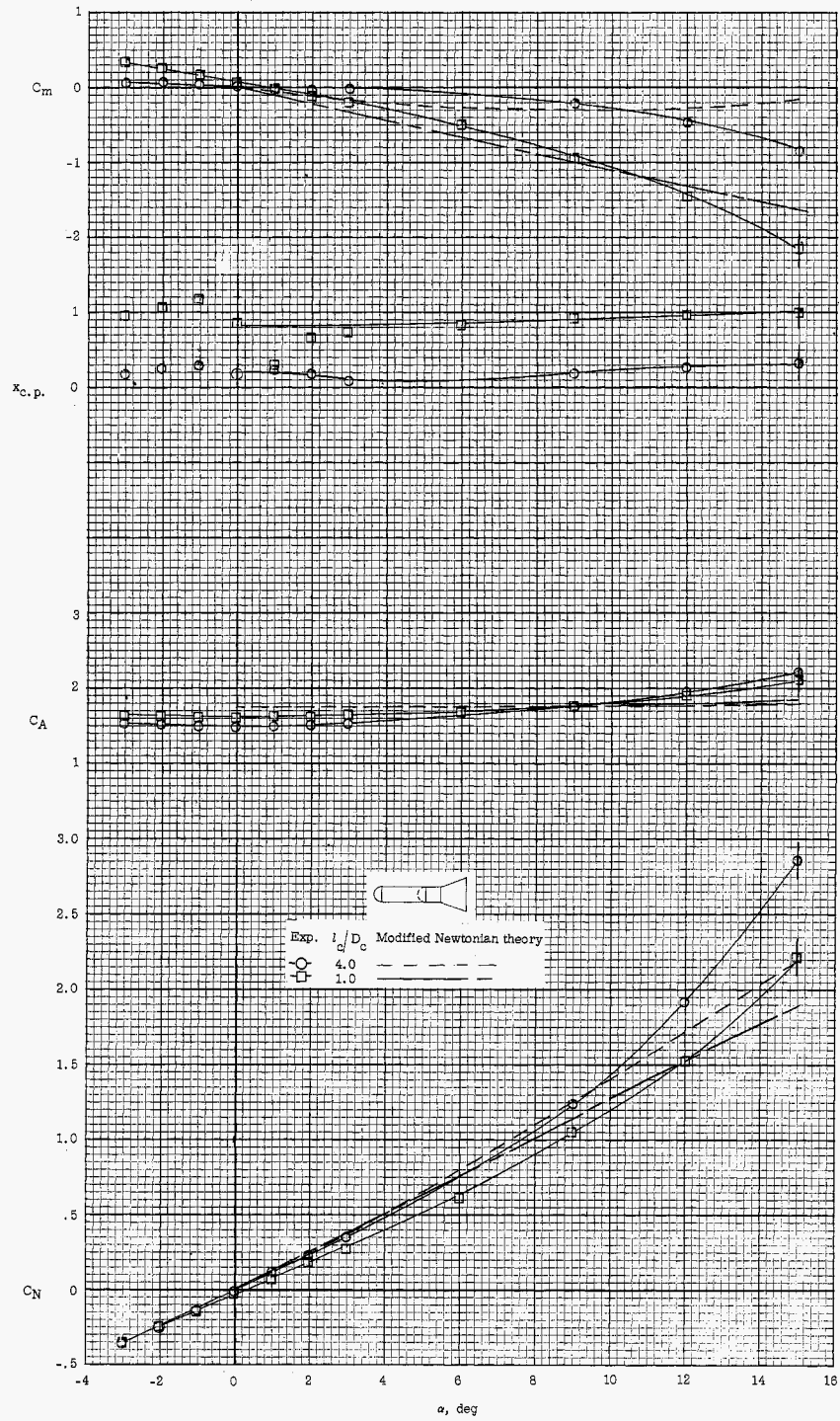
(b) Concluded.

Figure 12.- Concluded.



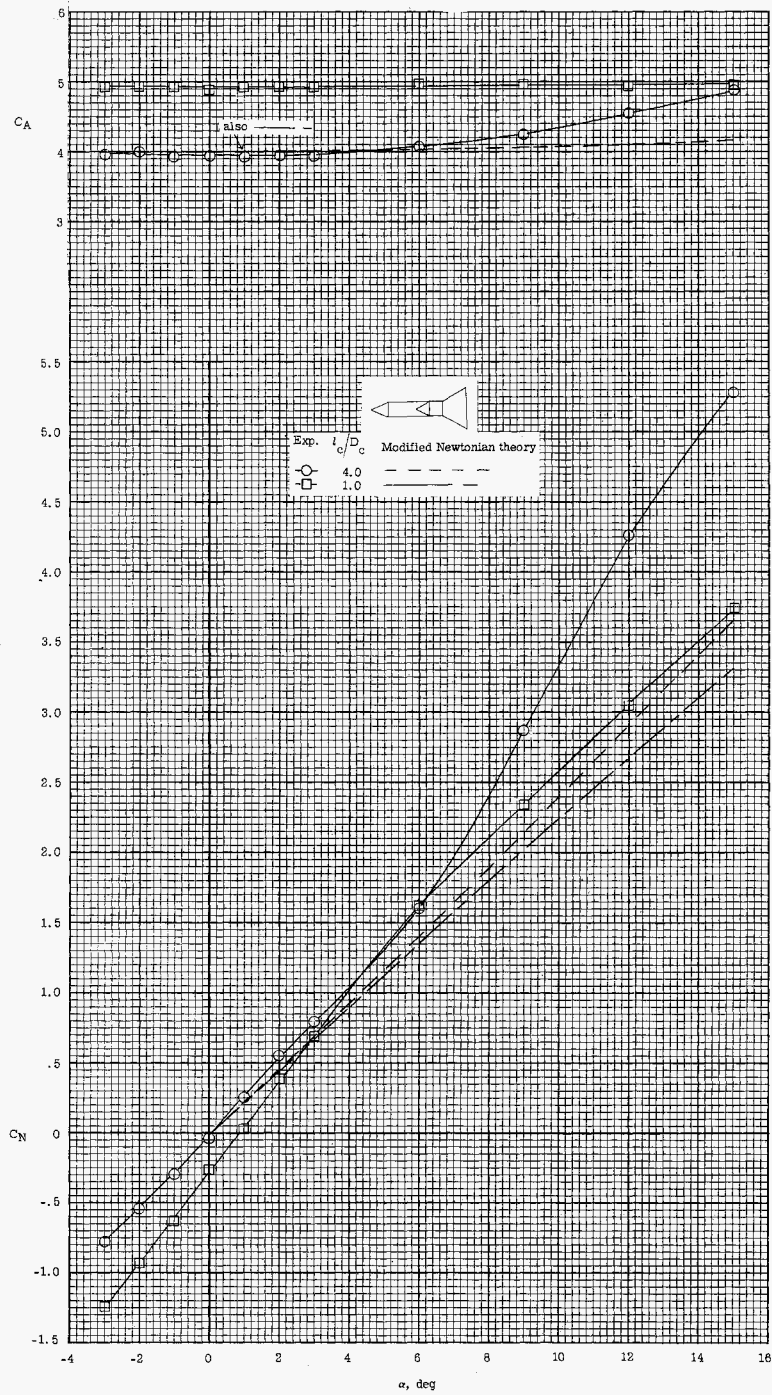
(a) Conical nose.

Figure 13.- Effect of cylinder length and bluntness on longitudinal aerodynamic characteristics of $l_f/D_c = 1.645$, $\theta_f = 20^\circ$ flare.



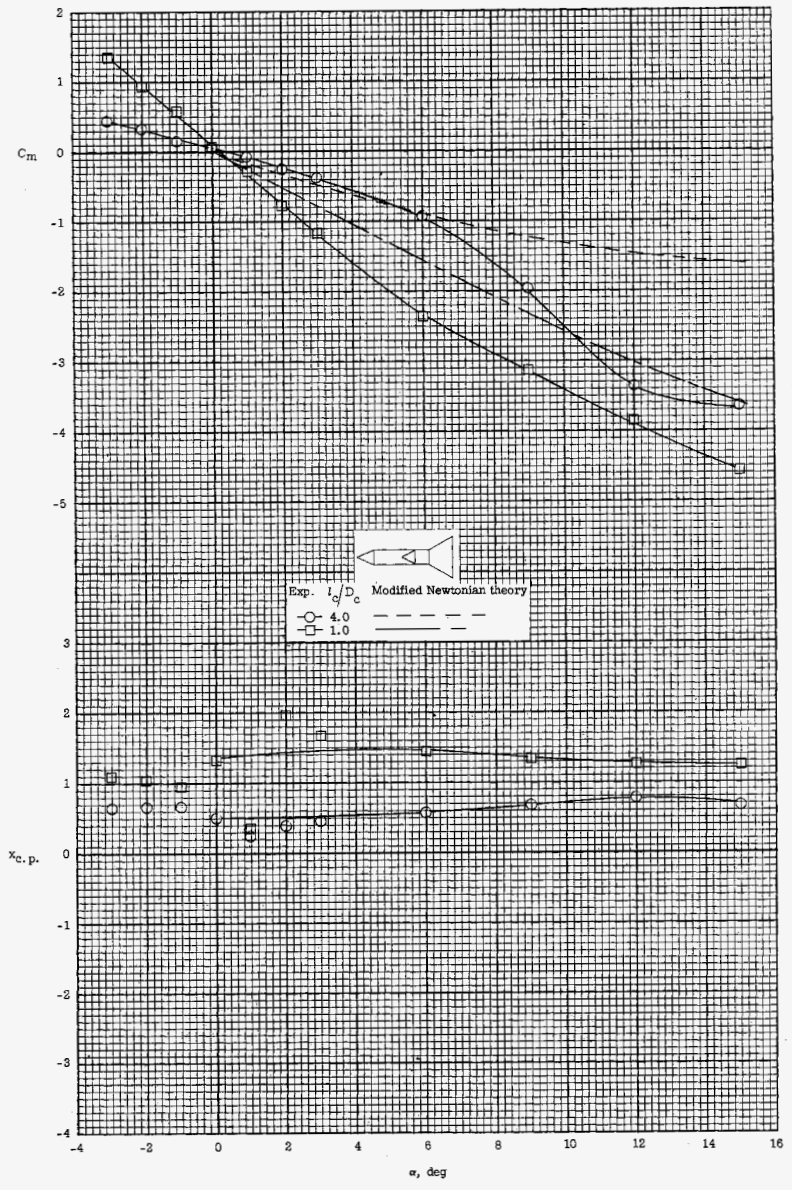
(b) Hemispherical nose.

Figure 13.- Concluded.



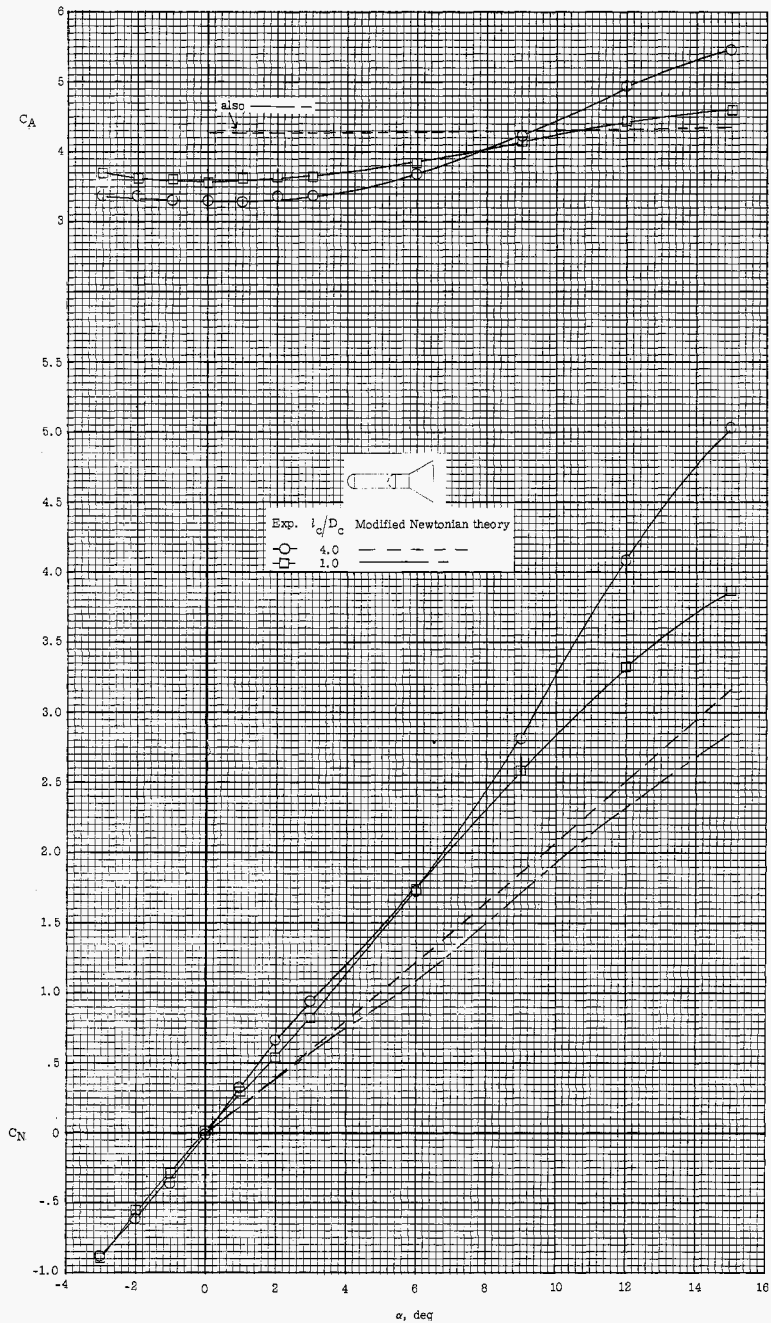
(a) Conical nose.

Figure 14.- Effect of cylinder length on longitudinal aerodynamic characteristics of $l_f/D_c = 1.645$, $\theta_f = 30^\circ$ flare.



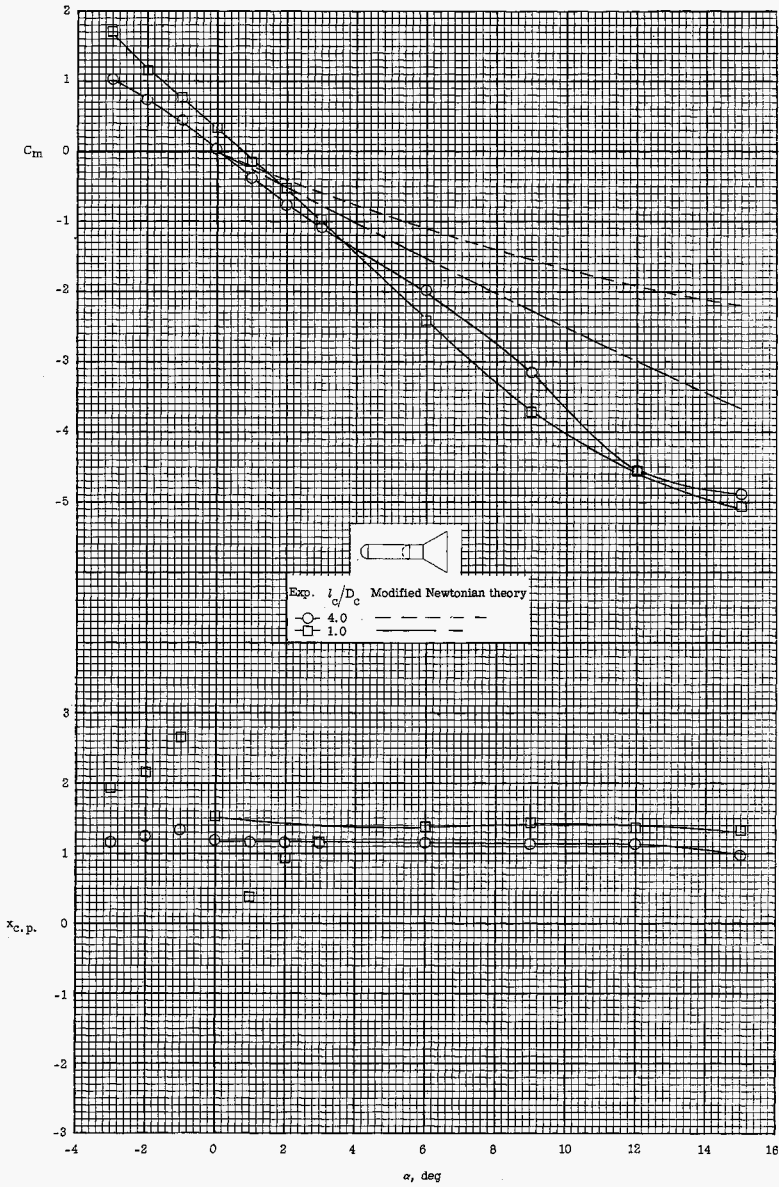
(a) Concluded.

Figure 14.- Continued.



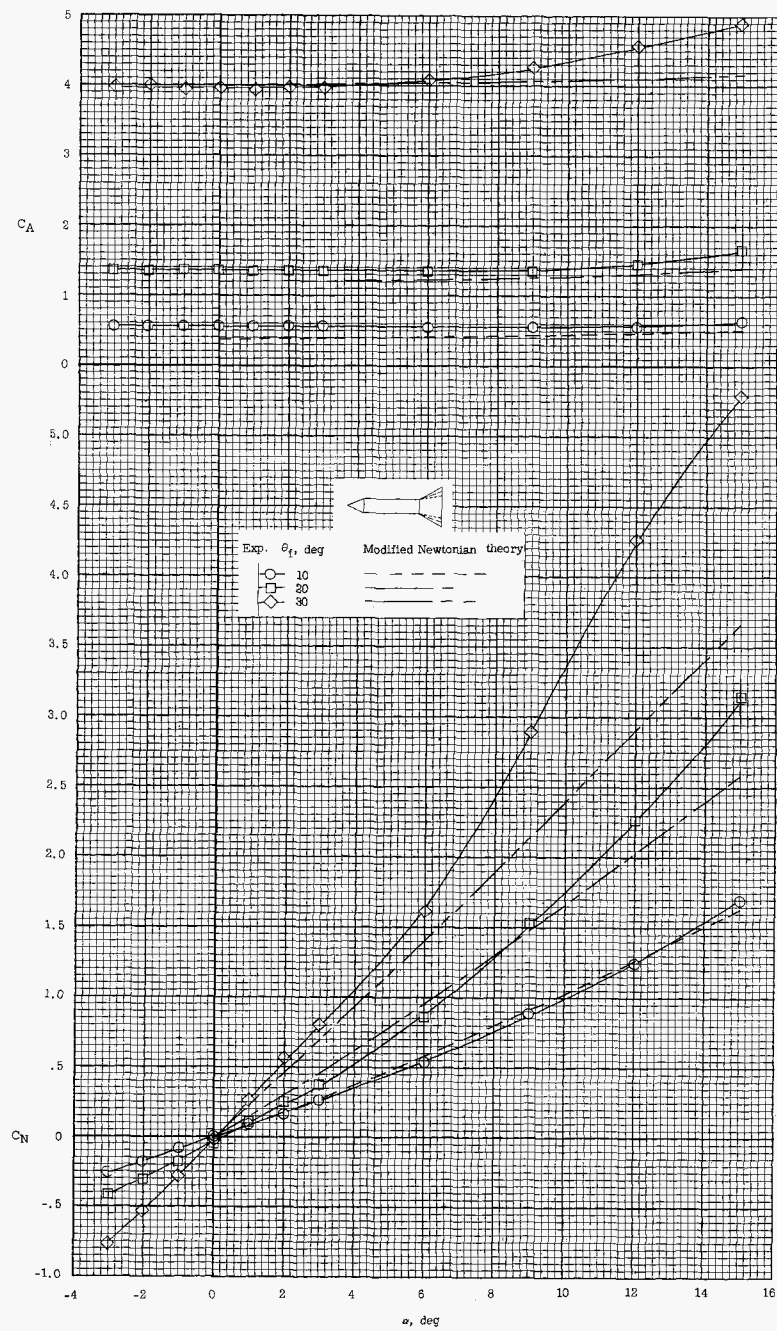
(b) Hemispherical nose.

Figure 14.- Continued.



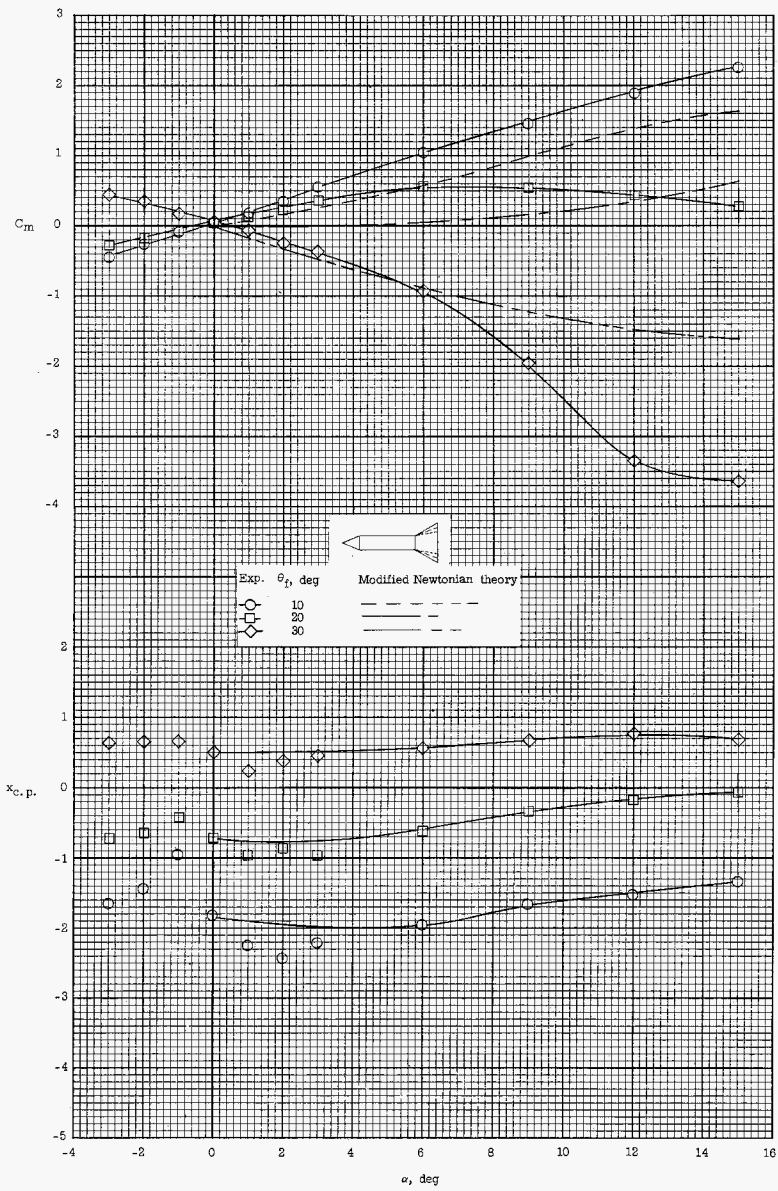
(b) Concluded.

Figure 14.- Concluded.



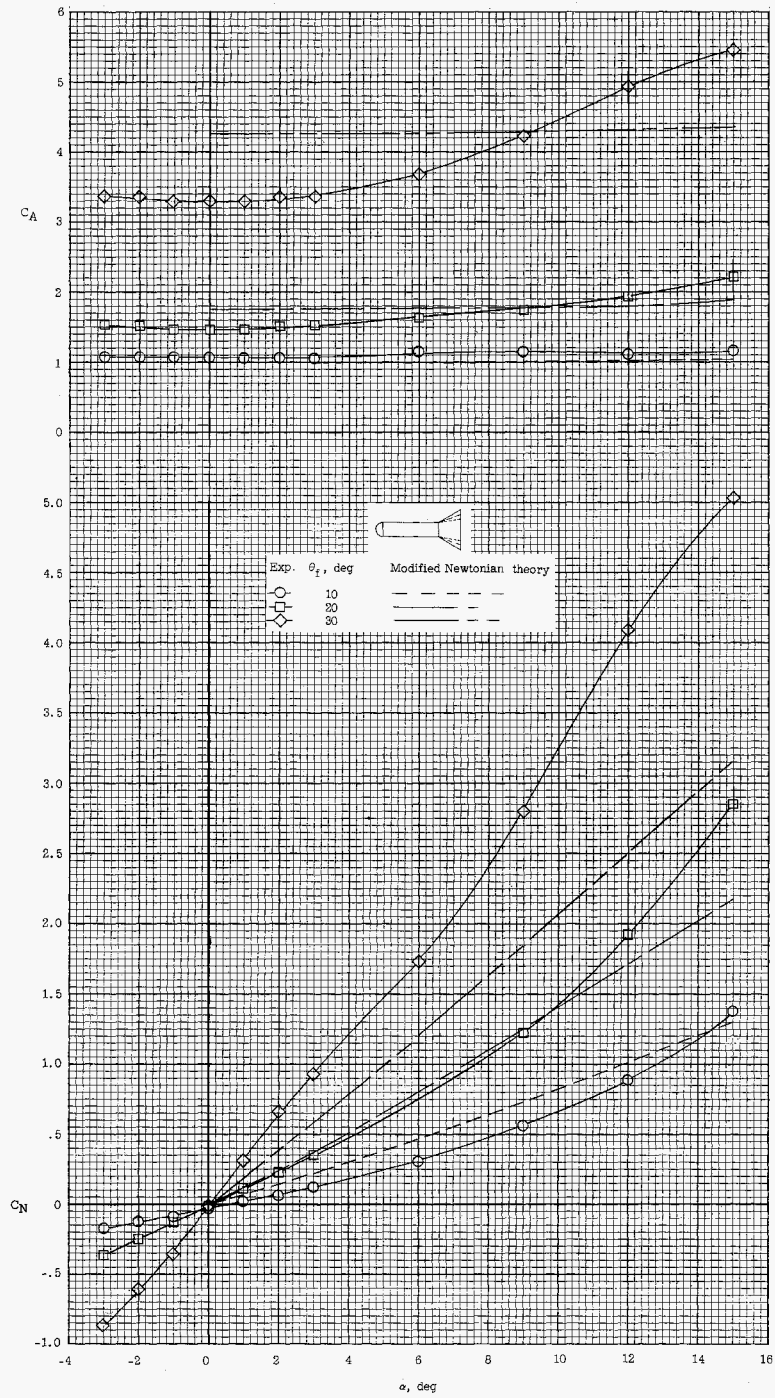
(a) Conical nose, $l_c/D_c = 4.0$.

Figure 15.- Effect of flare angle on longitudinal aerodynamic characteristics of various configurations for a constant flare length, $l_f/D_c = 1.645$.



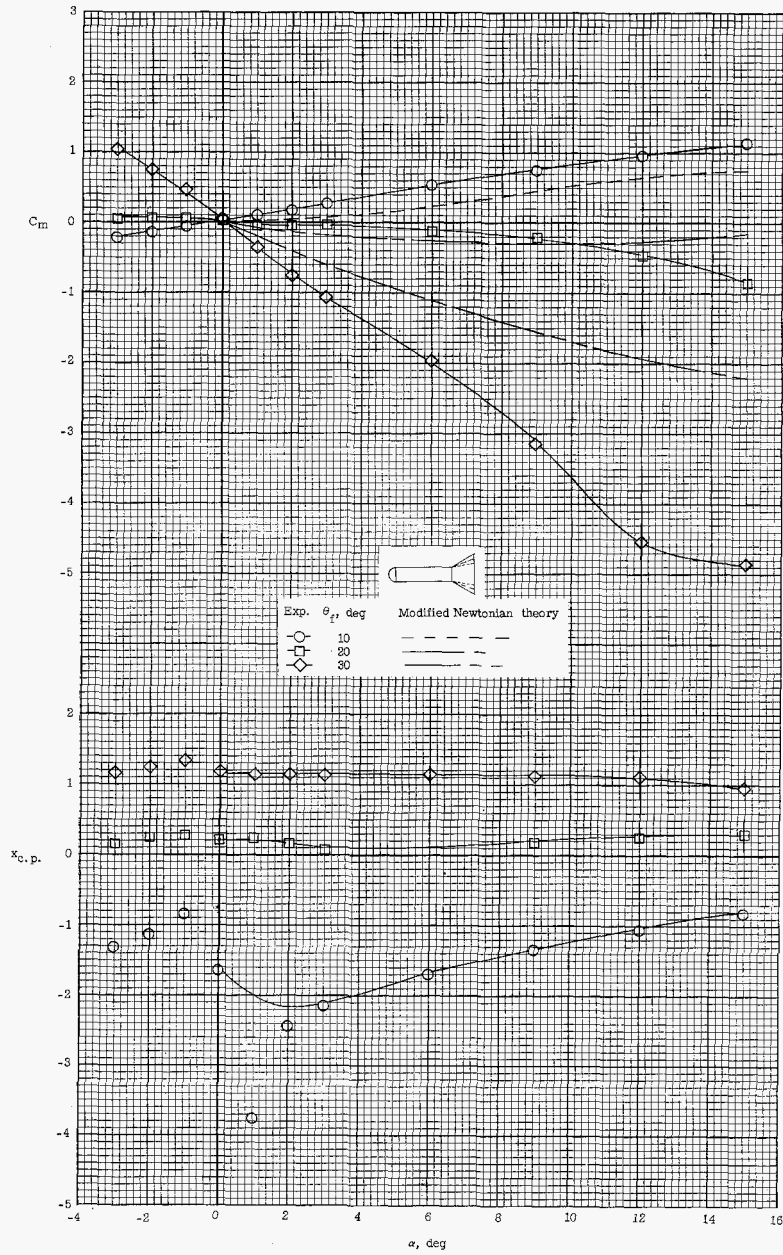
(a) Concluded.

Figure 15.- Continued.



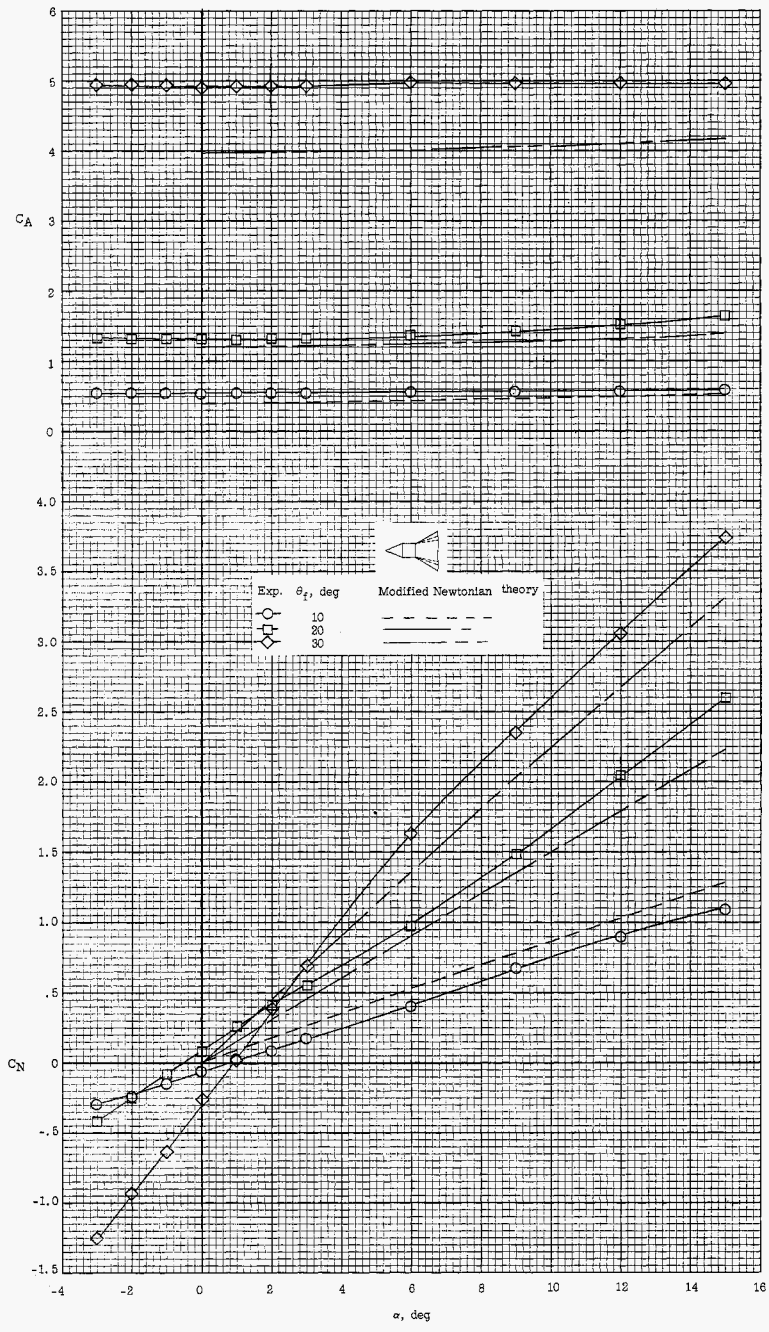
(b) Hemispherical nose, $l_c/D_c = 4.0$.

Figure 15.- Continued.



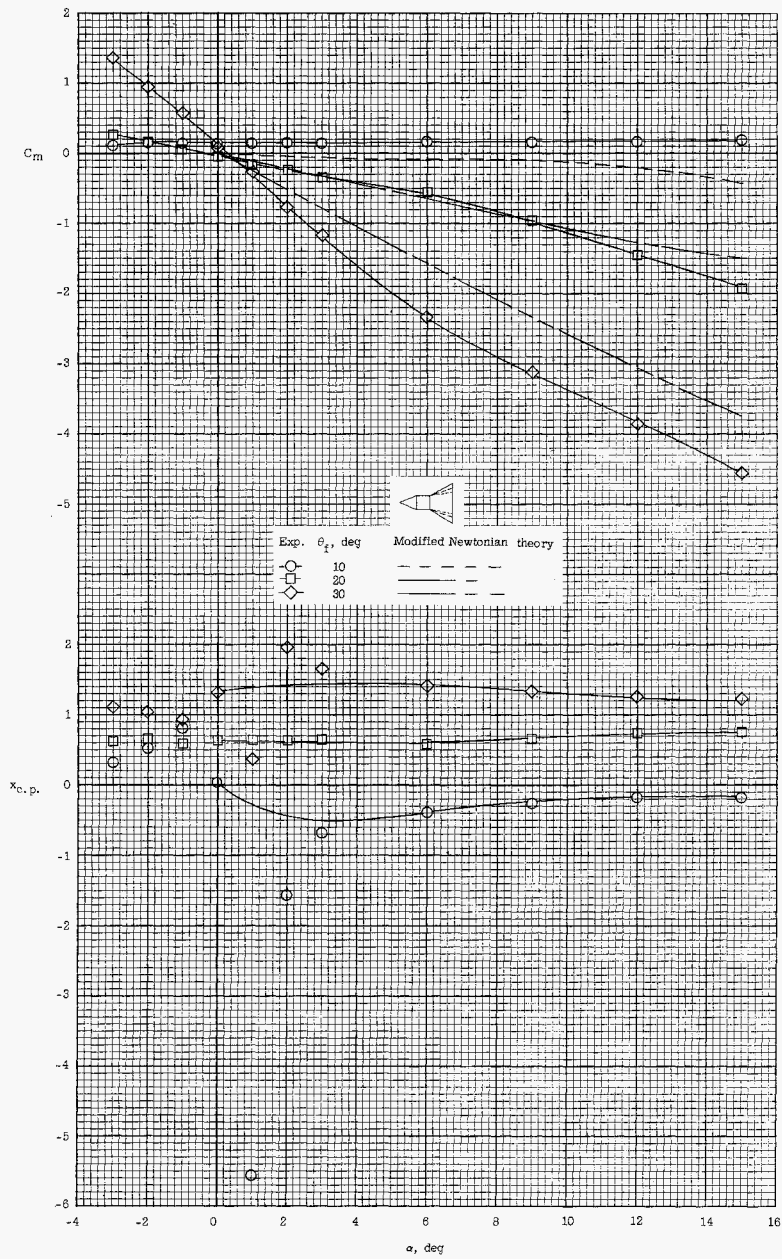
(b) Concluded.

Figure 15.- Continued.



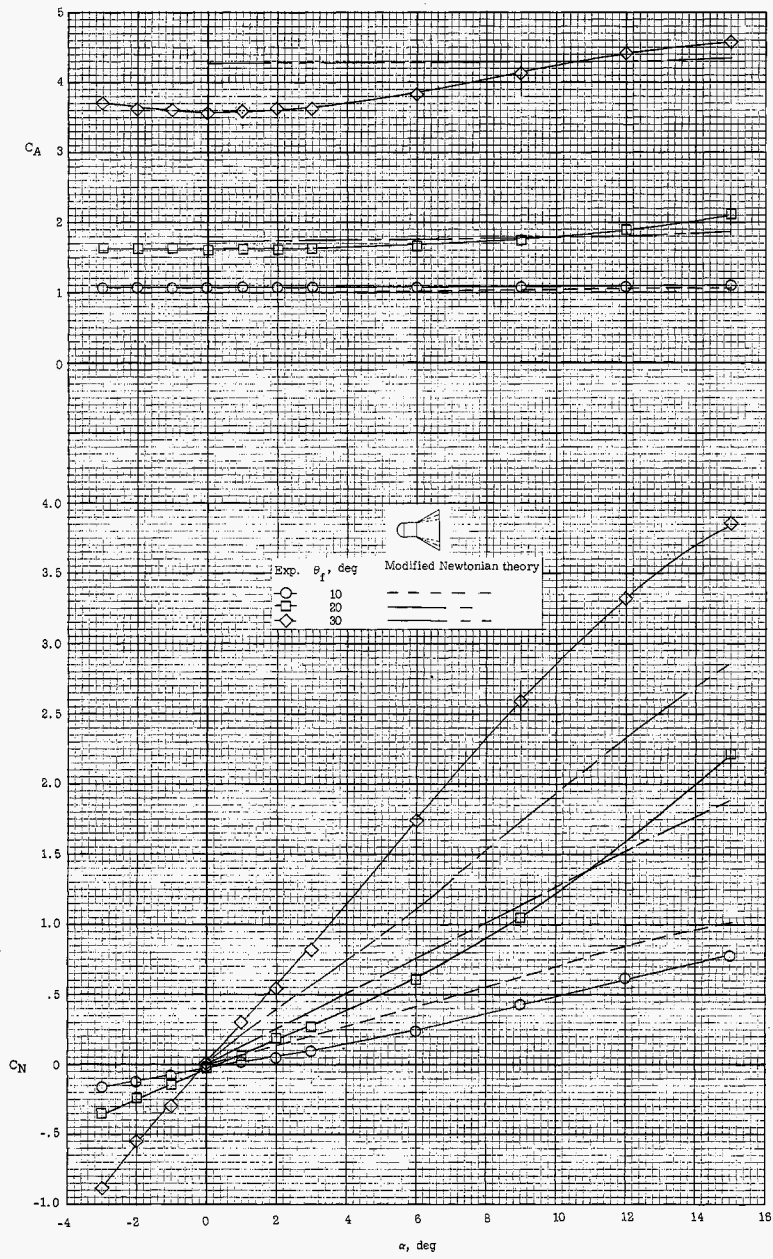
(c) Conical nose, $\lambda_c/D_c = 1.0$.

Figure 15.- Continued.



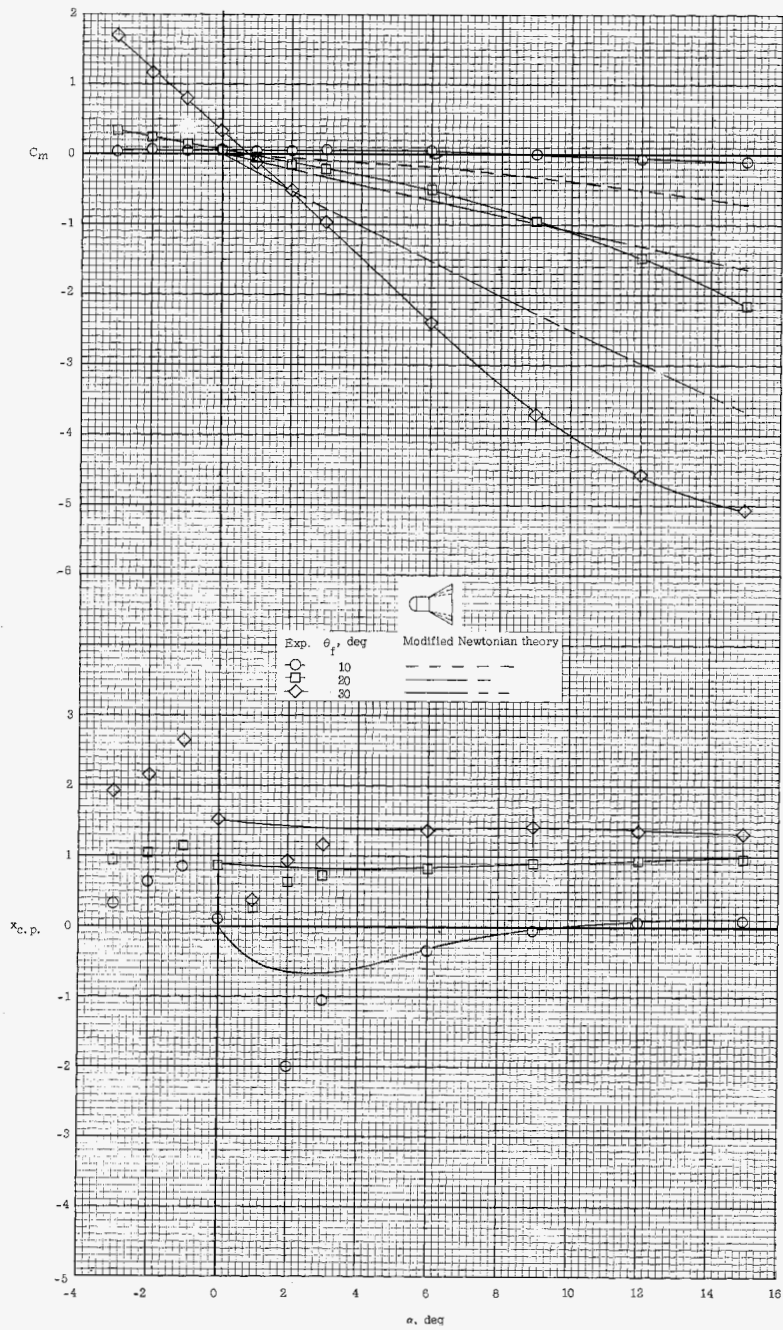
(c) Concluded.

Figure 15.- Continued.



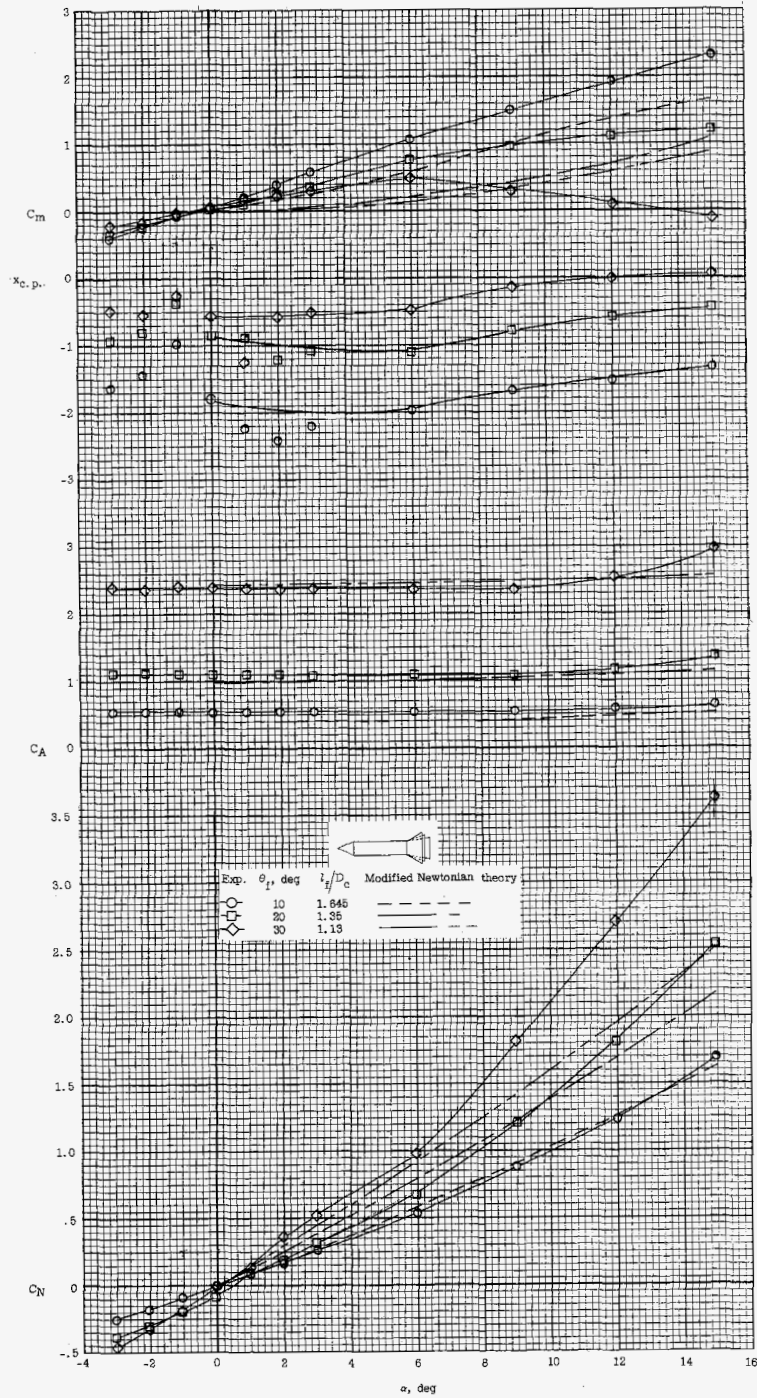
(d) Hemispherical nose, $l_c/D_c = 1.0$.

Figure 15.- Continued.



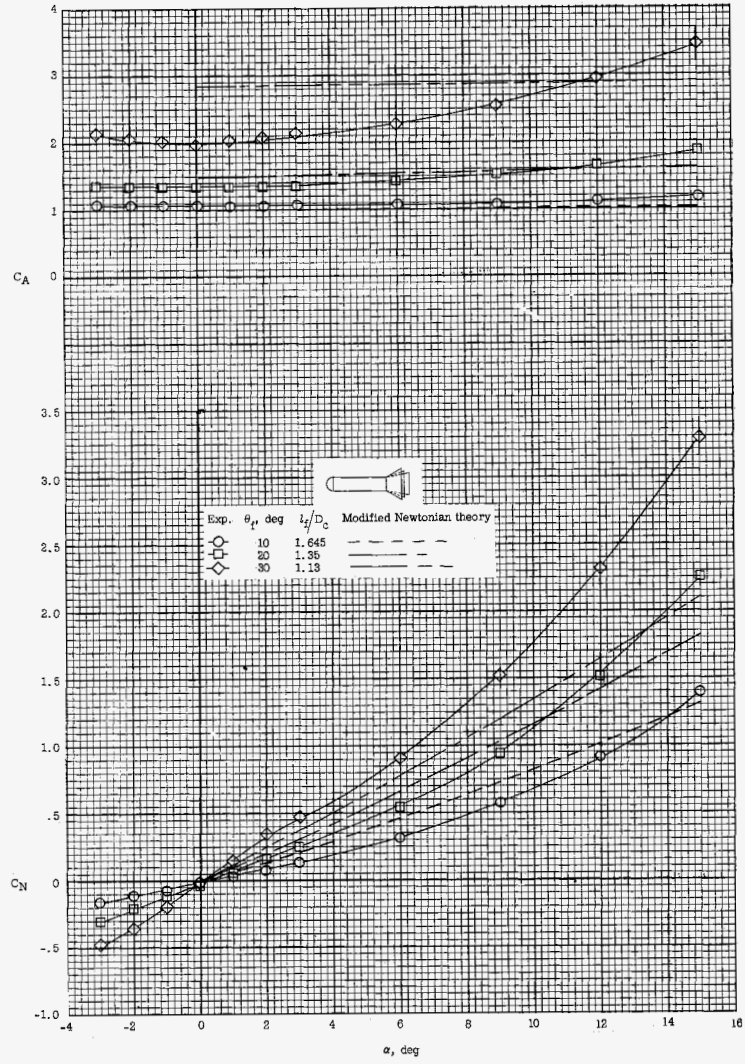
(d) Concluded.

Figure 15.- Concluded.



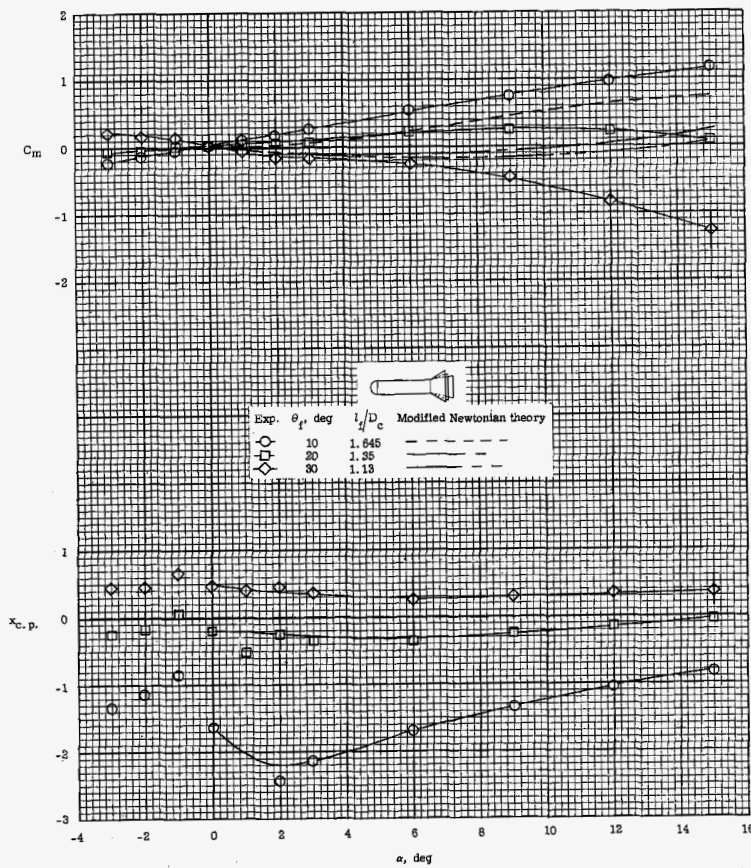
(a) Conical nose, $l_c/D_c = 4.0$.

Figure 16.- Effect of flare angle on the longitudinal aerodynamic characteristics of various configurations for a constant surface area, $S_f/A = 8.62$.



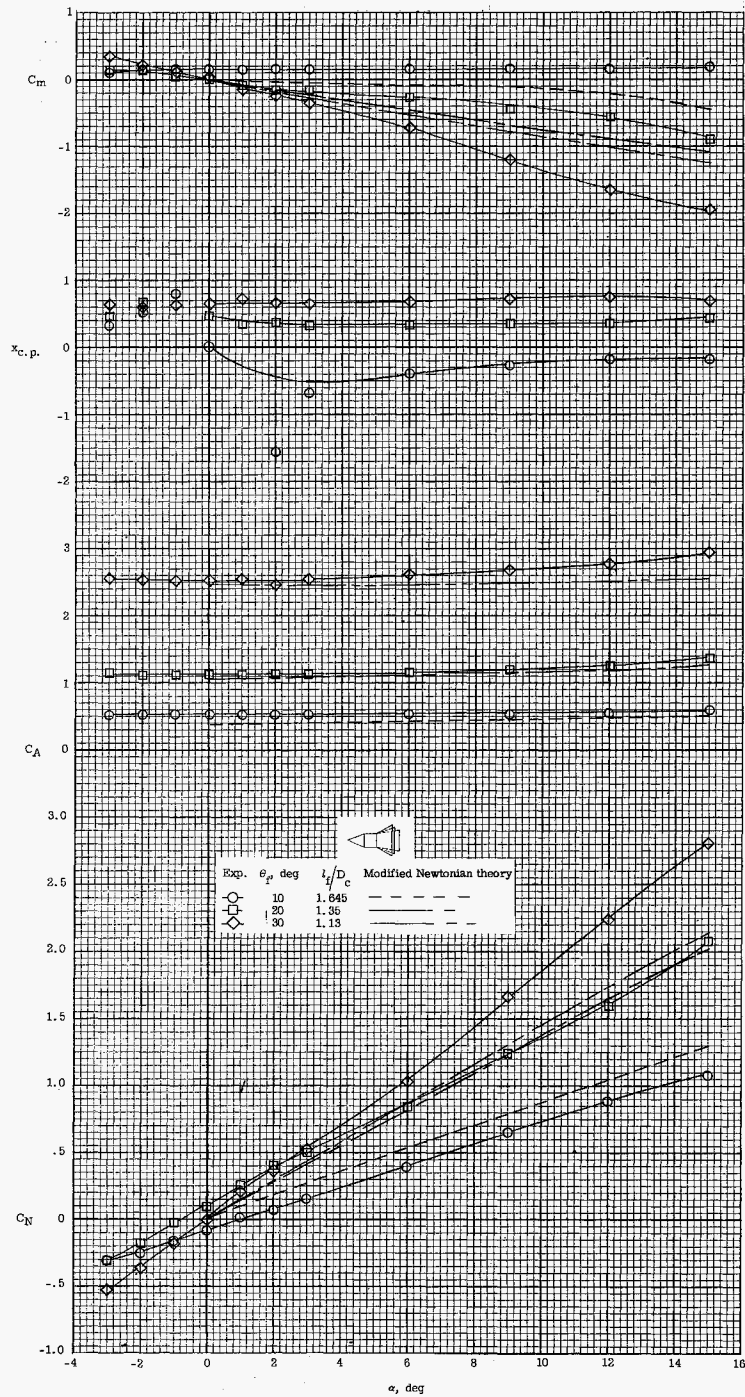
(b) Hemispherical nose, $l_c/D_c = 4.0$.

Figure 16.- Continued.



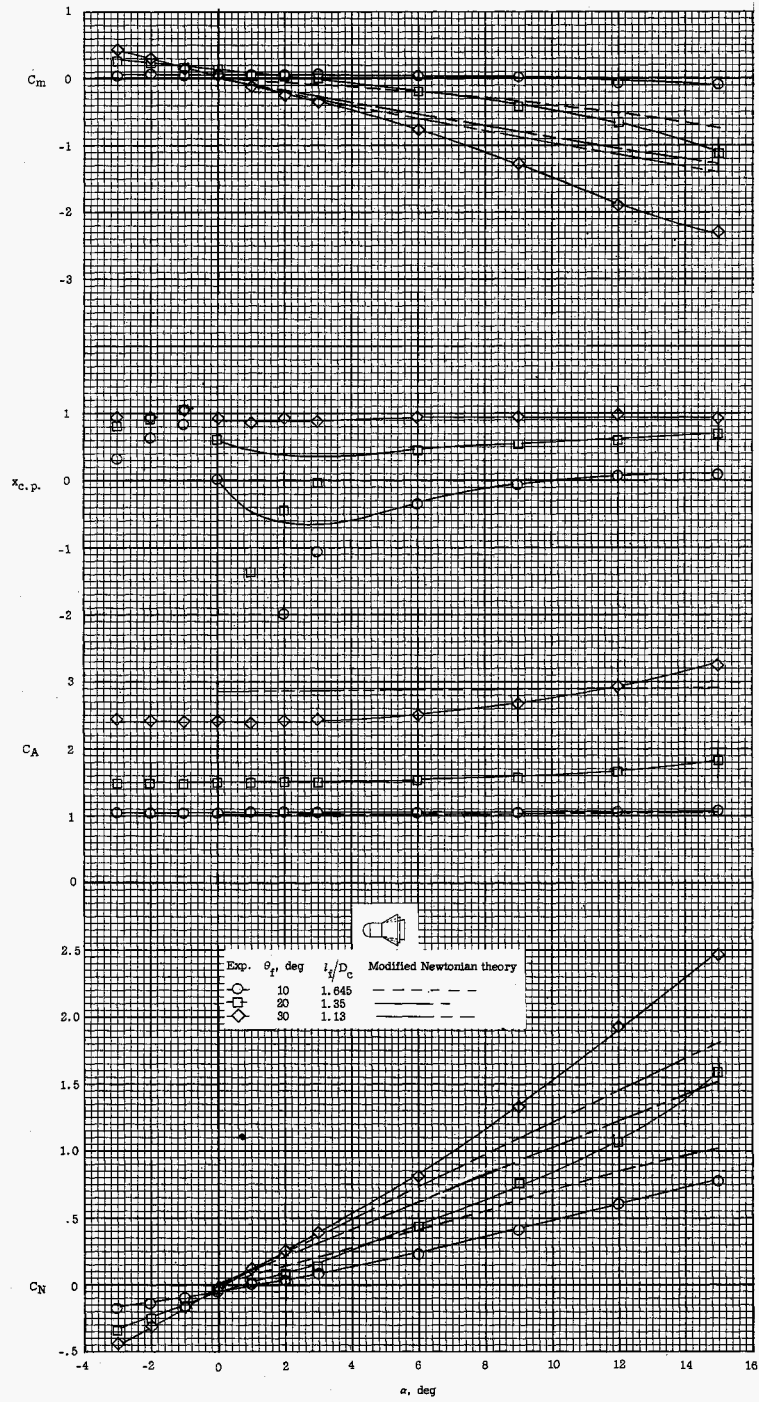
(b) Concluded.

Figure 16.- Continued.



(c) Conical nose, $l_c/D_c = 1.0$.

Figure 16.- Continued.

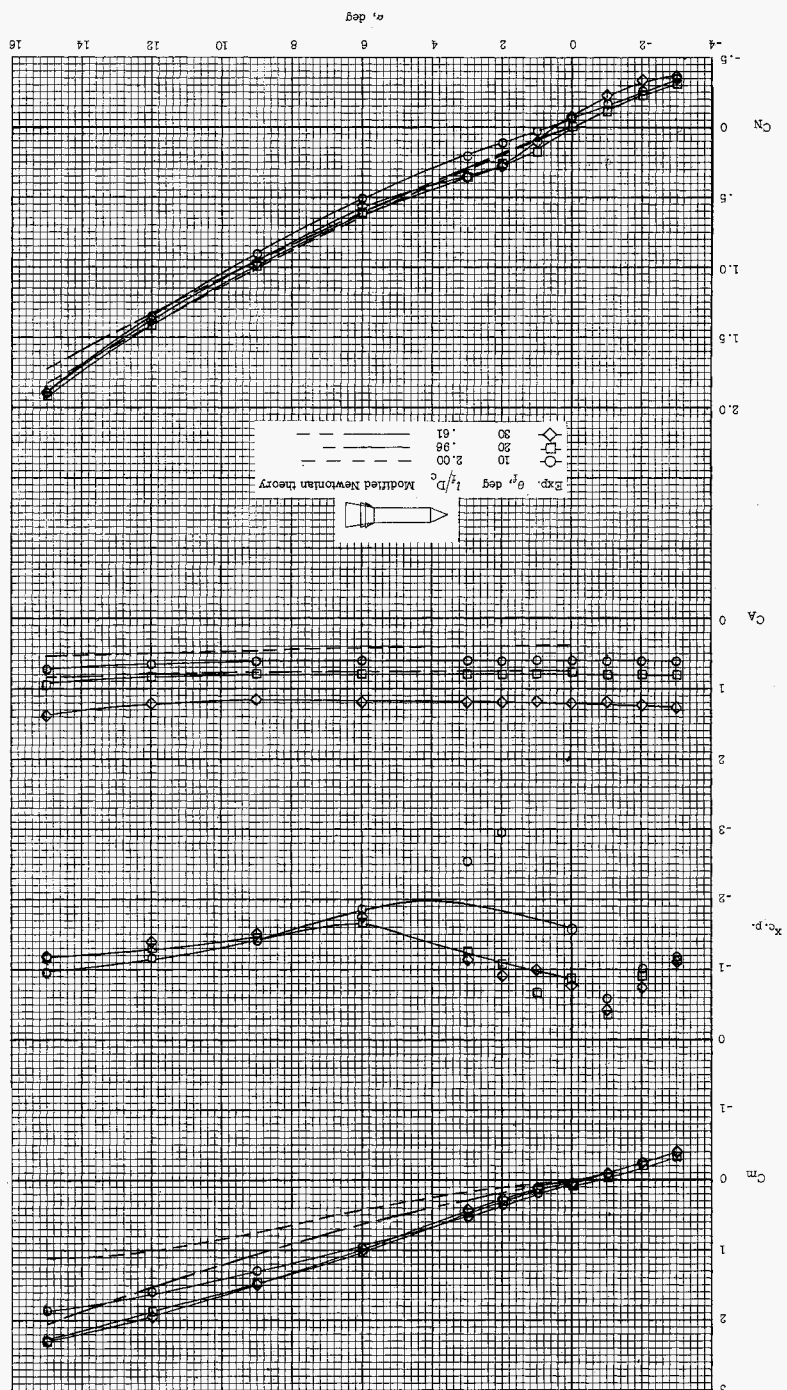


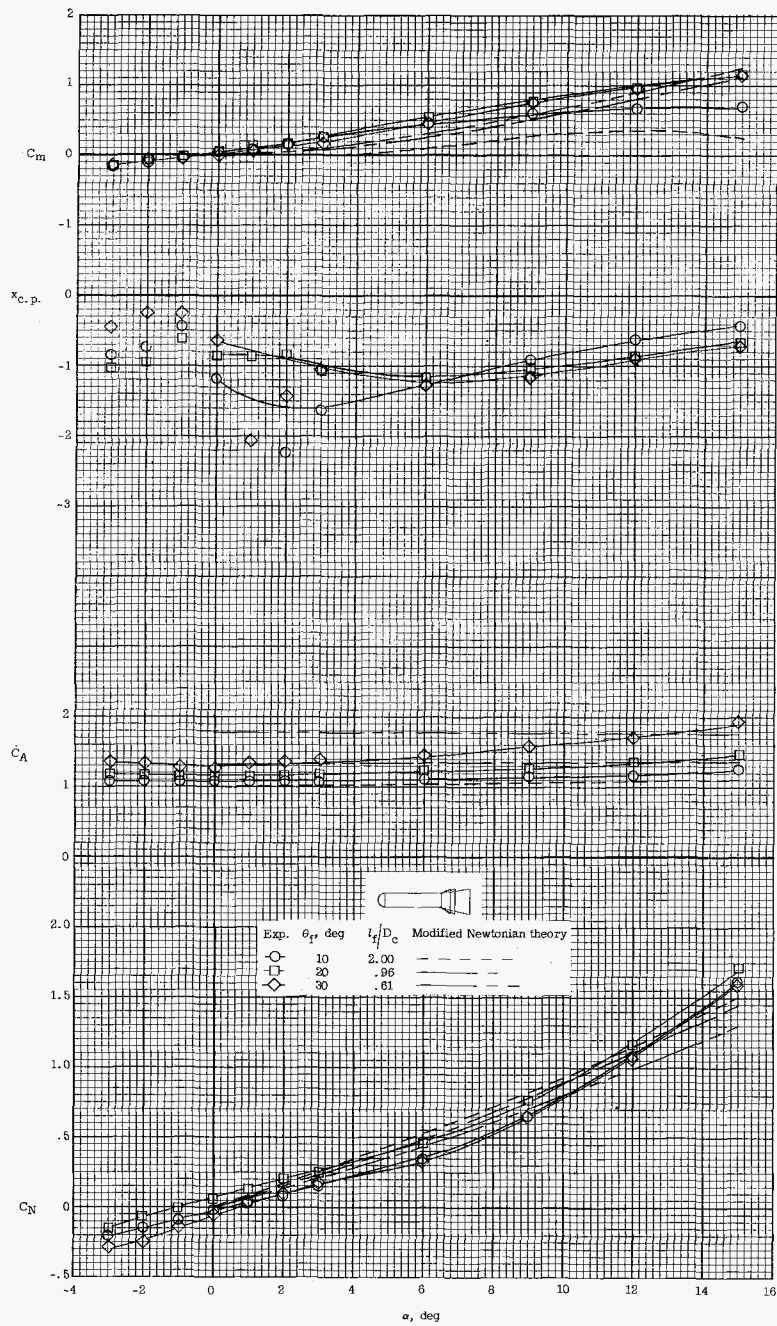
(d) Hemispherical nose, $l_c/D_c = 1.0$.

Figure 16.- Concluded.

Figure 17.- Effect of flare angle on the longitudinal aerodynamic characteristics of various configurations for a constant flare diameter, $D_f/D_c = 1.705$.

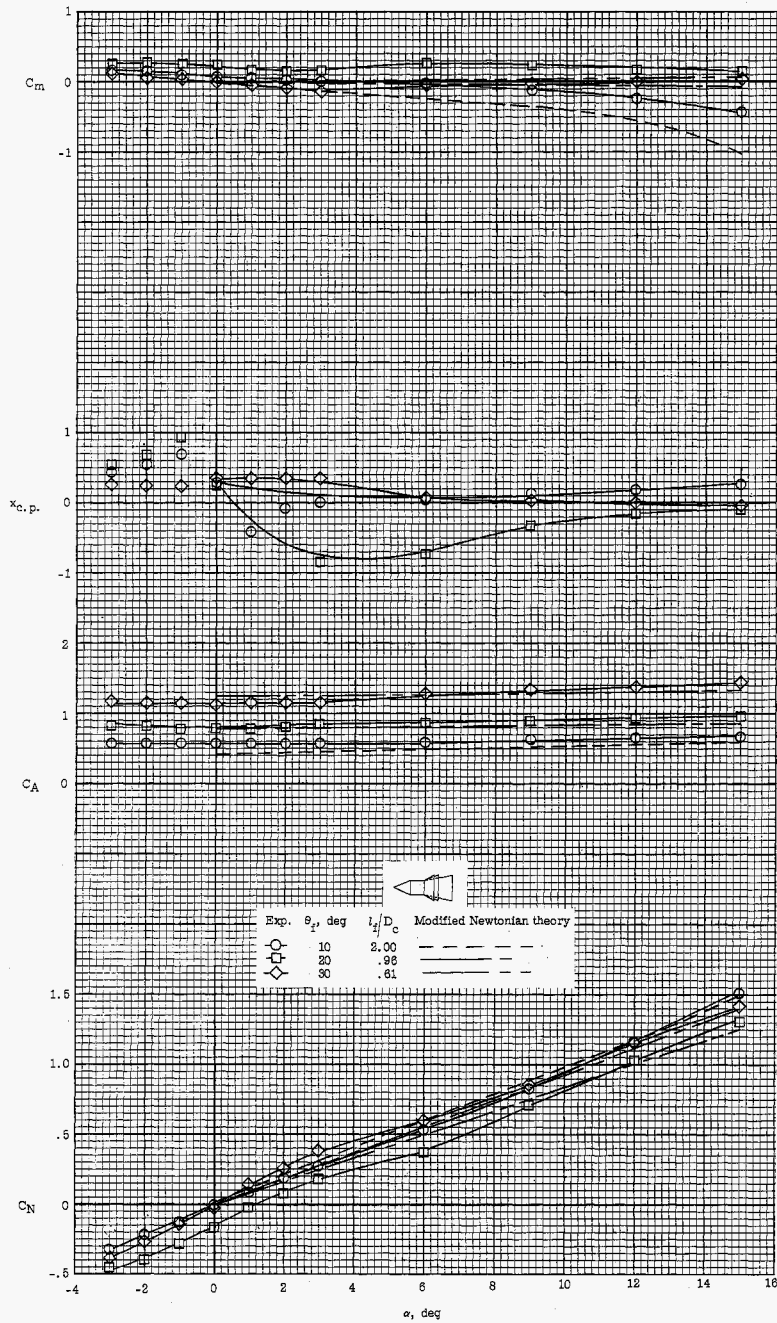
(a) Conical nose, $t_c/D_c = 4.0$.





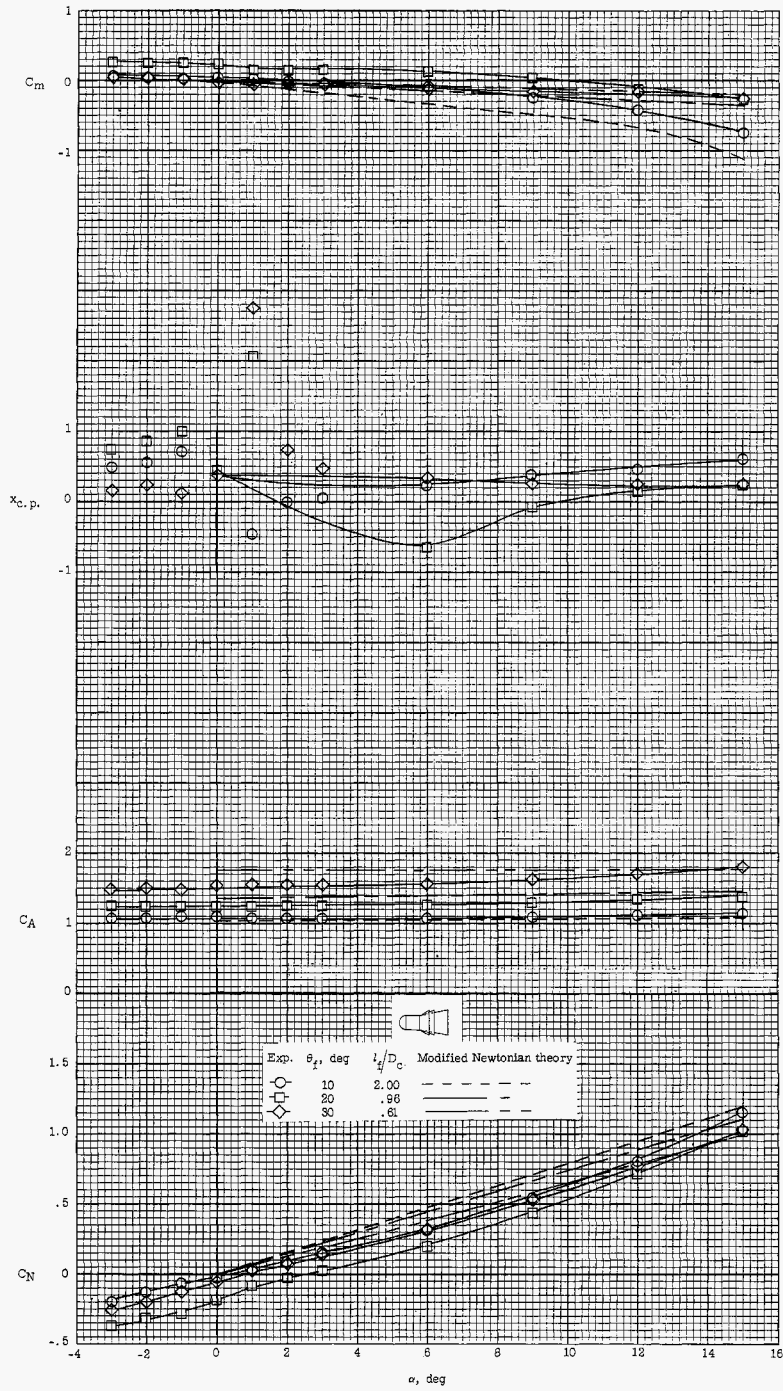
(b) Hemispherical nose, $l_c/D_c = 4.0$.

Figure 17.- Continued.



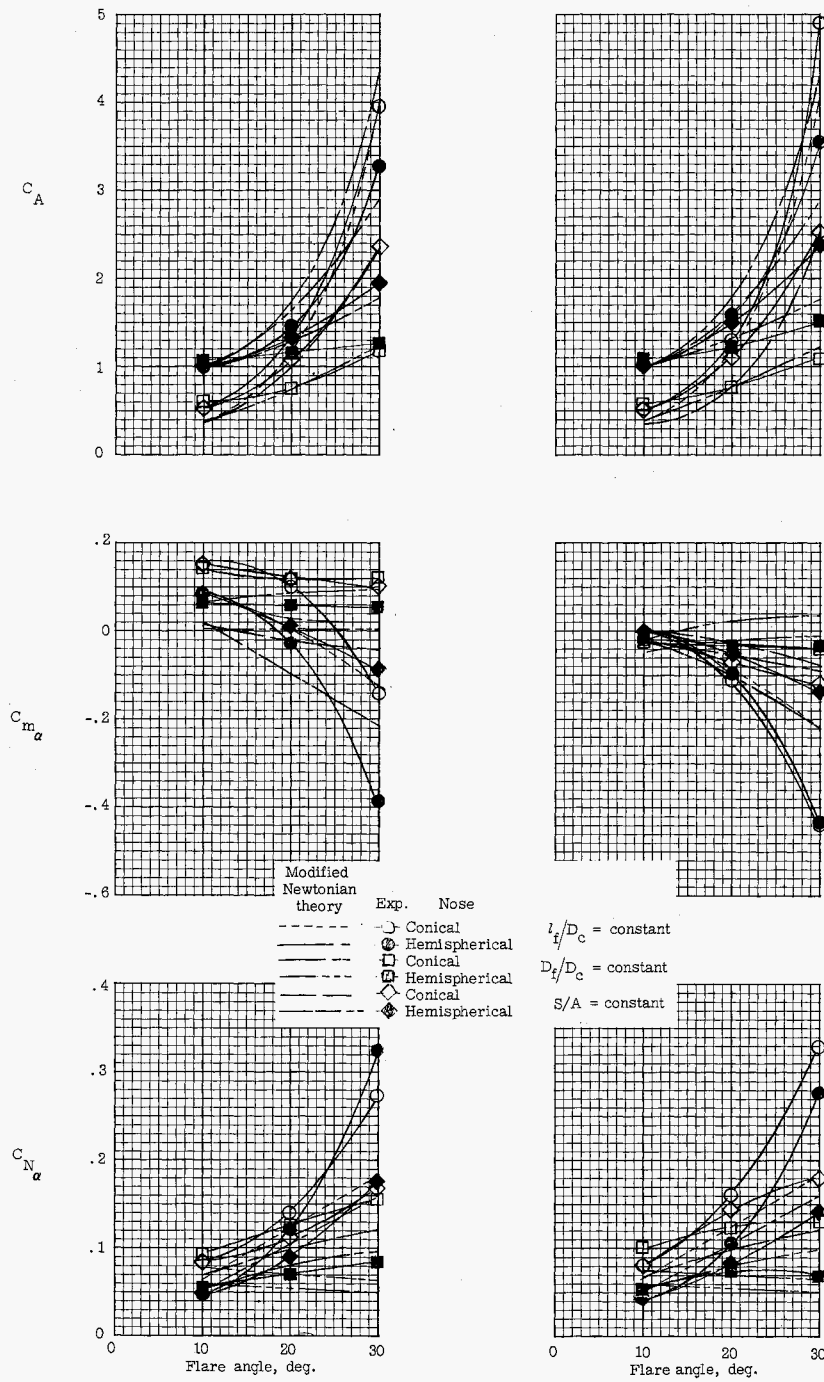
(c) Conical nose, $l_c/D_c = 1.0$.

Figure 17.- Continued.



(d) Hemispherical nose, $l_c/D_c = 1.0$.

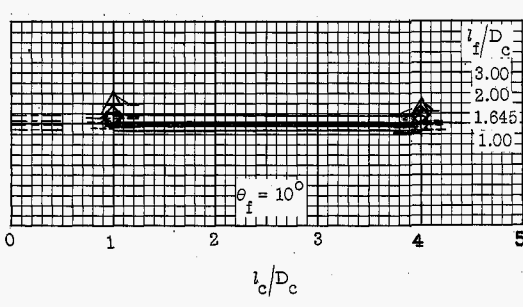
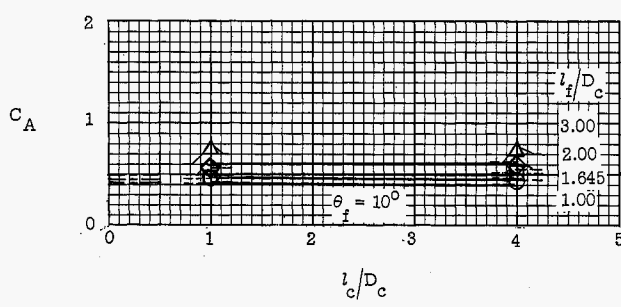
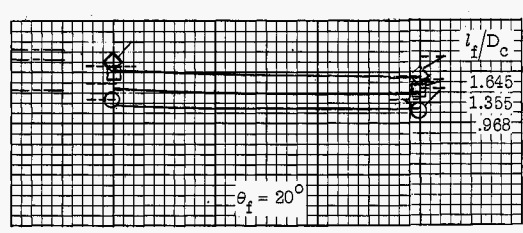
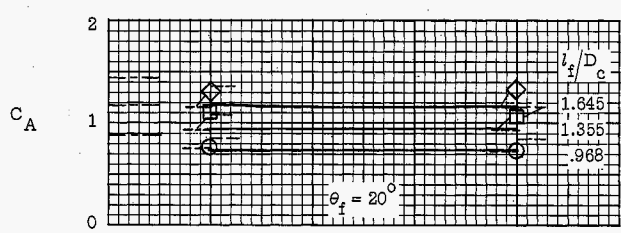
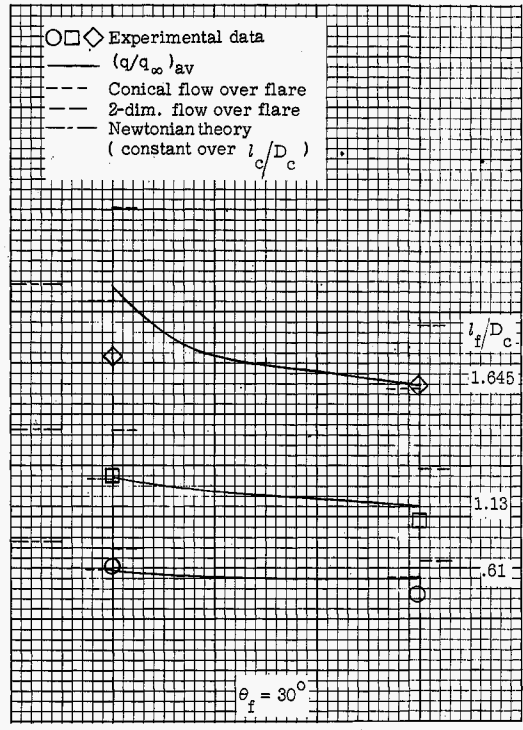
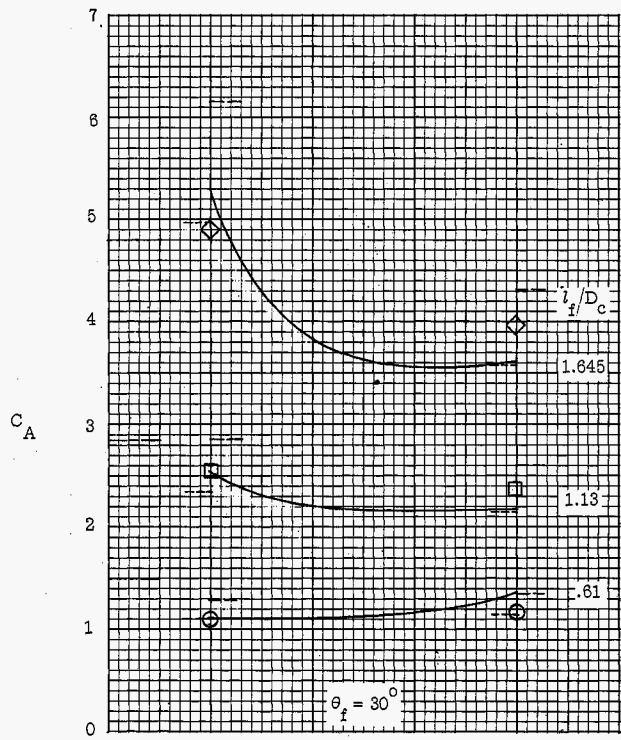
Figure 17.- Concluded.



(a) $l_c/D_c = 4.0$.

(b) $l_c/D_c = 1.0$.

Figure 18.- Variation of normal-force-coefficient and pitching-moment-coefficient slopes and axial-force coefficient at zero angle of attack with flare angle for various geometric constants of the flares.



(a) Conical.

(b) Hemispherical.

Figure 19.- Comparison of measured axial-force coefficient at zero angle of attack with values computed using the exact flow-field characteristics.